Hybrid Experimental-Numerical Determination of the Loading Path to Fracture in TRIP780 Sheets Subjected to Multi-axial Loading

by

Matthieu Dunand

Ingénieur de l'Ecole Polytechnique (2008)

Submitted to the Department of Mechanical Engineering
in Partial Fulfillment of the Requirements for the Degree of

Master of Science in Mechanical Engineering

at the

Massachusetts Institute of Technology

February 2010

Author:_____
Department of Mechanical Engineering
January 10, 2010

Certified by:_____
Dirk Mohr
CNRS Research Assistant Professor
Thesis Supervisor

Certified by:_____
Tomasz Wierzbicki
Professor of Applied Mechanics
Thesis Supervisor

Accepted by:_____
David E. Hardt
Professor of Mechanical Engineering
Chairman, Committee on Graduate Students

Hybrid Experimental-Numerical Determination of the Loading Path to Fracture in TRIP780 Sheets Subjected to Multi-axial Loading

Matthieu Dunand

Submitted to the Department of Mechanical Engineering
in January 2010, in partial fulfillment of the requirements for the degree of
Masters of Science in Mechanical Engineering

Abstract

The development of ductile fracture models of metals requires reliable measurements of the stress and strain histories up to the onset of fracture in multi-axial experiments. In the present work, a hybrid experimental-numerical approach is taken to determine the loading path in various fracture experiments on TRIP780 steel sheets. In most mechanical experiments on sheet metal, the localization of plastic deformation precedes the onset of fracture. After the beginning of necking, the stress fields within the specimen gage section become non-uniform and of three-dimensional nature. Consequently, the stress history prior to fracture can no longer be estimated based on the force history measurements using simple analytical formulas. A detailed finite element analysis of each experiment is required to identify the local stress and strain fields.

The results of the hybrid experimental-numerical analysis of a fracture experiment depend strongly on the chosen constitutive model. Here, an extensive bi-axial experimental program comprising more than 20 distinct loading conditions is performed to characterize the monotonic large deformation behavior of the TRIP780 steel. It is found that an anisotropic quadratic yield function along with a non-associated flow rule can accurately describe the inelastic behavior of the TRIP material.

A first series of fracture experiments is carried out on three types of full-thickness fracture specimens. This experimental program characterizes the onset of fracture for stress states between uniaxial tension and equi-biaxial tension. An effort is made to quantify and minimize the errors affecting the hybrid experimental-numerical analysis of those experiments. Inaccuracies affecting the stress triaxiality and plastic strain histories to fracture are evaluated by comparing surface strains measured by Digital Image Correlation (DIC) and computed by Finite Element Analysis (FEA). A second series of fracture experiments is carried out on a newly designed butterfly-shaped specimen, which allows for multi-axial testing under combinations of normal and tangential loads. Experiments for four different loading conditions are performed and used to analyze the onset of fracture for stress states ranging from pure shear to transverse plane strain tension.

Thesis Supervisors:	Dirk Mohr	Tomasz Wierzbicki
Titles:	CNRS Research Assistant Professor	Professor of Applied Mechanics

Table of Contents

List of Figures

List of Tables

Acknowledgments

I deeply thank my two advisors, Pr. Tomasz Wierzbicki and Pr. Dirk Mohr, for their guidance and support during my two first years at MIT. I am very grateful to Pr. Wierzbicki for having facilitated my admission at MIT and for funding me through a Research Assistantship at the Impact and Crashworthiness Laboratory.

I would also like to thank all the members of the ICL for their help, and for creating a cooperative working environment in which we all support each other. Thanks to: Dr. Carey Walters, Mr. Meng Luo, Ms. Allison Beese, Dr. JongMin Shim, Ms. Danielle Issa, Dr. Yaning Li. A special (and huge) thank goes to Sheila McNary, who was always ready to help me no matter what my problem was.

The partial support of the Joint MIT/Industry AHSS Fracture Consortium is gratefully acknowledged. POSCO Steel is thanked for providing the material.

Nadège, thank you for your unconditional support.

My final thought goes to all my friends, here at MIT or in France, and to my family, who make my life here in Boston easier and more cheerful.

Chapter 1.

Introduction

1.1 Background

1.1.1 Ductile fracture of metals

The use of sheet materials of high strength-to-weight ratio is essential in modern transportation vehicle engineering. This choice is driven by the constant quest for lower structural weight in an attempt to improve fuel efficiency, vehicle dynamics and cost efficiency. Candidate materials are advanced high strength steels which feature a tensile strength that is more than twice as high as that of conventional low carbon or HSLA steels. Special aluminum and magnesium alloys are also being considered, mostly for castings and extrusions. The common feature of light weight metal structures is that ductile fracture frequently limits their formability and crashworthiness.

Ductile fracture is generally described by the nucleation and growth of voids that ultimately link to form cracks. The early studies of McClintock (1968) and Rice and Tracey (1969) analyzed the evolution of cylindrical and spherical holes in a ductile matrix. Their results show that void growth is governed by the stress triaxiality. Gurson (1977) proposed a porous plasticity model which includes the void volume fraction as internal variable. Some phenomenological fracture models make use of Gurson's evolution equations assuming that ductile fracture occurs as the void volume fraction reaches a critical threshold value. The original Gurson model has been repeatedly improved by accounting for the loss of stress-carrying capacity associated with void coalescence (e.g. Tvergaard and Needleman, 1984), by incorporating enhanced strain hardening models (e.g. Leblond et al., 1995), by describing void shape effects (e.g. Pardoen and Hutchinson, 2000) and by incorporating plastic anisotropy (e.g. Benzerga et al., 2004) and shear

(e.g. Nahshon and Hutchinson, 2008). A comprehensive review of modified Gurson models can be found in Lassance et al. (2007).

As an alternative to micromechanics inspired fracture models, phenomenological models have been developed to predict ductile fracture without modeling void nucleation and growth. It is assumed that fracture occurs at a point of the body where a weighted measure of the accumulated plastic strain reaches a critical value. A comparative study of various weighting functions (including models based on the work of McClintock (1968), Rice and Tracey (1969), LeRoy et al. (1981), Cockcroft and Latham (1968), Oh et al. (1979), Brozzo et al. (1972), and Clift et al. (1990)) showed that none of them can accurately describe the fracture behavior of a given material over a large range of stress triaxialities (Bao and Wierzbicki, 2004). Attempts to define a more general fracture criterion have lead to the introduction of the third invariant of the stress tensor in the weighting function (e.g. Wierzbicki and Xue, 2005), or to the transformation of stress based fracture criteria into the space of stress triaxiality, Lode angle and equivalent plastic strain (Bai and Wierzbicki, 2008).

1.1.2 Previous experimental investigations on ductile fracture

Numerous experimental investigations have been carried out to characterize ductile fracture. Clausing (1970) performed an experimental study on axisymmetric and plane strain tensile fracture specimens of several materials and found a lower ductility for plane strain loading. Hancock and MacKenzie (1976) investigated the relationship between the ductility and the stress triaxiality for three different steels. They used smooth and U-notched axisymmetric tensile specimens and concluded that for all studied materials, the ductility is decreasing with stress triaxiality; the same authors also found good agreement between their experimental results and the predictions by Rice and Tracey's (1969) fracture model. Hancock and Brown (1983) compared experimental results from notched axisymmetric specimens and flat grooved plane strain specimens and concluded that the ductility was determined by the stress state, and not the strain state. Using split Hopkinson bars, Johnson and Cook (1985) performed dynamic torsion and notched tensile tests at different strain rates and temperatures. They concluded that the effect of stress triaxiality on the ductility of their tested metals was more significant than that of strain rate and temperature.

Bao (2003) carried out an extensive experimental program on aluminum 2024-T351 covering stress triaxialities ranging from compression to multi-axial tension. Bao's results suggested a transition region between shear and uniaxial tension, where ductility increases with stress triaxiality. Mohr and Henn (2007) proposed a butterfly-shaped flat specimen to study the onset of fracture over a wide range of stress triaxialities. When using this specimen in conjunction with a dual actuator system (Mohr and Oswald, 2008), virtually any loading condition between pure shear and transverse plane strain tension can be imposed.

1.2 Objectives and structure of the thesis

This works aims at determining the loading path to fracture in TRIP780 sheets under quasi-static loading, through hybrid experimental-numerical analysis over a wide range of stress states. It is divided into three main parts.

The first part of this thesis focuses on finding an accurate plasticity model for the TRIP780 material. The accuracy of quadratic plane stress plasticity models is evaluated. The sheet material exhibits a considerable direction-dependence of the r-ratio while the uniaxial stress-strain curves are approximately the same irrespective of the specimen direction. Isotropic and anisotropic associated as well as non-associated quadratic plasticity models are considered to describe this behavior. Using a newly-developed dual-actuator system, combinations of normal and tangential loads are applied to a flat specimen in order to characterize the sheet material response under more than 20 distinct multi-axial loading states. The comparison of the experimental results with the plasticity model predictions reveals that both the associated and non-associated quadratic formulations provide good estimates of the stress-strain response under multi-axial loading. However, the non-associated model is recommended when an accurate description of the thinning behavior is important. Moreover, a structural validation example is presented that demonstrates the higher prediction accuracy of the non-associated plasticity model.

In a second part, a basic ductile fracture testing program is carried out on specimens extracted from the TRIP780 material including tensile specimens with a central hole and circular notches. In addition, equi-biaxial punch tests are performed. The surface strain fields are measured using two- and three-dimensional digital image correlation. Due to the localization of plastic

deformation during the testing of the tensile specimens, finite element simulations are performed of each test to obtain the stress and strain histories at the material point where fracture initiates. Error estimates are made based on the differences between the predicted and measured local strains. The results from the testing of tensile specimens with a central hole as well as from punch tests show that equivalent strains of more than 0.8 can be achieved at approximately constant stress triaxialities to fracture of about 0.3 and 0.66, respectively. The error analysis demonstrates that both the equivalent plastic strain and the stress triaxiality are very sensitive to uncertainties in the experimental measurements and the numerical model assumptions. The results from computations with very fine solid element meshes agree well with the experiments when the strain hardening is identified from experiments up to very large strains.

In the last part, an attempt is made to characterize the ductile fracture behavior of the TRIP material in the intermediate range of stress triaxialities (from shear to uniaxial tension stress states). For that purpose, the experimental technique by Mohr and Henn (2007) is used. The design of the butterfly shaped specimen has been revisited in order to provide more homogeneous stress and strain states at the center of the gage section, where fracture initiate. The influence of each feature of the specimen design on the homogeneity of the material state has been investigated through a parametric study. The proposed specimen features concave lateral edges and a reduced-thickness gage section delimited by clothoidally-shaped fillets. The hybrid experimental-numerical analysis is carried out for four different loadings, ranging from shear to tension under transverse plane strain stress states. The analysis shows that tests results are very sensitive to the specimen machining precision. Furthermore, it is found that the local stress and strain fields within the specimen gage section cannot be computed with high accuracy at very large strains.

1.3 Material

The present study has been conducted using 1.5mm thick TRIP780 steel sheets provided by POSCO (Korea). This TRIP-assisted steel features a complex multiphase microstructures consisting of ferrite, bainite, martensite and metastable retained austenite. present complex multiphase microstructures consisting of a ferrite matrix and dispersion of multiphase grains of

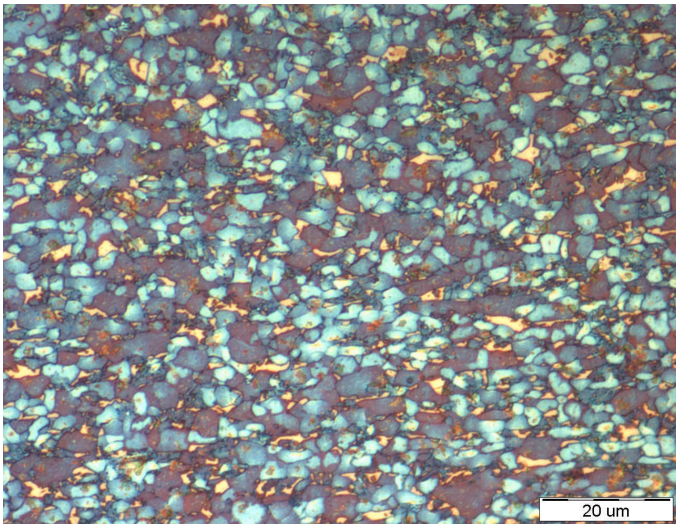

Figure 1-1: Microstructure of TRIP780.
Micrograph showing the different phases in the undeformed microstructure: grey=ferrite and bainite, yellow=retained austenite

bainite, martensite and metastable retained austenite (Jacques et al., 2007). The transformation of this retained austenite into martensite during straining is responsible for the so called TRIP (TRansformation Induced Plasticity) effect (Angel (1954), Lecroisey and Pineau (1972), Olsen and Cohen (1975), Stringfellow et al. (1992)). This effect enhances both the strength of the material by allowing maintenance of a high work hardening rate through the continuous appearance of martensite in the microstructure, and its ductility by improving dilatation and shear strains associated with the displacive formation of martensite (Jacques et al., 2001).

C	Al	Mn	Si	Mo
1.70	0.47	2.50	0.59	0.08

Table 1-1: Chemical composition of the TRIP780 material in wt-%

The exact chemical composition of the present TRIP780 material as measured by energy-dispersive X-ray analysis is given in Table 1-1. Micrographs (see figure 1-1) reveal a fine grain structure with a maximum grain size of about 10μm and an austenite content of about 6%.

1.4 Related Publications

Chap. 2 Mohr, D., Dunand, M. and Kim, K.H., Evaluation of Associated and Non-associated Quadratic Plasticity Models For Advanced High Strength Steel Sheets under Multi-axial Loading, *International Journal of Plasticity*, In Press, 2009.

Chap. 3 & 4 Dunand, M. and Mohr, D., Hybrid Experimental-numerical Analysis of Basic Ductile Fracture Experiments for Sheet Metals, *International Journal of Solids and Structures*, In Press, 2010.

Chap. 5 Dunand, M. and Mohr, D., Optimized Specimen for the Fracture Testing of Advanced High Strength Steels under Combined Normal and Shear Loading, *In Preparation*.

Chapter 2.

Calibration of a plasticity model

2.1 Introduction

In this chapter, we investigate the large deformation behavior of the TRIP780 steel under monotonic multi-axial loading. The key purpose of this study is to evaluate existing phenomenological plasticity models for sheet materials. The reader is referred to Chaboche (2008) for a recent review of macroscopic plasticity theories. Different yield surfaces have been used in the past to model advanced high strength steels: von Mises yield surface (e.g. Yoshida et al., 2002, Durrenberger et al., 2007), quadratic anisotropic Hill (1948) yield function (e.g. Banu et al., 2006, Padmanabhan et al., 2007, Campana and Cortese, 2007, Chen and Koc, 2007), high exponent isotropic Hershey (1954) yield function (Tarigopula et al., 2008), non-quadratic anisotropic Barlat (2003) yield function (Lee et al., 2005, 2008). Here, we focus on simple quadratic yield functions and evaluate their predictive capabilities for multi-axial loading conditions. Moreover, following the work by Stoughton (2002), we include both associated and non-associated quadratic flow rules. The discussion of non-associated formulations in metal plasticity has been partially initiated by the experimental observations of Spitzig and Richmond (1984). Non-associated plasticity models for metals have been considered by Casey and Sullivan (1985), Brünig and Obrecht (1998), Brünig (1999), Lademo et al. (1999), Stoughton (2002), Stoughton and Yoon (2004, 2008) and Cvitanic et al. (2008).

Kuwabara (2007) provides a comprehensive review of experimental techniques measuring the anisotropic behavior of sheet materials. As an alternative to the testing of cruciform specimens (e.g. Makinde et al. (1992), Boehler et al. (1994), Lin and Ding (1995), Müller and Pöhlandt (1996), Kuwabara et al. (1998)), we make use of a newly-developed combined tension and shear

technique (Mohr and Oswald, 2008). Similar to the experimental work reported in Wang et al. (2008), the technique of Oswald and Mohr (2008) achieves multi-axial stress-states through the application of normal and tangential loads to a rectangular sheet specimen. The TRIP780 sheet material is loaded monotonically along more than 20 different multi-axial loading paths. The comparison of the simulation and experimental results suggests that the use of Hill's (1948) quadratic anisotropic yield surface along with a non-associated flow rule provides satisfactory results from a phenomenological point of view.

2.2 Uniaxial experiments

Dogbone-shaped tensile specimens are cut from the sheet materials using a waterjet. In accordance with ASTM E8, the specimens featured a 12.7mm wide and 50mm long gage section. The specimens have been placed into an electro-mechanical universal testing machine with wedge grips (Model G45, MTS, Eden-Prarie). All experiments have been carried out at a cross-head loading velocity of less than 1mm/min. Both the axial and width strain are continuously measured using a digital image correlation system (VIC2D, Correlated Solution, SC). For this, a random speckle pattern with an average speckle size of about $100\mu m$ has been applied to the specimen gage section.

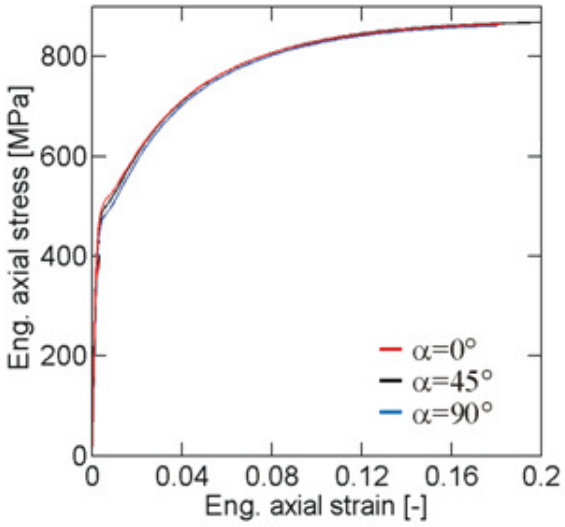

Figure 2-1: Uniaxial tensile testing – engineering stress strain curve.

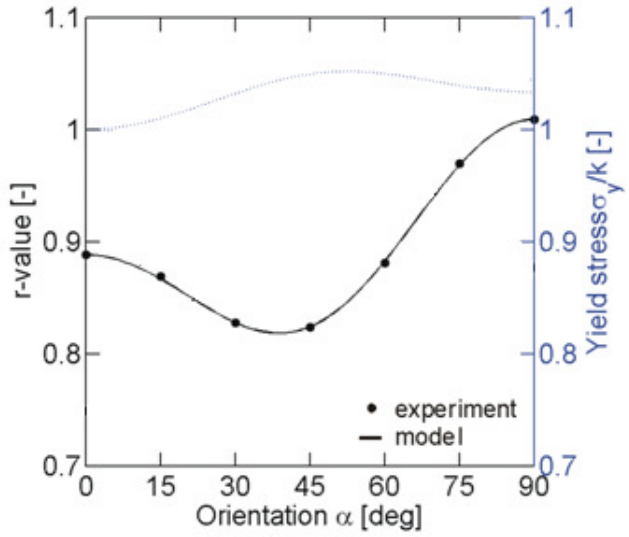

Figure 2-2: Results from uniaxial tensile test.
Calculated and measured r-ratio variations (black curves and solid dots, respectively) and calculated yield stress variations (dotted blue curves).

Specimens are cut from seven different directions, from $\alpha = 0°$ (rolling direction) to $\alpha = 90°$ (transverse direction) by step of 15°. The corresponding uniaxial engineering stress-strain curves are plotted in Fig. 2-1 up to their respective stress maximum. The results show that except for a short plateau at the beginning of the experiment along the rolling direction, all stress-strain curves lie almost on top of each other. The maximum differences in the stress level of up to 5% are observed at the very beginning of plastic deformation. The engineering stress at necking is about $850\ MPa$, irrespective of the material orientation.

Using a Young's modulus of $E = 185MPa$ and an elastic Poisson's ratio of $\nu = 0.3$, we calculated the logarithmic plastic axial and width strains from the measured stress-strain curves. Based on the assumption of plastic incompressibility, the r-values are then determined from the slopes of the corresponding linear approximation of the logarithmic plastic width strain versus logarithmic plastic thickness strain curves ($r = d\varepsilon_w^p / d\varepsilon_{th}^p$). The solid dots in Fig. 2-2 show the identified r-values as a function of the specimen orientation angle α. The average r-value, $\bar{r}$, defined as

$$\bar{r} = \frac{1}{4}(r_0 + 2\,r_{45} + r_{90}) \tag{2.1}$$

is 0.89.

2.3 Biaxial experiments

2.3.1 Biaxial testing technique

A series of biaxial experiments is performed using a newly-developed dual actuator system. The reader is refereed to Mohr and Oswald (2008) for details on the multi-axial testing procedure. The dual actuator system applies tangential and normal loads to the boundaries of a flat specimen. The horizontal actuator applies the tangential force to the lower specimen boundary. As shown in Fig. 2-3, the lower specimen clamp is mounted onto a low friction sliding table. A load cell positioned between the horizontal actuator and the lower specimen clamp measures the tangential force. The normal force is applied through the vertical actuator in the upper cross-head. Two additional load cells have been integrated into the lower sliding table to measure the total vertical force. For all tests, the hydraulic dual actuator system is run in the force-controlled mode.

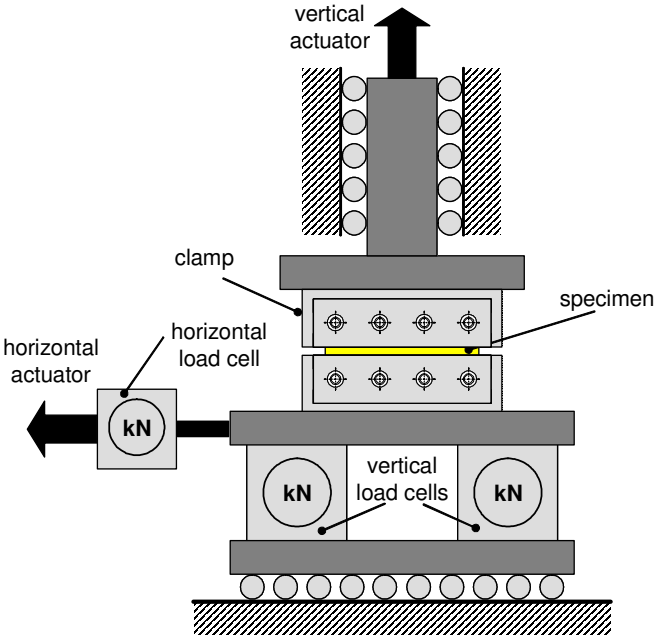

Figure 2-3: Schematic of the dual actuator system.

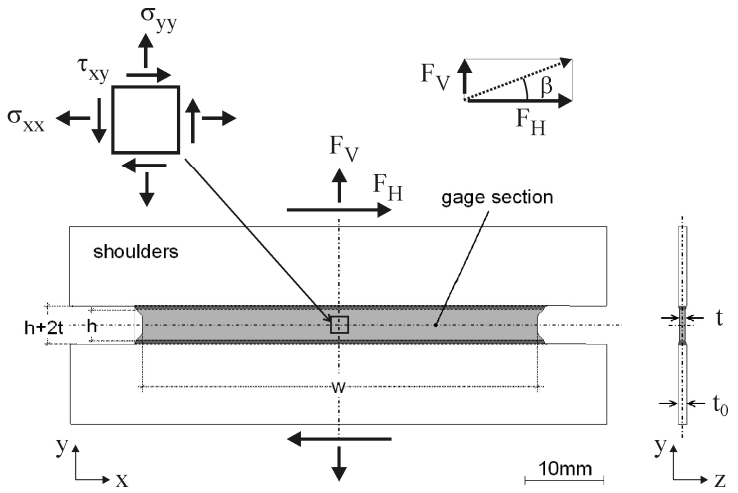

Figure 2-4: Specimen geometry and the definition of the biaxial loading angle β.

Figure 2-4 shows the exact shape and dimensions of the specimen. It features a $h = 4.5mm$ high and $w = 50mm$ wide gage section. The thickness of the gage section has been symmetrically reduced to about $t = 0.5mm$ using a conventional milling process. The displacements are measured directly on the specimen surface using a digital image correlation system (VIC2D, Correlated Solutions Inc, SC). More than 200 photographs are taken throughout each monotonic experiment. The data is acquired using the software packages FastTrack DAX (Instron, Canton, MA) and VicSnap (Correlated Solution, SC).

The limiting cases of $\beta = 0°$ and $\beta = 90°$ correspond to pure shear and transverse plane strain tension, respectively. In the case of orthotropic sheet materials, we introduce the *specimen orientation angle* α to report the orientation of the sheet rolling direction with respect to the vertical axis of the dual actuator system. We refer to the horizontal and vertical axis as the x- and y-direction, respectively.

As demonstrated by Mohr and Oswald (2008), the specimen is designed such that the engineering stress along the y-direction, Σ_y, may be approximated by

$$\Sigma_y \cong \frac{F_V}{A_0} \tag{2.2}$$

with the initial cross-sectional area of $A_0 = wt$. Equation (2.3) implies that the variations of the stress Σ_y are negligible along the x-direction. Similarly, due to the large width-to-height ratio, we

may assume that the shear stress variations along the x-direction are small. Hence, the engineering shear stress Σ_{xy} associated with the horizontal force measurement F_H reads

$$\Sigma_{xy} \cong \frac{F_H}{A_0} \tag{2.3}$$

The corresponding engineering normal strain E_y and engineering shear strain E_{xy} are determined from DIC. The state of stress in the specimen gage section is plane stress, while the state of deformation in this specimen is transverse plane strain. In other words, the strain along the x-direction is approximately zero, $E_x \cong 0$. In order to study distinct features of the material's constitutive response, it may be useful to map the measured stresses and strains into a coordinate system which is attached to the material's orthotropy axes (see Mohr and Jacquemin, 2008). However, the present work focuses on the validation of existing constitutive models which may be readily performed in the machine coordinate system.

2.3.2 Biaxial testing program

Biaxial tests are performed over a wide range of loading conditions by varying the biaxial loading angle β as well as by cutting the specimens at different angles α relative to the rolling direction. Three different batches of specimen have been extracted along three different sheet directions ($\alpha = 0°, \alpha = 45°, \alpha = 90°$) and subsequently tested at the following biaxial loading angles: $\beta = 0°$, $\beta = 28°$, $\beta = 49°$, $\beta = 63°$, $\beta = 74°$, $\beta = 82°$ and $\beta = 90°$. Note that the limiting cases $\beta = 0°$ and $\beta = 90°$ correspond to pure shear and transverse plane strain loading, respectively.

Figure 2-5 shows a graph which illustrates the different loading states on a generic von Mises yield surface in the plane stress subspace $(\sigma_0, \sigma_{90}, \tau)$, where σ_0 is the normal stress in the rolling direction, $\sigma_{90}$is the normal stress in the cross-rolling direction, and τ is the corresponding shear stress component. From each experiment, we obtain a normal stress versus normal strain curve as well as a shear stress versus shear strain curve. All measured normal and shear stress-strain curves can be found in Annex A. The results will be discussed in detail throughout our comparison of the experimental results with the numerical simulations in Paragraph 2.5.

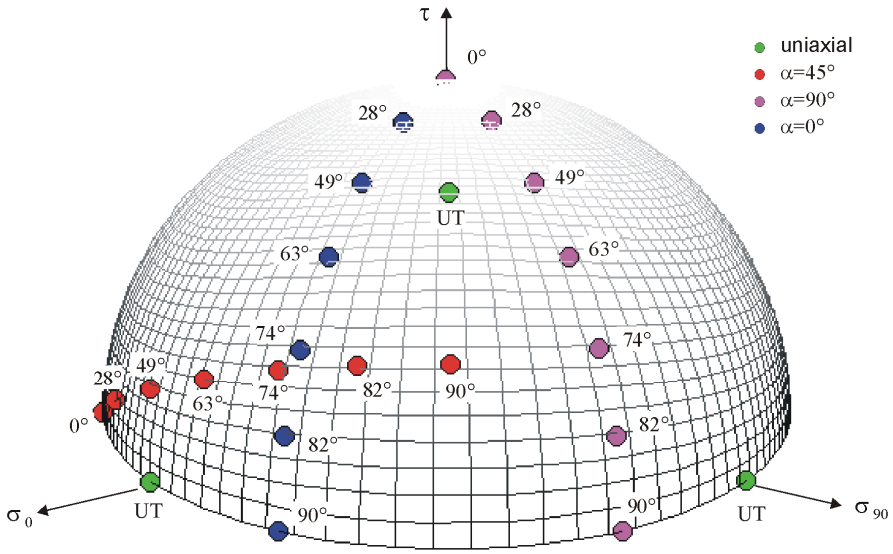

Figure 2-5: Visualization of the loading states in the 3-dimensional stress-space. The solid dots represent the intersection of the linear stress paths with a quadratic yield surface. The labels next to the data points denote the biaxial loading angle β while the point color corresponds to the specimen orientation α (see legend). The green dots correspond to uniaxial tension (UT).

2.4 Quadratic plane stress plasticity models

In the case of aluminum alloys, direct measurements of distinct points on the yield surface (e.g. Green et al., 2004) have shown that non-quadratic functions are needed to describe the boundary of the elastic domain with satisfactory accuracy. To the best knowledge of the author, no such yield surface measurements have been published in the open literature for dual phase or TRIP-assisted steel sheets. The use of non-quadratic yield envelopes for steels is usually justified through the upper bound calculations by Logan and Hosford (1980) or by r-value measurements. In the latter case, the assumption of associated plastic flow is imposed and the shape of the yield surface is adjusted such that the r-values are predicted accurately. However, as pointed out by Stoughton (2002), Bishop and Hill's (1951) proof of the associated flow rule is only valid if slip according to Schmid's law is the dominant deformation mechanism at the crystal level.

Similar to the results by Padmanabhan et al. (2007) on a Dual-Phase Steel, the present uniaxial experiments indicated a pronounced direction dependency of the r-value (Fig. 2-2), while nearly the same stress-strain curve has been measured for all specimen directions. In other words, the r-value measurements suggest planar anisotropy while the material's response is planar isotropic as far as the stress level is concerned. It is straightforward to show that a standard associated plasticity model with a quadratic yield surface cannot replicate this behavior. As an alternative to the formulation of non-quadratic associated plasticity models (e.g. Barlat, 2003a,b), we loosen the constraint of associated plastic flow. As suggested by Stoughton (2002), we make use of a quadratic yield surface in conjunction with a non-associated quadratic plastic flow potential. Thus, the computational efficiency of quadratic plasticity models is maintained while providing a model structure that can describe the present uniaxial experiments accurately. The reader is referred to Stoughton (2002) for the proof of the uniqueness of the states of stress and strain as well as the proof of stability of plastic flow.

2.4.1 Plane stress yield surface

As discussed above, we limit our attention to the quadratic yield function proposed by Hill (1948). It may be written in the form

$$f(\boldsymbol{\sigma}, k) = \bar{\sigma} - k = 0 \tag{2.4}$$

where $\bar{\sigma}$ is the equivalent stress,

$$\bar{\sigma} = \sqrt{(\boldsymbol{P}\boldsymbol{\sigma}) \cdot \boldsymbol{\sigma}} \tag{2.5}$$

$\boldsymbol{\sigma}$ denotes the Cauchy stress vector in material coordiantes

$$\boldsymbol{\sigma} = [\sigma_0 \quad \sigma_{90} \quad \tau]^T \tag{2.6}$$

with the true stress components σ_0 along the rolling direction, σ_{90} along the cross-rolling direction and the corresponding shear stress τ. **P** shall be a symmetric positive-definite matrix defined through the three independent parameters P_{22}, P_{33} and P_{12}

$$\boldsymbol{P} = \begin{bmatrix} 1 & P_{12} & 0 \\ P_{12} & P_{22} & 0 \\ 0 & 0 & P_{33} \end{bmatrix} \tag{2.7}$$

2.4.2 Flow rule

The flow rule describes the incremental evolution of the plastic strain vector

$$d\boldsymbol{\varepsilon_p} = \begin{bmatrix} d\varepsilon_0^p & d\varepsilon_{90}^p & d\gamma^p \end{bmatrix}^T \tag{2.8}$$

$d\varepsilon_0^p$ and $d\varepsilon_{90}^p$ denote the plastic strain components along the rolling and cross-rolling direction, while γ^p denotes the plastic engineering shear strain (which is twice the mathematical shear strain). The direction of plastic flow is assumed to be aligned to the stress derivative of the flow potential function $g(\boldsymbol{\sigma})$

$$d\boldsymbol{\varepsilon_p} = d\lambda \frac{\partial g}{\partial \boldsymbol{\sigma}} \tag{2.9}$$

where $d\lambda \geq 0$ is a scalar plastic multiplier. In close analogy with the yield function, the potential function $g(\boldsymbol{\sigma})$ is defined as a quadratic function in stress space,

$$g(\boldsymbol{\sigma}) = \sqrt{(\boldsymbol{G\sigma}) \cdot \boldsymbol{\sigma}} \tag{2.10}$$

with the positive definite coefficient matrix

$$\boldsymbol{G} = \begin{bmatrix} 1 & G_{12} & 0 \\ G_{12} & G_{22} & 0 \\ 0 & 0 & G_{33} \end{bmatrix} \tag{2.11}$$

Note that in the special case of $= \boldsymbol{G}$, we recover the associated flow rule.

2.4.3 Isotropic hardening

The distinction between isotropic and kinematic hardening is omitted since the present evaluation is limited to monotonic loading conditions. Isotropic strain hardening is described

through the relationship between the deformation resistance k and the equivalent plastic strain. Formally, we introduce the hardening modulus $h = h(\bar{\varepsilon}^p)$ and the evolution equation

$$dk = h(\bar{\varepsilon}^p)d\bar{\varepsilon}^p \qquad \text{with} \qquad k(\bar{\varepsilon}^p = 0) = k_0 \tag{2.12}$$

The equivalent plastic strain $\bar{\varepsilon}^p$ is defined as incrementally work-conjugate to the equivalent stress, i.e.

$$\boldsymbol{\sigma} \cdot \left(d\boldsymbol{\varepsilon_p}\right) = \bar{\sigma}(d\bar{\varepsilon}^p\,) \tag{2.13}$$

Upon evaluation of this relationship for non-associated plastic flow, we obtain the following relationship between the equivalent plastic strain and the plastic multiplier,

$$d\bar{\varepsilon}^p = \frac{g(\boldsymbol{\sigma})}{\bar{\sigma}}(d\lambda) \tag{2.14}$$

as well as the relationship between the equivalent plastic strain and the plastic strain tensor,

$$d\bar{\varepsilon}^p = \left(\frac{g}{\bar{\sigma}}\right)^2 \sqrt{\left[\boldsymbol{P}\boldsymbol{G}^{-1}\left(d\boldsymbol{\varepsilon_p}\right)\right] \cdot \boldsymbol{G}^{-1}\left(d\boldsymbol{\varepsilon_p}\right)} \tag{2.15}$$

The evaluation of the present experimental data for the TRIP780 steel revealed that the Swift (1952) law provides a good approximation of the relationship between the equivalents stress and the equivalent plastic strain. In the case of monotonic loading, the Swift law reads

$$\bar{\sigma} = A(\varepsilon_s + \bar{\varepsilon}^p)^n \tag{2.16}$$

with the model parameters A, $\bar{\varepsilon}^p$ and n given in Table 2-1. Consequently, we chose the following special function to define the hardening modulus as a function of the equivalent plastic strain:

$$h(\bar{\varepsilon}^p) = nA(\varepsilon_s + \bar{\varepsilon}^p)^{n-1} \tag{2.17}$$

In the case of the structural validation simulations (see Section 2.6), the modified Swift law approximation is employed for an equivalent plastic strain of up to 0.2. Thereafter, we use a piecewise-linear extrapolation curve which has been determined from biaxial punch experiments (see section 4.3).

A [MPa]	$\bar{\varepsilon}^p$ [-]	n [-]
1460	1.63×10^{-3}	0.204

Table 2-1: Swift hardening law parameters

2.4.4 Model Calibration

It is common practice to calibrate anisotropic plasticity models based on Lankford's r-values. According to our flow rule, the dependence of the r-value on the loading direction is

$$r(\alpha) = \frac{(G_{33} + 2G_{12} - G_{22} - 1)\sin^2\alpha\cos^2\alpha - G_{12}}{(1 - G_{22})\cos^2\alpha + G_{12} + G_{22}} \tag{2.18}$$

where α denotes the angle between the material rolling direction and the loading axis. In the present comparative study, we consider four special parameter settings of the general non-associated quadratic plasticity model. For historic reasons, we refer to these special cases as different models:

- Model #1: Isotropic model with associated plastic flow. By setting $P_{11} = P_{22} = 1.0$, $P_{12} = -0.5$ and $P_{33} = 3.0$, we recover the isotropic von Mises yield surface. Furthermore, we assume $\boldsymbol{P} = \boldsymbol{G}$ which corresponds to associated plastic flow.
- Model #2: Orthotropic model with associated plastic flow. By imposing associated plastic flow, $\boldsymbol{P} = \boldsymbol{G}$, we may use the r-value measurements to calibrate both coefficient matrices. The relationships among the r-values r_0, r_{45} and r_{90} and the coefficients read:

$$G_{12} = -\frac{r_0}{1 + r_0}, \qquad G_{22} = \frac{r_0}{r_{90}}\frac{1 + r_{90}}{1 + r_0} \quad \text{and} \quad G_{33} = \frac{1 + 2r_{45}}{r_{90}}\frac{r_0 + r_{90}}{1 + r_0} \tag{2.19}$$

- Model #3: Planar isotropy (normal anisotropy) with associated plastic flow. In this case, we still have $\boldsymbol{P} = \boldsymbol{G}$, while both matrices are calibrated based on the average r-value:

$$G_{12} = -\frac{\bar{r}}{1 + \bar{r}}, \qquad G_{22} = 1 \quad \text{and} \quad G_{33} = 2\frac{1 + 2\bar{r}}{1 + \bar{r}} \tag{2.20}$$

- Model #4: Isotropic yield surface with non-associated anisotropic plastic flow rule. As in model #1, we set $P_{11} = P_{22} = 1.0$, $P_{12} = -0.5$ and $P_{33} = 3.0$. At the same time, we make use of the coefficients determined for model #2 to predict the direction of plastic flow.

- Model #5: Planar isotropic yield surface with non associated flow potential. The same $\boldsymbol{G}$ matrix as for model #2 is used to define the flow rule. The yield surface is defined through the Hill parameters for planar isotropy (see model #3). However, instead of using the average r-value, a suitable $\bar{r}$ may be identified from calibrating the model with respect to the transverse plane strain tension tests ($\beta = 90°$). The analytical expressions for the yield stresses under transverse plane strain conditions read

$$\sigma_y^{TPS-0} = \frac{k}{\sqrt{1 - 2P_{12}\left(\frac{G_{12}}{G_{22}}\right) + P_{22}\left(\frac{G_{12}}{G_{22}}\right)^2}} \tag{2.21}$$

for loading along the rolling direction and

$$\sigma_y^{TPS-90} = \frac{k}{\sqrt{G_{12}^2 - 2P_{12}G_{12} + P_{22}}} \tag{2.22}$$

for loading along the cross-rolling direction. In the present case, $\bar{r} = 0.91$ yielded the best results.

Tables 2-2 summarize the corresponding parameter settings.

	r_0	r_{45}	r_{90}	P_{12}	P_{22}	P_{33}	G_{12}	G_{22}	G_{33}
#1	1.00	1.00	1.00	-0.50	1.00	3.00	-0.50	1.00	3.00
#2	0.89	0.82	1.01	-0.47	0.94	2.64	-0.47	0.94	2.64
#3	0.89	0.89	0.89	-0.47	1.00	2.94	-0.47	1.00	2.94
#4	0.89	0.82	1.01	-0.50	1.00	3.00	-0.47	0.94	2.64
#5	0.89	0.82	1.01	-0.48	1.00	2.95	-0.47	0.94	2.64

Table 2-2: Plasticity model parameters

2.5 Results and comparison

A standard return-mapping algorithm is used to implement the constitutive model(s) into a commercial finite element program (user subroutine for ABAQUS/explicit (Abaqus, 2008)). Using the different sets of parameters (Table 2-2), finite element simulations are performed to investigate the predicative capabilities of all five plasticity models. The finite element model of the biaxial experiment comprises a single reduced integration plane stress element (Abaqus element CPS4R) that is subject to different radial engineering stress paths as specified by the biaxial loading angle β. The transverse plane strain condition is imposed by imposing kinematic constraints on displacement boundary conditions. The outcomes of each single-element simulation are two engineering stress-strain curves (normal and shear) which are the compared to the experimental results.

2.5.1 Uniaxial stress-strain curve and r-ratios

Figures 2-6 and 2-7 compares all experimental and simulation results for uniaxial loading. Models #1, #3, #4 and #5 all predict the same uniaxial stress-strain curves irrespective of the loading direction. Note that the curves labeled isotropic, planar isotropic and non-associated are all lying on top of each other in Figure 2-6. Model #2 is the only one using a fully-orthotropic yield surface and consequently the stress-level can only be predicted with high accuracy for the specimens loaded along the rolling direction, while the stress level is respectively under- and overestimated for 45° and 90° loading.

The orthotropic Hill model with associated flow rule (model #2) can describe the direction dependency of the r-values. The solid black lines in Fig. 2-2 show the r-value variations that are predicted after calibrating the Hill model. Observe the good agreement of the model with the experimental data points (solid dots). However, since the flow rule and the yield surface are associated in the standard Hill model, the r-value direction dependency translates into a direction-dependency of the stress-strain curves. The direction-dependent yield stress which is given by

$$\sigma_y(\alpha) = \frac{k}{\sqrt{\cos^4\alpha + \sin^2\alpha\cos^2\alpha\,(2P_{12} + P_{33}) + \sin^4\alpha\; P_{22}}} \tag{2.23}$$

is plotted as dotted blue lines in Fig. 2-2. The ratio of the maximum and minimum yield stress is 1.05. Due to this direction-dependency of the yield stress, the standard Hill model (model #2) cannot predict the uniaxial stress-strain curves to a great degree of accuracy for all specimen orientations (see red curves in Fig. 2-6). Model #4 makes use of a von Mises yield surface and a Hill flow rule. As a result, both the r-ratio variations and the uniaxial stress-strain curves are modeled accurately for all specimen orientations. The same accuracy with respect to the uniaxial experiments may be achieved by using a planar isotropic (i.e. normal anisotropic) yield surface along with the Hill flow rule (models #5).

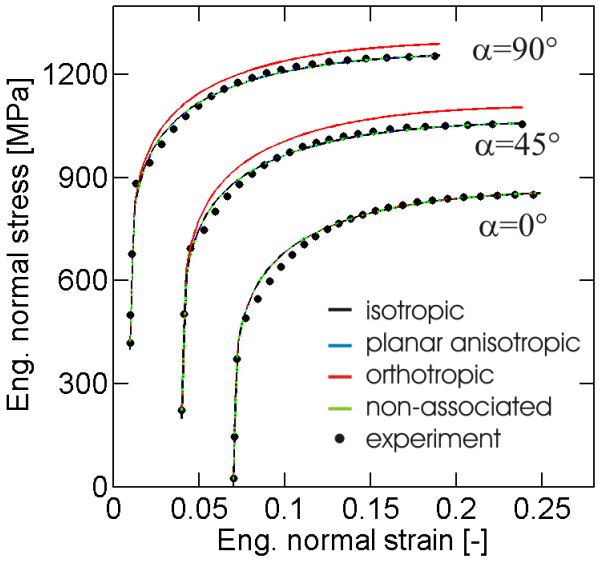

Figure 2-6: Model predictions for uniaxial loading - engineering stress-strain curves. The experimental results are shown by dots, while the solid lines correspond to the model predictions.

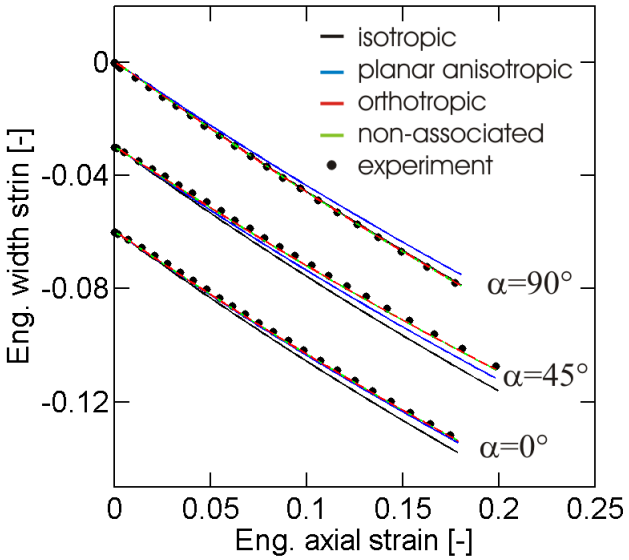

Figure 2-7: Model predictions for uniaxial loading – Strain evolution
Strain along the width direction as a function of the axial engineering strain. The experimental results are shown by dots, while the solid lines correspond to the model predictions.

2.5.2 Multi-axial experiments

Each multi-axial experiment is simulated using the plasticity models. Subsequently, we extracted one normal stress-strain curve and one shear stress-strain curve from each simulation and compared the computational and experimental results. Annex A summarizes the stress-strain curves. The solid curves represent the simulation results for the isotropic von Mises model; the experimental results are shown by dashed lines. The model and the experiments show a remarkably good overall agreement. Note that the transverse plane strain stress-strain response ($\beta = 90°$) is predicted accurately for all three specimen orientations ($\alpha = 0°$, $45°$ and $90°$). The same holds true for the shear stress-strain curves where the relative error in the estimated stress level is less than 5% irrespective of the specimen orientation α and the biaxial loading angle β. The simulation results for the other models are more or less identical (within 1% as far as the stress level is concerned). Even though the other models predict different r-ratios than the isotropic von Mises model, this anisotropic feature played only a minor role as far as the predictions under multi-axial loading are concerned. The only noteworthy exception is the prediction of the pure shear stress-strain curve for the associated Hill model (model #2). Here, the

Hill model overestimates the shear stress by about 5%. This is due to the low value of the parameter P_{33}. Note that the yield stress τ_y for pure shear loading is $\tau_y = k/\sqrt{P_{33}}$.

The use of the planar isotropic yield surface in combination with an orthotropic flow rule (model #5) may be seen as the most accurate model. It provides an accurate description of all uniaxial data while its prediction accuracy for multi-axial loading is similar to that of model #3.

2.6 Structural validation

The analysis of the biaxial plasticity experiments does not provide a clear answer as to whether the direction of plastic flow is associated or non-associated with the yield surface. In this section, a structural experiment is presented to elucidate the difference between these two modeling approaches. In the previous material experiments, the stress and strain fields are approximately uniform throughout the entire specimen. In a structural experiment, the fields are usually non-uniform and a wider range of stress states is covered by a single experiment. Even though it is difficult to deduce material properties from a structural experiment, the comparison of numerical simulations with the experimental results can be used to validate the underlying material model. Here, we perform a structural experiment on a butterfly-shaped specimen, sketched in Fig. 2-8. Subsequently, a finite element analysis is performed to assess the influence of the flow rule assumption on the simulation results.

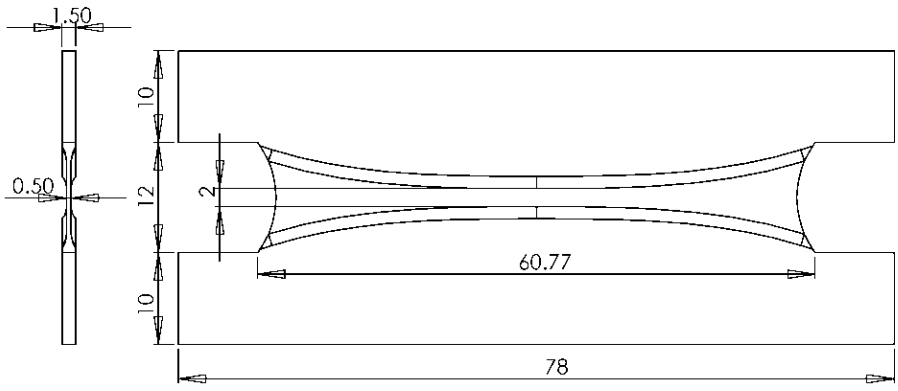

Figure 2-8: Geometry on the butterfly specimen

2.6.1 *Experiments and numerical model*

The geometry of the butterfly-shaped specimen is detailed in Chapter 5 of the present thesis. It has been developed for fracture testing, but in the present context we are only interested in its elasto-plastic response. The specimen is extracted from a 1.4*mm* thick TRIP780 sheet using CNC machining. The material rolling direction is aligned with the vertical direction of the testing machine (corresponds also to vertical direction of Fig. 2-8). After verifying the dimensions of the machined specimens, we make use of the same dual-actuator system as for biaxial plasticity testing to subject the specimen to a combination of horizontal (tangential) and vertical (normal) loads ($\beta = 63°$ until the maximum force is reached). The displacements of the specimen boundaries are measured using digital image correlation. The measured vertical and horizontal force-displacement curves are shown as dashed lines in Figure 2-9.

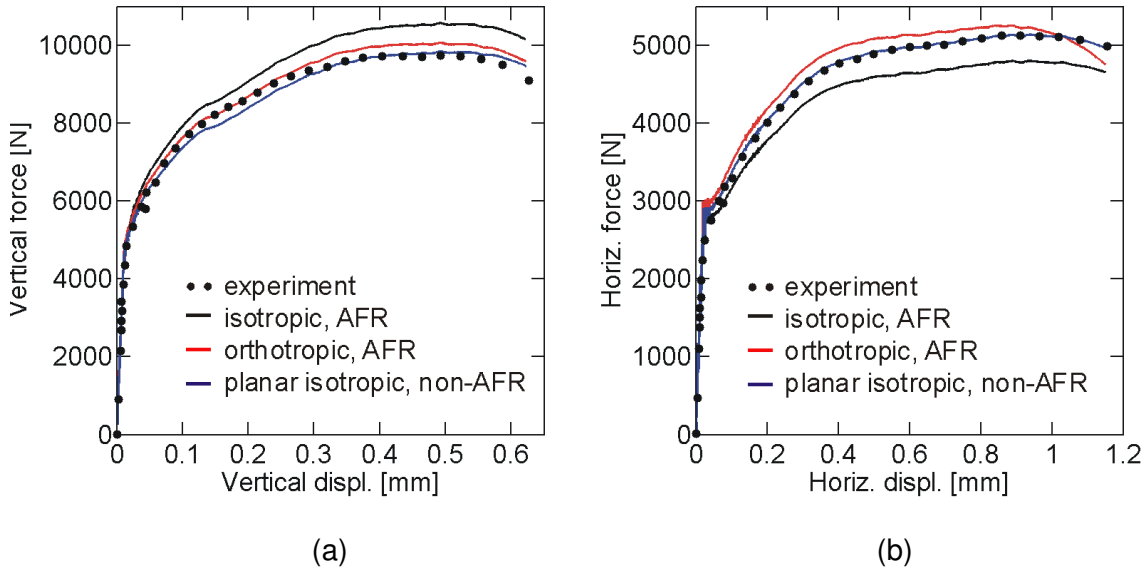

(a) (b)

Figure 2-9: Results for butterfly specimen
(a) vertical force-displacement curve, (b) horizontal force-displacement curve.

The specimen geometry is discretizated using first-order reduced integration solid elements (element C3D8R of the Abaqus element library). Due to the symmetry of the mechanical problem only one half of the specimen is meshed with at least five elements along the thickness direction. A total of 80,000 elements is used to mesh the entire specimen geometry. The DIC measured

displacements and rotations (almost zero) are applied to the boundaries of the virtual specimen assuming that the boundary surfaces remain plane throughout testing. The simulations are performed using Abaqus/explicit with double precision. The material density and loading velocity are scaled such that more than 600,000 explicit time steps are required to compute the quasi-static solution of the boundary value problem.

2.6.2 Extension of the plasticity model to 3-dimensional stress states

The quadratic equivalent Hill stress can be expressed for a three dimensional stress state as:

$$\bar{\sigma} = \sqrt{F(\sigma_{22} - \sigma_{33})^2 + G(\sigma_{33} - \sigma_{11})^2 + H(\sigma_{22} - \sigma_{11})^2 + 2L\sigma_{23}^2 + 2M\sigma_{13}^2 + 2N\sigma_{12}^2} \qquad (2.24)$$

We can thus generalize the framework given in Paragraph 2.4 by using 6 components stress and strain vectors, and 6-by-6 $\widetilde{\boldsymbol{P}}$ and $\widetilde{\boldsymbol{G}}$ matrixes.

The Cauchy stress vector $\boldsymbol{\sigma}$ is now defined in material coordinates as:

$$\boldsymbol{\sigma} = [\sigma_0 \quad \sigma_{90} \quad \sigma_{th} \quad \sigma_{0-90} \quad \sigma_{0-th} \quad \sigma_{90-th}]^T \qquad (2.25)$$

where σ_{th} is the out-of-plane stress, σ_{0-90} the in-plane shear stress, σ_{0-th} and σ_{90-th} the out-of-plane shear stresses.

Similarly the plastic strain vector becomes:

$$\boldsymbol{d\varepsilon^p} = [d\varepsilon_0 \quad d\varepsilon_{90} \quad d\varepsilon_{th} \quad d\varepsilon_{0-90} \quad d\varepsilon_{0-th} \quad d\varepsilon_{90-th}]^T \qquad (2.26)$$

The equivalent stress $\bar{\sigma}$ (resp. flow potential $g(\boldsymbol{\sigma})$) is given by:

$$\bar{\sigma} = \sqrt{(\widetilde{\boldsymbol{P}}\boldsymbol{\sigma}) \cdot \boldsymbol{\sigma}} \qquad (2.27)$$

where positive definite matrix $\widetilde{\boldsymbol{P}}$ (resp. $\widetilde{\boldsymbol{G}}$) becomes:

$$\widetilde{\boldsymbol{P}} = \begin{bmatrix} 1 & \tilde{P}_{12} & \tilde{P}_{13} & 0 & 0 & 0 \\ \tilde{P}_{12} & \tilde{P}_{22} & \tilde{P}_{23} & 0 & 0 & 0 \\ \tilde{P}_{413} & \tilde{P}_{23} & \tilde{P}_{33} & 0 & 0 & 0 \\ 0 & 0 & 0 & \tilde{P}_{44} & 0 & 0 \\ 0 & 0 & 0 & 0 & \tilde{P}_{55} & 0 \\ 0 & 0 & 0 & 0 & 0 & \tilde{P}_{66} \end{bmatrix} \tag{2.28}$$

The coefficients of $\widetilde{\boldsymbol{P}}$ (resp. $\widetilde{\boldsymbol{G}}$) are linked to the 6 Hill48 coefficients through:

$$\begin{aligned} \tilde{P}_{22} &= F + H \\ \tilde{P}_{33} &= F + G \\ \tilde{P}_{12} &= -H \\ \tilde{P}_{13} &= -G \\ \tilde{P}_{23} &= -F \\ \tilde{P}_{44} &= 2N \\ \tilde{P}_{55} &= 2M \\ \tilde{P}_{66} &= 2L \end{aligned} \tag{2.29}$$

with:

$$F = \frac{r_0}{r_{90}}\frac{1}{1+r_0}\,, \qquad G = \frac{1}{1+r_0}\,, \qquad H = \frac{r_0}{1+r_0} \text{ and } \quad N = \frac{1+2r_{45}}{2r_{90}}\frac{r_0+r_{90}}{1+r_0} \tag{2.30}$$

Due to lack of experimental data for out-of-plane shear, we assume *L* and *M* are equal to 1.5 (value for isotropic materials).

2.6.3 Results

The numerical simulations are performed for material model #1 (isotropic yield with AFR), model #2 (orthotropic yield with AFR) and model #5 (planar isotropic yield with non-AFR). Figure 2-9 shows the predicted vertical and horizontal force-displacement curves. It is interesting to observe that the isotropic model overestimates the vertical force (Fig. 2-9.a) while it underestimates the horizontal force (Fig. 2-9.b). The simulation with the associated orthotropic model (red curves) provides an accurate prediction of the vertical force up to a displacement of about 0.3*mm*, but overestimates the vertical force level thereafter. The same model overestimates the horizontal force up to its maximum. Beyond this point, the horizontal force decreases much faster in the simulation than in the experiments. The non-associated planar isotropic model (blue

curves) provides the best overall predictions. It slightly underestimates the vertical force level at the beginning of the experiments, but provides very accurate predictions of the tangential force-displacement curve including its decreasing branch.

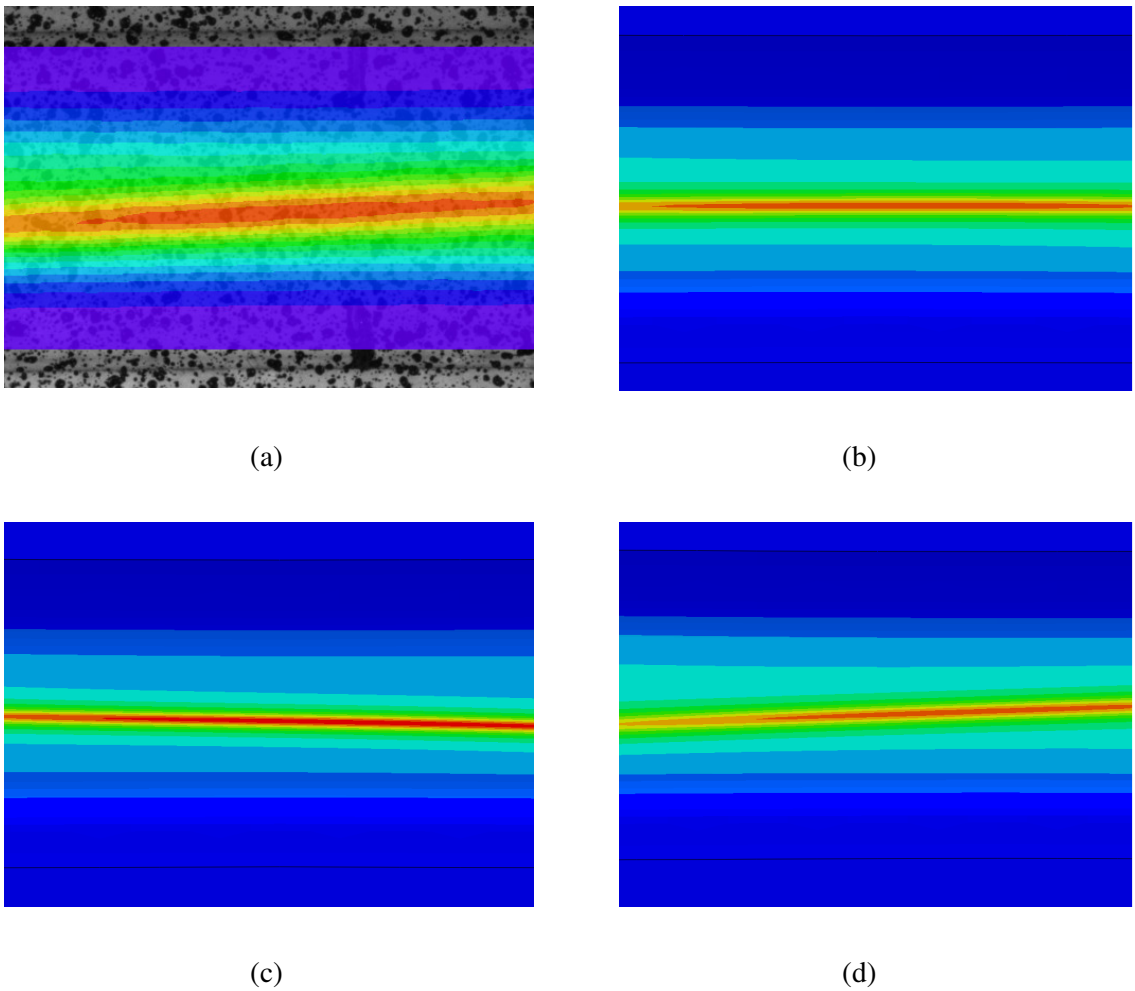

(a) (b)

(c) (d)

Figure 2-10: Contour plot of the maximum principal strain fields before the onset of fracture (a) experiment, (b) isotropic model with AFR, (c) orthotropic model with AFR, (d) planar isotropic model with AFR. The Lagrangian strain ranging from 0 to 0.8 is shown for the experiment, while the logarithmic strain ranging from 0 to 0.95 is depicted for the simulations. In all four cases, the strain fields are plotted on the undeformed configuration of the butterfly specimen

The advantages of the non-associated model become even more apparent when comparing the fields of deformation. Figure 2-10.a shows the DIC measured field of deformation towards the end of the experiment. A band of deformation localization is clearly visible at that point. The

corresponding numerical predictions (Figs. 2-10.b and 2-10.c) reveal that the predictions of both the associated isotropic and the associated orthotropic models are very different from the experimental result. The orientation of the band of localization is almost opposite to that observed in the experiment. However, the predicted orientation of the simulations with non-associated flow rule (Fig. 2-10.d) agrees well with the experimental observation (Fig. 2-10.a).

2.7 Discussion

The results for uniaxial tension clearly indicate that the anisotropy of the material needs to be taken into account in order to obtain satisfactory predictions of the direction-dependent thickness reduction. Thus, different anisotropic models have been considered for the multi-axial simulations in addition to the isotropic Levy-von Mises model. The comparison of the simulation and experimental results shows that all models provide overall good estimates of the stress-strain curves for a wide range of multi-axial loading conditions. Both associated and non-associated plasticity models have been considered. The present comparison of the respective model predictions with the results from biaxial plasticity tests does not provide a clear answer to the question as to whether the plasticity of the TRIP steel is associated or non-associated. However, the example of a butterfly-shaped specimen shows strong evidence that the plasticity of the TRIP steel is non-associated.

Both the associated and non-associated model types appear to perform well under the tested biaxial loading conditions. Highly accurate measurements and repeatable material properties would be needed to shed more light on this issue. Here, the accuracy of the experimentally-measured stresses is only about ±2% for the multi-axial experiments (Mohr and Oswald, 2008). The uniaxial tensile experiments have shown that almost the same stress-strain curve is obtained while the r-ratio varies for different specimen orientations. Therefore, a non-associated plasticity model with a planar isotropic yield surface and a non-associated anisotropic flow potential is proposed to model the uniaxial experiments.

Most of the present biaxial plasticity experiments have been performed under force control. The material has been loaded along radial loading paths in stress space. Thus, the choice of the yield surface had a stronger effect on the measured stress-strain curves for multi-axial loading

than the flow rule. Note that the multi-axial simulation results for model #1 (isotropic yield surface and isotropic flow rule) and model #4 (isotropic yield and orthotropic flow rule) are almost identical for loading angles and specimen orientations. Similarly, all multi-axial predictions for model #3 (planar isotropic yield surface and associated flow) and model #5 (planar isotropic yield surface and non-associated flow) were almost identical. The differences between the isotropic von Mises surface and the orthotropic Hill'48 surface are small for the tested material. A future study on a sheet material with a higher degree of anisotropy may allow for a better differentiation between the prediction accuracy of associated and non-associated plasticity models. Furthermore, it is recommended to include equi-biaxial tensile tests in the experimental program to validate the assumption of a quadratic yield function.

2.8 Conclusion

The isotropic Levy-von Mises model and the associated orthotropic Hill (1948) plasticity models are considered in this study to describe the large deformation response of TRIP780 steel sheets. The uniaxial tensile experiments reveal a pronounced in-plane direction-dependence of the r-ratios while the measured stress-strain curves appeared to be direction-independent. Here, Stoughton's (2002) non-associated quadratic flow rule is employed as an alternative to non-quadratic associated plasticity models. Using a newly-developed testing technique for sheet materials (Mohr and Oswald, 2008), a series of multi-axial experiments has been performed on the TRIP material. The comparison of the experiments with the simulation results shows that both the associated and non-associated quadratic plasticity model provide a satisfactory description of the mechanical response under multi-axial loading. However, the non-associated model is recommended when the thinning of the sheets needs to be predicted with a high degree of accuracy. Moreover, a structural validation example is presented that elucidates substantial differences between the simulations with associated and non-associated flow rule. In the case of the non-associated flow rule the force-displacement curves as well as the position of the strain localization band are predicted accurately.

Chapter 3.

Hybrid Experimental-numerical Method

3.1 Introduction

In most fracture experiments on sheet materials, the localization of plastic deformation through necking cannot be avoided. After necking, the stress fields within the specimen gage section become non-uniform and of three-dimensional nature (stresses in the thickness direction develop). Consequently, the stress history prior to fracture can no longer be estimated from the force history measurements using simple analytical formulas. Unless reliable in-situ neutron diffraction stress measurements (e.g. Lee et al., 2002) and three-dimensional tomography based digital image correlation measurements (e.g. Baranger et al., 2009) are available, the stress and strain histories prior to fracture need to be determined in a hybrid experimental-numerical approach. In other words, a detailed finite element analysis of each experiment is required to identify the stress and strain fields. This forced marriage of experimental and computational mechanics involves the risk of adding up the errors from both the experiment and the numerical simulation. In the present chapter, we limit our attention to the determination of the stress triaxiality and the equivalent plastic strain history to fracture and to the evaluation their accuracy.

3.2 Determination of the onset of fracture

The displacement fields on the specimen surface are measured using either two-dimensional or three-dimensional Digital Image Correlation (DIC). Based on the DIC measurements, we define the *instant of onset of fracture* (not the location) by the first detectable discontinuity in the measured displacement field at the specimen surface. Subsequently, a finite element simulation is

performed of each experiment. Post-processing of those simulations gives then access to the evolution of the stress triaxiality and the equivalent plastic strain. For the experiments performed within this study, it is assumed that the *location of the onset of fracture* coincides with the location of the highest equivalent plastic strain within the specimen at the instant of onset of fracture. The corresponding equivalent plastic strain is referred to as *fracture strain* $\bar{\varepsilon}^f$.

3.3 Sources of error

3.3.1 Experimental error

Among all experimental uncertainties, we consider the error in the optical displacement field measurement as critically important for the determination of the fracture strain and triaxiality. Possible errors in the initial specimen geometry including thickness can be easily eliminated through dimensional verification prior to each experiment. The accuracy of the DIC procedure used to measure the fracture displacement depends mainly on the quality of the speckle pattern applied on the specimen and on the interpolation function used during the correlation. In order to get the least error, the pattern has been applied following the recommendations of Sutton et al. (2009) in terms of speckle size and density. Based on correlations performed on computer-generated sinusoidal waves, Sutton et al. (2009) concluded that for an appropriate speckle pattern, cubic B-spline displacement field interpolation functions produce an interpolation bias of about 1/40 pixel.

3.3.2 Computational error

The solution obtained from finite element analysis usually differs from the exact solution of the corresponding physical problem. In addition to shortcomings of the material model, the FEA is affected by different sources of errors (e.g. Bathe, 1996). In particular, errors associated with the spatial and time discretization as well as the constitutive model are monitored in this study:

- Spatial discretization errors are minimized by increasing the number of elements. To find a suitable mesh, we start with a coarse mesh that is successively refined by

dividing the elements' characteristic dimensions by two until the result converges. It is considered that convergence is achieved when an additional element division does not change the final plastic strain by more than 0.5%.

- Time discretization errors are minimized by increasing the number of implicit time steps. It is considered that convergence is achieved when adding 50% more time increments does not change the final plastic strain by more than 0.5%.

Furthermore, round-off errors are minimized by using the double precision floating point format in our computations with explicit time integration.

3.3.3 Error estimation

Due to the redundancy of measurements, we compare the logarithmic strain history obtained from DIC with that computed by FEA at the point on the surface where the first displacement field discontinuity appears. For every time step in the finite element simulation, there is a difference between the computed strain increment $\boldsymbol{d\varepsilon_{FEA}}$ at the surface of the specimen and the actual strain increment $\boldsymbol{d\varepsilon_{DIC}}$ measured by DIC. The error affecting the determined plastic strain increment at the location of the onset of fracture, $\boldsymbol{\delta(d\bar{\varepsilon}^p)}$, is then estimated based on the strain increment difference on the specimen surface,

$$\delta(d\bar{\varepsilon}^p) \cong \frac{d\bar{\varepsilon}^p}{|d\varepsilon_{DIC}|}|d\varepsilon_{DIC} - d\varepsilon_{FEA}| \tag{3.1}$$

Furthermore, we estimate the error in the accumulated equivalent plastic strain as

$$\delta\bar{\varepsilon}^p \cong \int_{\mathbf{0}}^{\bar{\boldsymbol{\varepsilon}}^{\boldsymbol{p}}} \left(\frac{|d\varepsilon_{DIC} - d\varepsilon_{FEA}|}{|d\varepsilon_{DIC}|}\right) d\bar{\varepsilon}^p \tag{3.2}$$

It is noted that the above error estimate represents both computational and experimental uncertainties. Using the definition of the stress triaxiality,

$$\eta = \frac{\sigma_m}{\bar{\sigma}_{VM}} \text{ with } \sigma_m = \frac{tr(\boldsymbol{\sigma})}{3} \tag{3.3}$$

the error in the stress triaxiality is related to the error in the hydrostatic stress $\boldsymbol{\sigma_m}$ and that in the von Mises stress,

$$\delta\eta = \frac{1}{\bar{\sigma}_{VM}}[\delta\sigma_m + \eta\delta\bar{\sigma}_{VM}] \tag{3.4}$$

It is assumed that all the components of the stress tensor are computed with the same error,

$$\frac{\delta\sigma_m}{\sigma_m} = \frac{\delta\bar{\sigma}_{VM}}{\bar{\sigma}_{VM}} = \frac{\delta\bar{\sigma}_{Hill}}{\bar{\sigma}_{Hill}} \tag{3.5}$$

and thus

$$\delta\eta = 2\frac{\eta}{\bar{\sigma}_{VM}}\delta\bar{\sigma}_{Hill} \tag{3.6}$$

Using the hardening law, the first order estimate of the error in stress triaxiality may be written as

$$\delta\eta = 2\frac{\eta}{\bar{\sigma}_{VM}}H(\bar{\varepsilon}^p)\delta\bar{\varepsilon}^p \tag{3.7}$$

Chapter 4.

Analysis of basic ductile fracture experiments

4.1 Introduction

A series of three different types of fracture experiments is carried out on TRIP780 steel: notched tensile tests, punch tests and tensile test on specimens with a central hole. The common feature of these three types of fracture experiments is their simplicity: (1) the specimens can be easily extracted from sheet material, and (2) all experiments can be performed on a universal testing machine. For each type of specimen, the accuracy of the hybrid experimental-numerical loading history identification is evaluated from the comparison of local digital image correlation measurements with FE predictions. It is found that the shell element meshes are not suitable for post-necking analysis of local strain fields. Conversely, solid element simulations provide accurate estimates of the measured local strain fields when the plasticity model is identified for large strains. The results demonstrate the stress triaxiality in specimens with a central hole is close to 0.3 all the way to fracture. Furthermore, it is noted that this type of experiment is also suitable for the identification of the stress-strain curve for very large strains.

4.2 Notched tensile tests

The first type of specimen considered in this study is a flat tensile specimen with circular cutouts (Figure 4-1). The stress triaxiality within the specimen is a function of the notch radius. For very large notch radii the stress state near the specimen center (prior to necking) corresponds to uniaxial tension, while the plane strain condition (along the width direction) is achieved for

very small notch radii. In the case of isotropic materials, this variation of stress state corresponds to a range of triaxialities from 0.33 to 0.58.

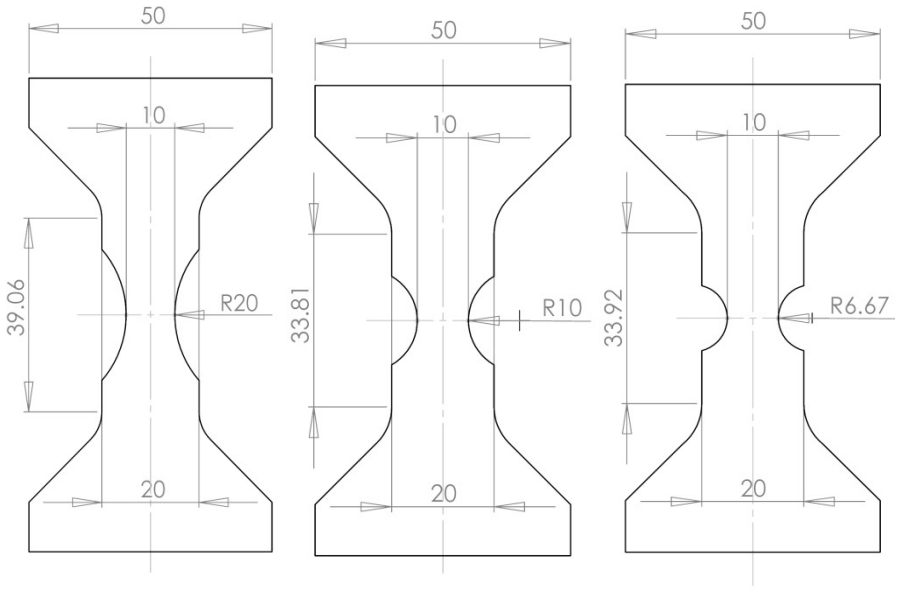

Figure 4-1: Geometry of the notched tensile specimens.
The special shape of specimen shoulders is due to the geometry of our high pressure grips; the total clamping force is applied to an area of 50x10*mm* at the top of the shoulders.

4.2.1 Experimental procedure

Specimens are extracted from the sheet material using water-jet cutting. The specimen loading axis is always oriented along the rolling direction. All specimens are 20mm wide and feature a b=10mm wide notched gage section. Three different notch radii are considered: R=20mm, R=10mm and R=6.67mm. The specimens are tested on a hydraulic testing machine (Instron Model 8080) with custom-made high pressure clamps. All experiments are carried out under displacement control at a constant crosshead velocity of 0.5mm/min.

During the tests, two digital cameras (QImaging Retiga 1300i with 105mm Nikon Nikkor lenses) take about 300 pictures (resolution 1300x1030 pixels) of the speckle-painted front and back surface of the specimens. The pictures of the front surface are used to determine the displacements of the specimen boundaries. The front camera is positioned at a distance of 1.25m to take pictures of the entire specimen (square pixel edge length of 51μm). The photographs of

the back face are used to perform accurate DIC measurements of the displacement field at the center of the specimen gage section. For that purpose, the second camera is positioned at a distance of 0.25m which reduces the square pixel edge length to 9.5μm. The average speckle size is about 70μm on both faces. The displacement field is calculated by DIC (VIC2D, Correlated Solutions) based on the assumption of an affine transformation of the 21x21 pixel neighborhood of each point of interest. The logarithmic axial strain at the center of the specimen is computed from the relative vertical displacement Δv of two points located at the center of the specimen,

$$\varepsilon = \ln\left(1 + \frac{\Delta v}{\Delta y}\right) \tag{4.1}$$

Both points are located on the vertical axis of symmetry at an initial distance of $\Delta y = 20 pixels$ (190μm). For each specimen geometry, we also performed an interrupted test: the monotonic displacement loading has been interrupted at a crosshead displacement of approximately 98% of the measured displacement to fracture. Subsequently, two 12 mm long samples have been extracted from the deformed specimen gage section; the small samples are embedded in an epoxy matrix for polishing; low magnification pictures are then taken to determine the thickness profile along the specimen's planes of symmetry.

4.2.2 Experimental results

The force-displacement curves for the three different notched geometries (black solid dots in Fig. 4-2) are shown all the way to fracture. All feature a force maximum before fracture occurs. The displacement to fracture presents small variations for different tests carried out on a given geometry (less than 3%). The measured fracture displacements and the corresponding experimental uncertainty are summarized in Table 4-1. DIC analysis of the strain fields shows important strain localization near the center of the specimens. The evolution of the logarithmic axial strain with respect to displacement is shown as solid blue dots in Fig. 4-2. Irrespective of the notch radius, two consecutive increases of the local strain rate become apparent. The first corresponds to the development of diffuse necking (localization through the width of the gage section), while the second indicates the onset of localized necking (through the thickness localization). The localized necking provokes a severe thickness reduction at the center of the

specimens. The measured thickness variations along the axial plane of symmetry of the samples obtained from interrupted tests are depicted in Fig. 4-3. Observe the severe thickness reduction for all three geometries.

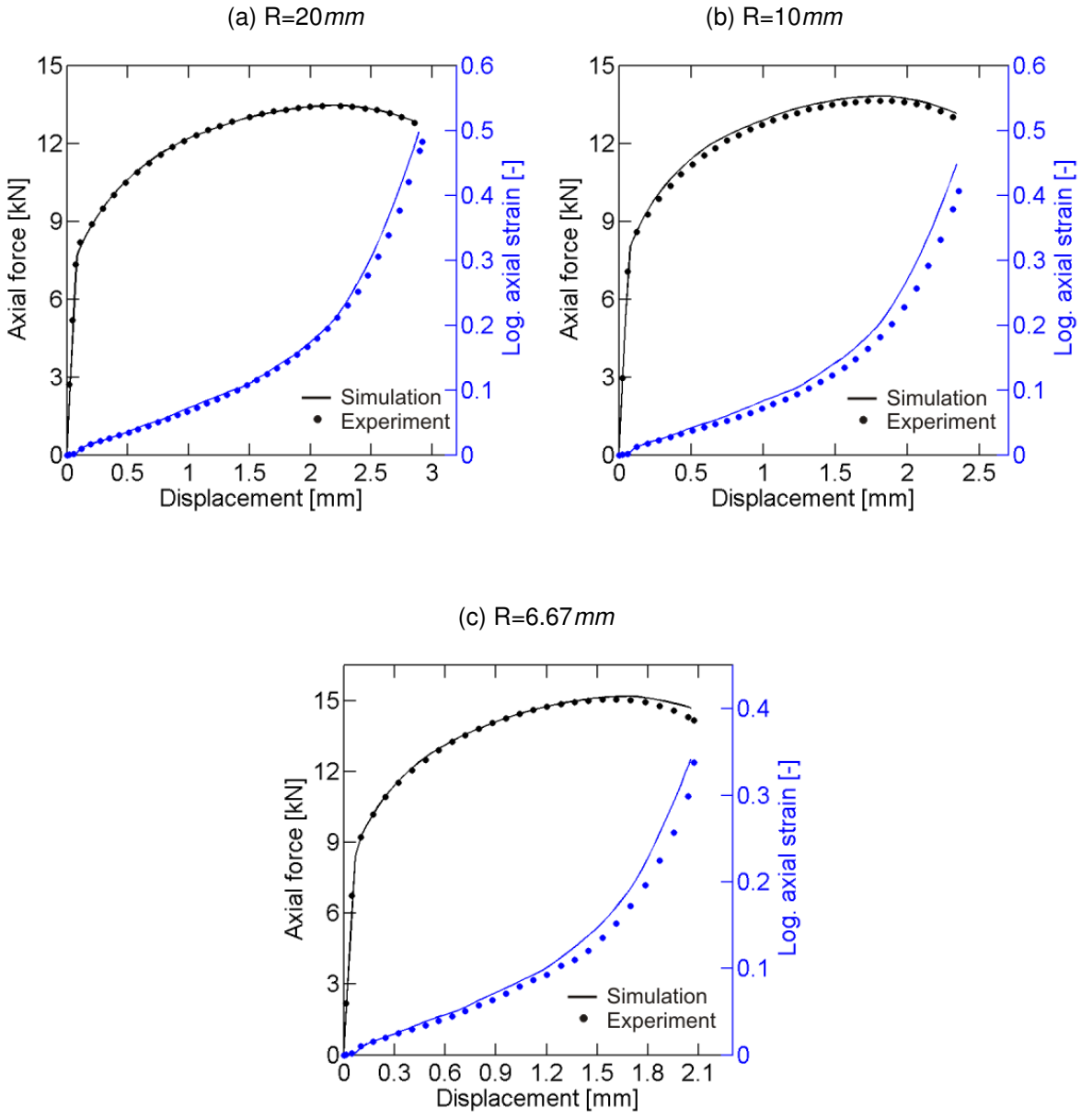

Figure 4-2: Experimental and simulation results for tensile specimen with circular cutouts. Force displacement curves are in black and central logarithmic axial strain versus displacement curves in blue.

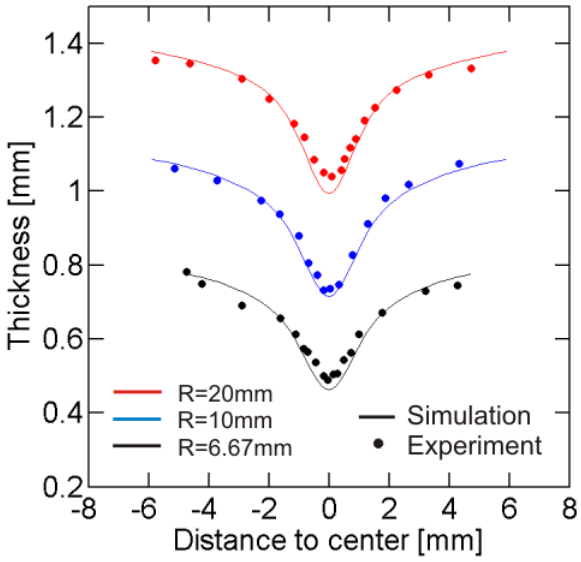

Figure 4-3: Thickness profile along the axial plane of symmetry for the 3 geometries. The curves corresponding to the 10*mm* and 6.67*mm* notched geometries are shifted by -0.3*mm* and -0.6*mm* respectively.

Notch radius [mm]	Fracture displacement		Fracture plastic strain		Stress triaxiality at fracture	
	Value [mm]	Variation [%]	Value [-]	Variation [%]	Value [-]	Variation [%]
6.67	2.048	1.28	0.422	5.09	0.626	1.90
10	2.336	1.21	0.552	5.22	0.653	1.97
20	2.887	1.22	0.585	5.38	0.614	2.43

Table 4-1: Experimental results and fracture predictions for the tensile specimens with circular cutouts

4.2.3 Finite element model

Implicit finite element simulations are performed of each experiment using Abaqus/standard. Reduced integration eight-node 3D solid elements (type C3D8R of the Abaqus element library) are used to mesh the specimens. Exploiting the symmetry of the specimen geometry, material properties and loading conditions, only one eighth of the specimen is modeled: the mesh represents the upper right quarter of the specimen, with half its thickness (Fig. 4-4). A constant

velocity is uniformly imposed to the upper boundary. A zero normal displacement condition is imposed to the three boundaries that correspond to symmetry planes.

The effect of mesh density and time discretization on the computational predictions is studied for the R=10mm notch specimen geometry. Four meshes are considered (Fig. 4-4):

- coarse mesh with an element edge length of $l_e = 400\mu m$ at the specimen center and $n_t = 2$ elements in thickness direction (half thickness),
- medium mesh with $l_e = 200\mu m$ and $n_t = 4$;
- fine mesh with $l_e = 100\mu m$ and $n_t = 8$;
- very fine mesh with $l_e = 50\mu m$ and $n_t = 16$;

The meshes are designed such that the elements near the specimen center feature the same dimension in all three spatial directions. In addition to solid element simulations, we make use of first-order plane stress shell elements (S4R) with five integration points in the thickness direction. The simulations are run up to the fracture displacement. Forty equally spaced time increments are used. The corresponding force-displacement curves as well the evolution of the equivalent plastic strain at the center of the specimen with respect to displacement are plotted in Fig. 4-5. The force-displacement curves lie on top of each other for all solid element meshes. However, the comparison with the results from shell element simulations shows that solid elements are required in order to provide meaningful predictions after the force maximum has been reached (after the onset of necking). Therefore, we limit our attention to the solid element simulations.

The predictions of force-displacement relationship are approximately mesh size independent, but the mesh density has a noticeable effect on the predicted strains at the specimen center. The final plastic strain computed with the coarse mesh is 7.3% lower than that for the very fine mesh. The relative error between the fine and very fine meshes being only 0.2%. Errors due to time discretization are evaluated by running a simulation on the fine mesh with 40, 60 and 90 implicit time steps. The difference in the final plastic strain between 40 and 90 steps is 0.7%, while a difference of less than 0.2% is observed for 60 time steps. In the following, all simulations of notched tensile tests are performed using at least 8 solid elements through the half-thickness and at least 60 equally spaced implicit time increments.

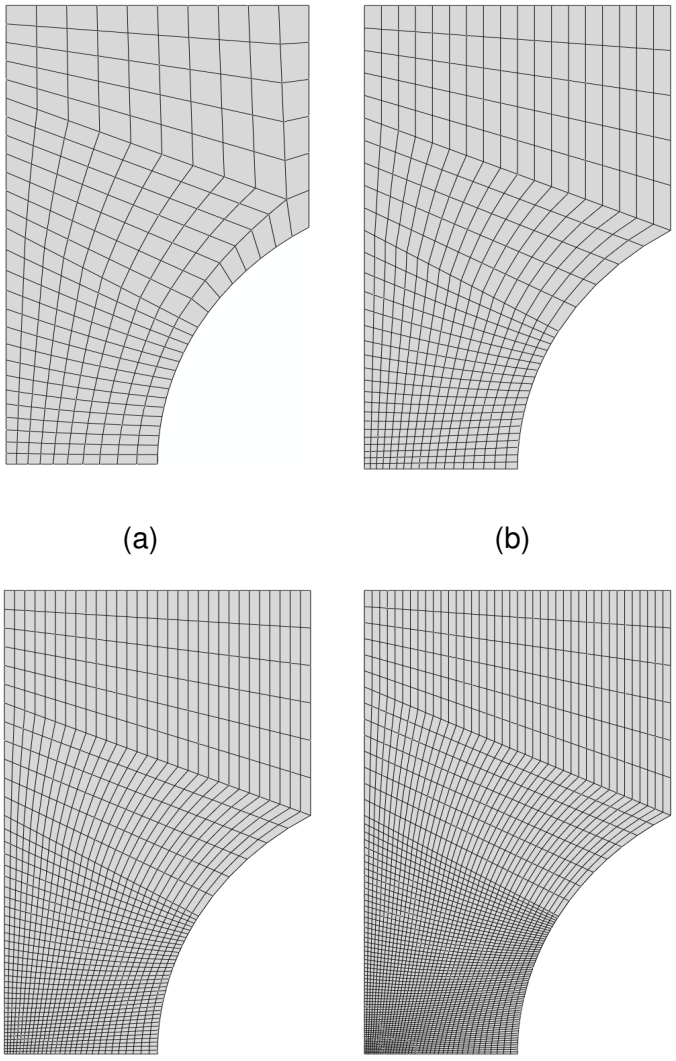

Figure 4-4: Meshes of the 10 *mm* notched radius specimen.
(a) Coarse mesh with 2 elements through half the thickness, (b) medium mesh with 4 elements through half the thickness, (c) fine mesh with 8 elements through half the thickness, (d) very fine mesh, with 16 elements through half the thickness.

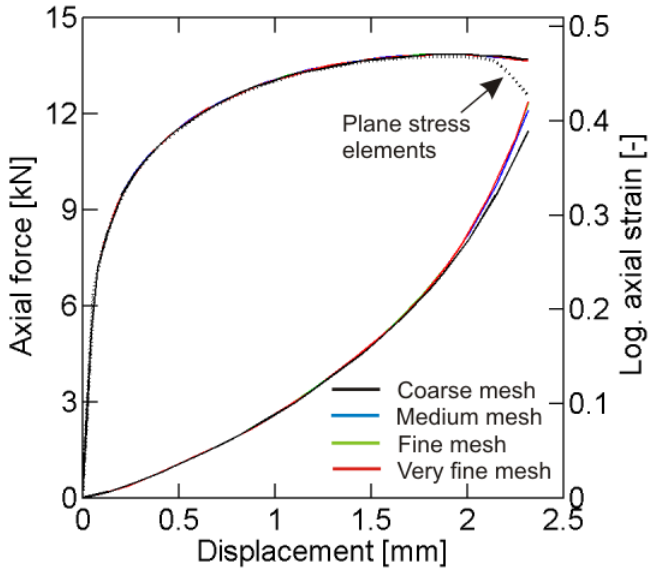

Figure 4-5: Effects of spatial discretization on the predict force and strain displacement curves for R=10*mm*

4.2.4 Extrapolation of the stress-strain curve

The Swift strain hardening curve has been validated for equivalent plastic strains of up to 0.2 (point of necking under uniaxial tension). However, in notched tensile specimens, the plastic strains at the specimen center are much higher than 0.2. The comparison of the experimentally-measured force-displacement curve for R=20*mm* (black solid dots in Fig. 4-6) with the simulation results shows that the Swift model assumption overestimates the force level (blue solid line). The assumption of a tangent modulus of $H_{min} = 0$ for strains greater than 0.2 yields an underestimation of the force level. To obtain a better extrapolation of the measured stress-strain curve, we defined two segments of constant slope H_1 and H_2; here, H_1 corresponds to the range of intermediate plastic strains (from 0.2 to 0.35), H_2 to the range of high plastic strains ($\bar{\varepsilon}^p$ higher than 0.35). The two strain hardening rate moduli are calibrated such that the simulation provides a good prediction of the experimentally-measured force-displacement curve (Fig. 4-6).

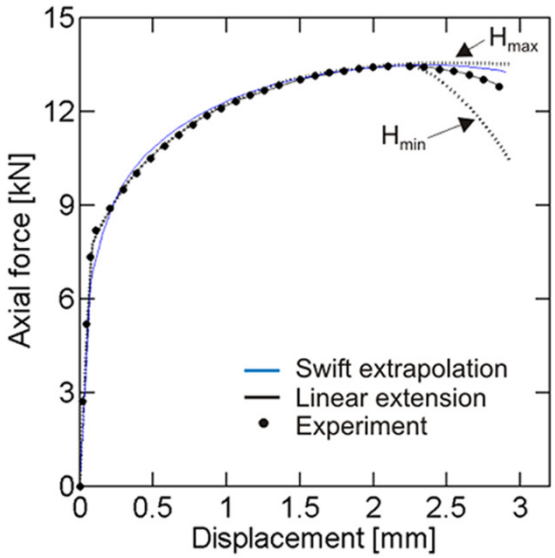

Figure 4-6: Influence of the strain hardening extrapolation on the prediction of the force-displacement curve for R=20*mm*

4.2.5 Comparison of simulations and experiments

In Fig. 4-2, we show the simulated force-displacement curves (solid black lines) all the way to fracture. The agreement with the experimental results (depicted with black dots) is very good for the 20mm (Fig. 4-2a) and 10mm (Fig. 4-2b) notch geometries. The force difference between simulation and experimental results is less than 1% in both cases. For the 6.67mm notch geometry (Fig. 4-2c), the peak of force, corresponding to the onset of localized necking, is delayed in the simulation by relative displacement of about 5%. As a result, the FEA predicted force drop is too small: the axial force at the onset of fracture is 3.7% higher in the simulation than in the experiment. The comparison of the evolution of the logarithmic axial strain at the center of the gage section with respect to the displacement (depicted in blue in Fig. 4-2) also shows a good agreement. Irrespective of the notch radius, the simulations are able to describe the characteristic increases in strain rates that have been observed in the experiments. Relative differences between simulation and DIC strains in case of the 20mm notch geometry are about 3% (Fig. 4-2a). For the 10mm notch geometry (Fig. 4-2b), the computed strain is of up to 10% higher than the DIC measurement. As far as the 6.67mm notch geometry is concerned (Fig. 4-2c), the first increase of strain rate is too large in the simulation, while the predicted strain rate increase after the onset of localized necking appears to be smaller than that given by DIC. As a

result, differences between simulated and measured strains tend to decrease at the end of the simulation, to be almost zero at fracture. Figure 4-3 depicts the thickness profile along the axial plane of symmetry of the specimens (20mm in red, 10mm in blue, 6.67mm in black). Note that both the amplitude of thickness variation and the size of the area of localization are very well predicted by the simulations.

4.2.6 Stress triaxiality and equivalent plastic strain evolution

Figures 4-7a to 4-7c show the evolution of the equivalent plastic strain as a function of the stress triaxiality at the center of the gage area. The red solid lines depict the evolution on the specimen surface, while the black solid lines show the evolution at the very center of the specimen (intersection point of all three symmetry planes). The large solid dot marks the onset of fracture that is obtained when using the average fracture displacement from three experiments. The crosses indicate the corresponding simulation results for the measured minimum and maximum displacement to fracture (see also Table 4-1). The comparison of the red and black curves clearly shows that the stress and strain state at the specimen surface is significantly different from that at the specimen mid-plane. In other words, there is a strong gradient along the thickness direction within the central zone of strain localization. The equivalent plastic strains to fracture inside the specimen are 11.5% (20*mm* notch) and 15.8% (10*mm* notch) higher inside the specimen than on the surface (see Fig. 4-8). Localized necking also leads to the development of out-of-plane stress components in the middle of the specimen (while the surface deforms under plane stress), which increases the stress triaxiality. Furthermore, the strains measured at the specimen surface are not representative for the strain to fracture of the material (red line in Fig. 4-7). It is also noted that the stress triaxiality exhibits very strong variations during loading. For instance, for R=20mm it increases from $\eta = 0.40$ before the onset of localized necking to $\eta = 0.61$ at the onset of fracture.

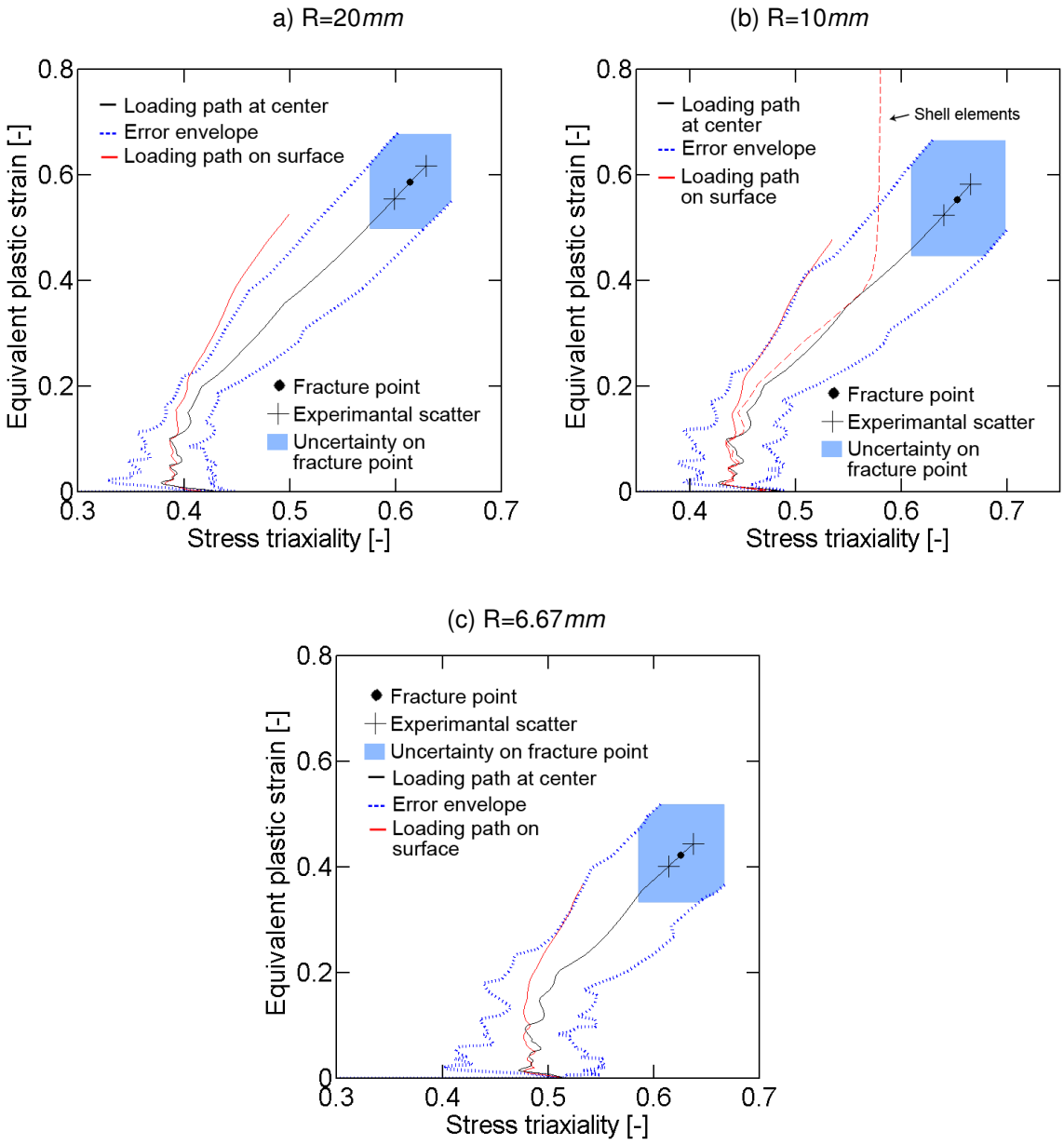

Figure 4-7: Loading paths at the center of the notched specimens.

The red solid line depicts the loading path at the surface, the black solid line at the mid-plane; black dots and the crosses highlight the onset of fracture including experimental scatter (min/max). The dashed blue lines show the error envelopes.

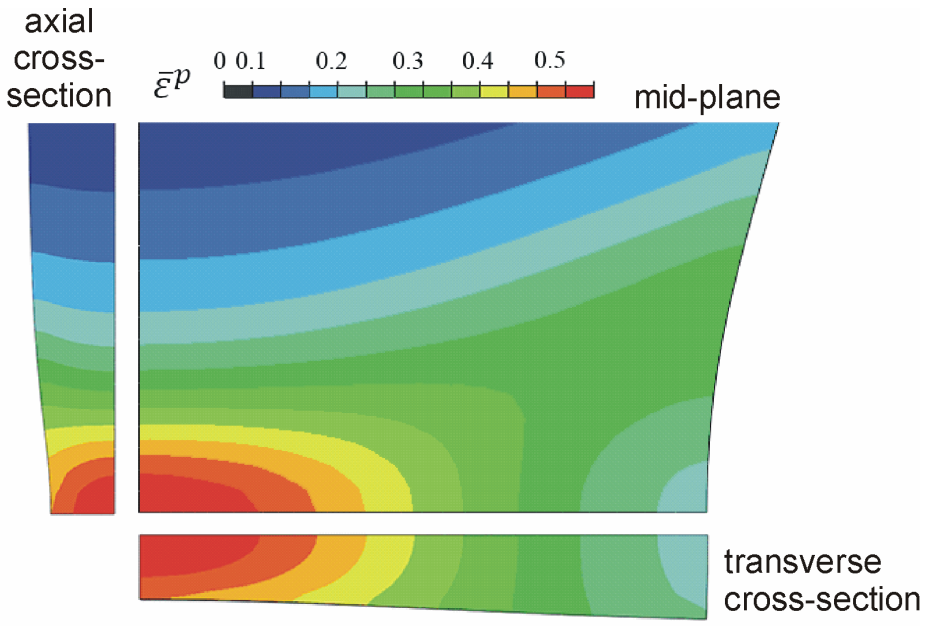

Figure 4-8: Contour plot of the equivalent plastic strain at the instant of the onset of fracture in the notched specimen with R=10*mm*

4.2.7 Uncertainty analysis

Three different types of errors affecting both the plastic strain and the stress triaxiality at the onset of fracture are summarized in Table 4-2. Considering DIC accuracy and camera resolution, the relative displacement of the specimen boundaries is measured in all experiments with an accuracy of 2.5μm. Due to the strain localization at the center of the specimen, the errors in the fracture displacement translate to even larger errors in the fracture strain. This small uncertainty in the measured fracture displacement (relative error of about 0.1%) leads to an error of about 0.004 on the fracture strain and 0.002 on the stress triaxiality at the onset of fracture.

Errors due to the inaccuracy of the constitutive model are computed according to Eq. (3.2). For all three specimen geometries, the estimated error $\delta\bar{\varepsilon}^p$ on the plastic strain is less than 0.03 at the onset of localized necking and reaches 0.063 at the point of fracture for the 20mm notch geometry (0.083 and 0.073 for the 10mm and 6.67mm geometries, respectively). This emphasizes the difficulty of modeling the post necking behavior of the specimen with great accuracy. According to Eq. (3.7), this corresponds to errors on the stress triaxiality at the onset of fracture of 0.025 for the 20mm geometry, 0.036 for R=10mm and 0.032 for R=6.67mm. The errors affecting the plastic strain versus stress triaxiality curves are depicted in Figs. 4-7a to 4-7c by

dashed blue lines. Those lines can be seen as the upper and lower boundaries on the evolution of the actual material state in the stress triaxiality/plastic strain space at the fracture locus. Colored areas surrounding fracture points depict the uncertainty on the actual fracture point due to both errors (plus experimental scatter). Those areas represent the precision achievable when determining the material state at the onset of fracture using tensile specimens with circular cutouts. Note that errors affecting stress triaxiality are very important for small strains, even if strain errors are then very small. According to Eq. (3.7), $\delta\eta$ is proportional to the current strain hardening modulus $H(\bar{\varepsilon}^p)$; the latter is very high for small strains, but decreases monotonically as the strain increases (e.g. $H = 8100MPa$ for $\bar{\varepsilon}^p = 0.01$ and $H = 400MPa$ for $\bar{\varepsilon}^p = 0.5$).

To illustrate the large error associated with the use of shell elements, we added a red dashed line to Fig. 4-7b which shows the predicted loading path evolution from a shell element simulation. The loading path agrees well with the solid element simulation prior to necking, whereas the predicted strain increases to unrealistically high values after the onset of necking.

Notch radius [mm]	Fracture plastic strain			Stress triaxiality at fracture		
	Displacement error [-]	Modeling error [-]	Total error [-]	Displacement error [-]	Modeling error [-]	Total error [-]
6.67	$0.34\ 10^{-2}$	$7.31\ 10^{-2}$	$7.65\ 10^{-2}$	$0.14\ 10^{-2}$	$3.16\ 10^{-2}$	$3.30\ 10^{-2}$
10	$0.43\ 10^{-2}$	$8.34\ 10^{-2}$	$8.77\ 10^{-2}$	$0.17\ 10^{-2}$	$3.57\ 10^{-2}$	$3.74\ 10^{-2}$
20	$0.46\ 10^{-2}$	$6.34\ 10^{-2}$	$6.80\ 10^{-2}$	$0.17\ 10^{-2}$	$2.55\ 10^{-2}$	$2.72\ 10^{-2}$

Table 4-2: Errors in the evaluation of the plastic strain and stress triaxiality at the onset of fracture

4.3 Circular punch test

The circular punch test is a standard sheet metal forming test that characterizes the formability of sheet materials under stress states that are close to equi-biaxial tension. Analogously to our analysis of the notched tensile test, we assess the accuracy of the circular punch test.

4.3.1 Experimental procedure

The circular sheet specimen is clamped on a circular die and subsequently loaded through a hemispherical punch. The punch and die have a diameter of 44.5*mm* and 100*mm*, respectively. The clamping pressure is applied through eight M10-12.9 screws. The experiment is carried out in a universal testing machine (MTS, Model G45) at a constant punch velocity of 5*mm/min*. In order to limit the effects of friction, a stack of six oil-lubricated $90\mu m$ thick Teflon layers is put between the specimen and the punch during each test.

Three-dimensional Digital Image Correlation (Vic3D, Correlated Solutions) is used to measure the out-of-plane deformation of the specimen. In our vertical experimental set-up, the clamping die is fixed on a special metal frame (Walters, 2009). A leaning mirror is integrated into that frame to record pictures of the speckle-painted bottom surface of the specimen with two digital cameras. The cameras see the specimen at a distance of 2.5*m* at an angle of 20° from the punching direction. Each camera records about 300 pictures during the test; the edge length of a square pixel is about $100\mu m$. The displacement field is calculated by DIC for the entire free surface of the specimen assuming an affine transformation of the 21x21pixels neighborhood of each point. The interpolation of the gray values is performed with a 6-tap filter. The logarithmic strain field is then calculated by averaging the displacement gradient over an area of 11x11 pixels.

4.3.2 Experimental results

The measured cross-head displacement includes the deformation of the clamping fixture as well as the deformation of the punch and the testing frame in addition to the effective punch displacement. Since the punch behaves like a non-linear spring (because of the increasing contact area between the punch and the specimen) it is difficult to extract the displacement associated with permanent deformation of the specimen from these measurements. Moreover, we observed that most of the Teflon layers are torn apart during the punching which may be considered as permanent deformation of the testing device. The initial thickness of the Teflon stack is 0.55*mm*, but we measure a final thickness of 0.12*mm* after the experiment. In order to eliminate these

experimental uncertainties in the punch displacement measurements, we present most experimental results as a function of the punch force instead of the punch displacement.

Figure 4-9 depicts the evolution of the maximum principal true strain on top of the dome measured by DIC. Observe that the applied force reaches a plateau in this displacement controlled experiment. Fracture initiates on top of the dome which indicates that friction was close to zero in this experiment. After fracture initiation, cracks propagate along the rolling direction of the sheet. Both measured principal strains at the apex of the deformed specimen exceed 0.4 at the onset of fracture. Post-mortem analysis revealed that the sheet thickness is reduced by almost 60%, from 1.43*mm* (initial) to 0.58*mm* (final).

In addition to measuring the strain at the specimen apex, the DIC measurements are used to verify two important features of this experiment. Firstly, the DIC measurements demonstrate that the radial displacements are negligibly small along the interface between the specimen and the clamping ring (less than 0.05mm). Secondly, the DIC measurements demonstrate that the strain maximum prior to fracture is located at the specimen center which re-confirms that friction effects have been successfully eliminated by the lubricated Teflon layers (Burford et al., 1991).

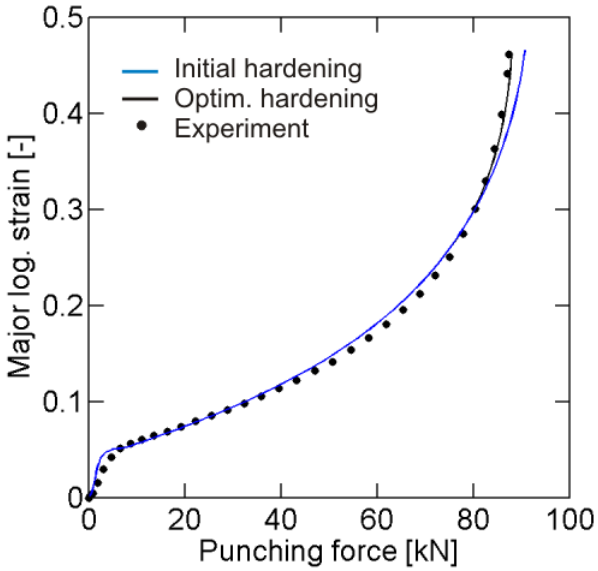

Figure 4-9: Punch test experimental results.
Evolution of the major logarithmic strain on the specimen surface as a function of the punch force

4.3.3 Numerical modeling

A quarter of the mechanical system is modeled because of the symmetry of the punch experiment and the orthotropic material behavior. Eight-node reduced-integration solid element meshes are employed in conjunction with the implicit solver of Abaqus. In addition, we make use of a shell element mesh along with the explicit solver of Abaqus because of the high computational efficiency of the shell contact formulation. In all FE models, the punch and the die are modeled as rigid bodies. The portion of the specimen that is clamped in the die is limited to 5*mm* in the simulation (i.e. the diameter of the circular specimen in the FE model is 110mm). The displacements of all nodes located on the outer edge of the specimen are set to zero. A condition of zero-normal displacement is imposed along the two edges that correspond to planes of symmetry. For shell meshes, no rotation around the edge direction is allowed on those two boundaries. A frictionless node-to-surface contact is defined between the punch and the specimen. In the case of shell elements, contact is defined for the sheet surface while thickness variations are taken into account. A constant velocity is applied to the punch, while the die is fixed in space.

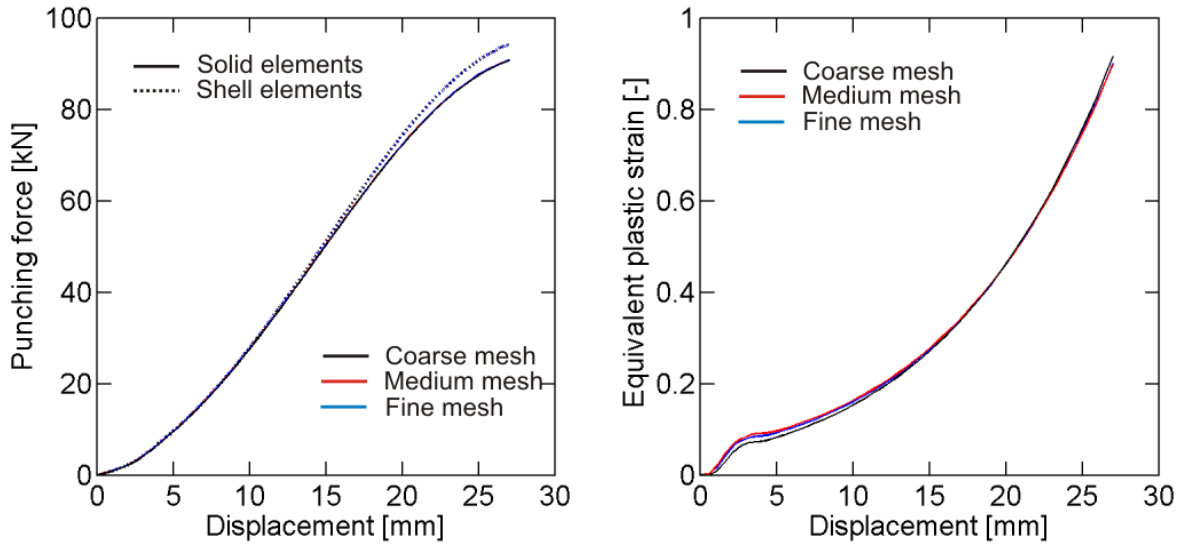

Figure 4-10: Punch test modeling.
Influence of the mesh density on the force displacement curve and on the equivalent plastic strain versus displacement curve. Results for solid and shell elements are depicted with solid and dashed lines, respectively

The predicted force-displacement curves from an implicit simulation with 100 time steps using a coarse mesh (60/3 solid elements along the radial/thickness direction), an intermediate mesh (120/6) and a fine mesh (240/12) all lie on top of each other (Fig. 4-10). Similarly, the results from quasi-static explicit simulations with shell elements (using the same number of integration points through-the-thickness as solid elements along that direction) are all identical. However, there is a noticeable difference between shell and solid element simulations for large punch displacements. This difference may be attributed to the errors associated with the assumption of plane stress and zero plastic out-of-plane shear strains in the shell element formulation. Analysis of the solid element simulations reveals that the out-of–plane compression stress reaches $90MPa$ on the contact surface with the punch; the maximal out-of-plane logarithmic shear strain is about 0.035. Unlike the results for the force-displacement curves, the solid element model predictions of the equivalent plastic strain feature a weak mesh size effect. At the center, the final equivalent plastic strain reaches 0.92 for a coarse mesh, whereas it is 0.90 for a fine mesh. Between a medium and fine mesh, the relative difference is almost zero. The results from implicit simulations with different numbers of time steps (65, 100, 150 and 200) revealed only small differences. The final maximal equivalent plastic strain reaches 0.92 when using 65 time steps and 0.90 for 200 steps.

Based on our brief analysis, the punch experiment will be analyzed using a finite element model with (i) 120 solid elements along the radial direction, (ii) 6 solid elements in thickness direction, (iii) 100 implicit time steps, and (iv) frictionless kinematic node-to-surface contact.

4.3.4 Identification of strain hardening response

When plotting the evolution of the major principal strain at the center of the specimen as a function of the punching force (Fig. 4-9), it becomes apparent that the simulation model (blue curve) underestimates the strain in comparison with the experiment (solid black dots). Recall that the hardening curve used in the simulation has been calibrated based on the experimental results from uniaxial and notched tensile tests. However, since the maximum equivalent plastic strain reached in a punch test (about 0.9) is still much larger than that reached in a notched tensile test (about 0.6), we may improve the extrapolation of the stress-strain curve for large strains. Here, a

third linear hardening segment is introduced for $\bar{\varepsilon}^p > 0.6$. The best correlation between simulation and the punch experiment is achieved when using a hardening modulus of H_3=100MPa in this third segment. The corresponding simulation result is depicted as a black solid line in Fig. 4-9. It is emphasized that this modification of the hardening curve does not affect the results from the previous section on notched tensile tests.

4.3.5 Simulation results and uncertainty analysis

The numerical simulation is performed up to the instance where the computed surface strain equals the measured surface strain at the onset of fracture ($\varepsilon = 0.461$). The simulated curve shows very good agreement with the experimental results (depicted with black dots). Furthermore, the predicted thickness reduction is in excellent agreement with the experiment. Figure 4-11 depicts the evolution of the equivalent plastic strain as a function of the stress triaxiality (black curve); here, it is assumed that fracture initiates on the free specimen surface. The loading state at the onset of fracture is depicted as a black dot. Fracture occurs at a computed stress triaxiality of $\eta = 0.66$ (equi-biaxial tension).

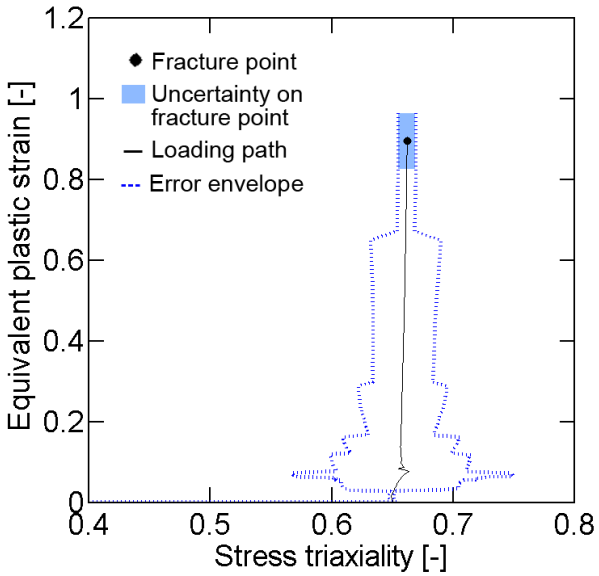

Figure 4-11: Loading paths on the outer surface of the punched specimen.
The black dot indicates the onset of fracture, the dashed blue lines shows the error envelope.

Fracture plastic strain		Stress triaxiality at fracture	
Value [-]	Error [-]	Value [-]	Error [-]
0.896	$6.86\ 10^{-2}$	0.662	$0.73\ 10^{-2}$

Table 4-3: Fracture point and error estimation for the circular punched specimen

The modeling error affecting the computation of the equivalent plastic strain and the stress triaxiality is evaluated according to Eqs. (3.2) and (3.7); it is shown by blue dashed lines in Fig. 4-11. Modeling errors at the onset of fracture are summarized in Table 4-3. A complete evaluation of the errors affecting the hybrid experimental-numerical result would require evaluating the precision of the 3D DIC method. However, the authors could not identify such an evaluation in the open literature. For the case of one-dimensional DIC, Sutton et al. (2009) reported that the 6-tap optimized filter interpolation function does not produce any significant error. Thus, we neglect this source of error in our analysis.

4.4 Tensile specimen with a central hole

Conventional uniaxial tensile specimens develop a pronounced neck at large strains which yields to a change in stress state throughout the experiment from uniaxial tension to transverse plane strain. In an attempt to keep the stress triaxiality more constant throughout the experiment, we make use of tensile specimens with a central hole. The presence of a central hole creates a strain concentration which favors the fracture initiation at the intersection of the hole and the transverse axis of symmetry of the specimen.

4.4.1 Experimental procedure

The tensile specimens are 20*mm* wide and feature an 8*mm* diameter circular hole at the center (Fig. 4-12). For the first set of specimens, the central hole is cut using a water-jet. In order to obtain a better edge finish, we prepared a second set of specimens with a 7mm diameter water jet cut hole that is subsequently enlarged to 8mm using CNC milling (with a 0.125” diameter end

mill). The experimental procedure follows closely the program outlined for the notched specimens. To evaluate the error in the computed strains, we determined the axial logarithmic strain on the transverse symmetry axis at a distance of 40 pixels ($380\mu m$) from the hole. A measurement right at the edge of the hole is not possible as the DIC algorithm needs a continuous displacement field in the vicinity of the point of interest.

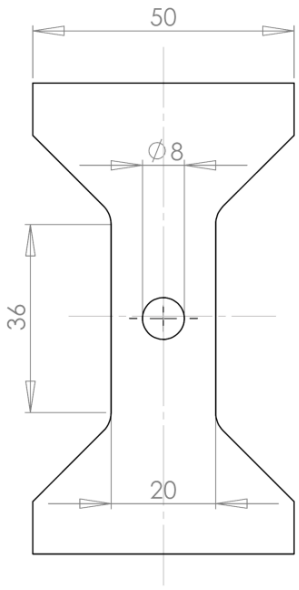

Figure 4-12: tensile specimen with central hole

4.4.2 Experimental results

The measured force-displacement curves for the two sets of specimens are shown in Fig. 4-13 as crosses for the waterjet cut specimens and as solid dots for the CNC milled specimens. The waterjet-prepared specimens are extracted from a slightly thinner part of the sheet (1.46*mm* instead of 1.5*mm*), resulting in a lower force displacement curve. The measurements demonstrate that the machining technique has a strong influence on the fracture displacement. It is about 2.1*mm* for CNC-milled specimens and only 1.7*mm* for the waterjet cut specimens. The waterjet cuts the sheet by abrasion (abrasive jet), which leaves a non-smooth edge with numerous geometric defects. It is speculated that those defects along with some residual plastic strains are responsible for the premature failure of the water-jet cut specimens. Consequently, the results for water-jet cut specimens are discarded in the following analysis.

The force-displacement curve (Fig. 4-13) exhibits a peak before fracture occurs. An important width reduction (diffuse necking) is observed within both specimen ligaments (Fig. 4-14), which appears to intensify as the force reaches its maximum. The displacement to fracture varies among the CNC-milled specimens (Table 4-4). Observe from Fig. 4-15 that axial strain field features steep gradients around the transverse axis of symmetry of the specimen. The evolution of the surface strain (blue curve in Fig. 4-13) shows that the surface strain reaches values of up to 0.7 prior to fracture.

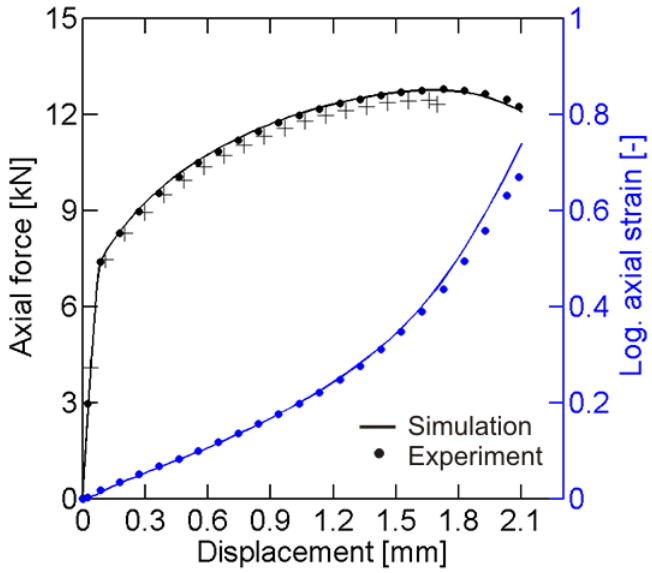

Figure 4-13: Experimental and simulation results for the tensile specimen with a central hole Force-displacement curves and logarithmic strain versus displacement curves from experiments (dots = CNC-machined, crosses = waterjet cut) and simulation (solid lines)

Figure 4-14: Specimen with a central hole after crack initiation

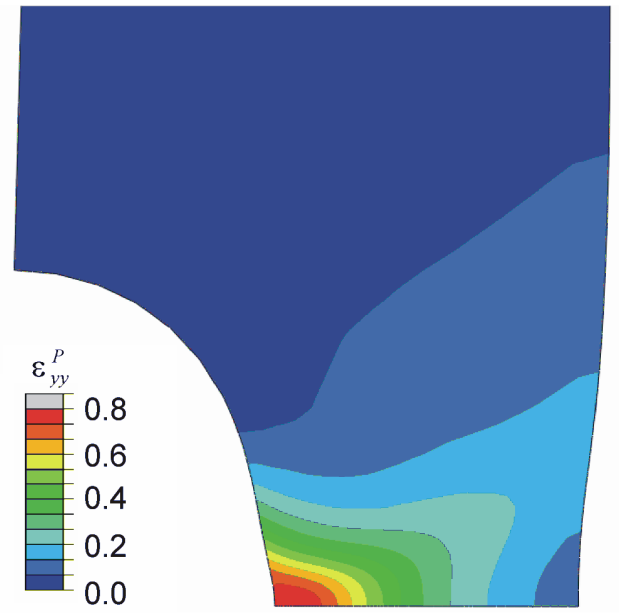

Figure 4-15: Logarithmic axial strain computed on specimen surface at the instant of the onset of fracture on a specimen with a central hole

Fracture displacement		Fracture plastic strain		Stress triaxiality at fracture	
Value [mm]	Variation [%]	Value [-]	Variation [%]	Value [-]	Variation [%]
2.089	2.24	0.834	6.67	0.282	1.45

Table 4-4: Experimental results and fracture predictions for the tensile specimen with central hole

4.4.3 Numerical modeling

Based on the results from Paragraph 3.3, eight-node solid elements (with reduced integration) are used to mesh one eighth of the specimen (Fig 4-16). A constant velocity is applied to the upper boundary. A zero normal displacement condition is imposed to the three boundaries corresponding to symmetry planes. Since the experimental results indicate that through-the-thickness localization is less important with this specimen design than for notched tensile specimens, we assume that 8 elements through the half thickness are enough to describe the stress and strain variations along the thickness direction. However, we use a biased mesh with the

smallest elements at the intersection of the hole with the transverse plane of symmetry (Fig. 4-16). In this vicinity, the elements have also the same length in the axial and transverse directions. Implicit simulations are performed using a coarse mesh (smallest in-plane element edge length is $120\mu m$), a medium mesh ($60\mu m$) and a fine mesh ($30\mu m$). As for the notched tensile tests, we find the same force-displacement curves for all mesh sizes. The effect of mesh size on the equivalent plastic strain is also weak for the element located at the hole boundary (on the specimen mid-plane). The final equivalent plastic strain computed with the coarse mesh is 0.83 compared to 0.86 when using the fine mesh. Errors due to time discretization are also evaluated by running simulations with 50, 75, 100 and 150 time increments. The difference in final plastic strain is already negligible (0.004) when comparing the results for 75 and 100 time increments. Thus, we make use of the implicit analysis with 75 time steps and a medium mesh to determine the loading history to fracture.

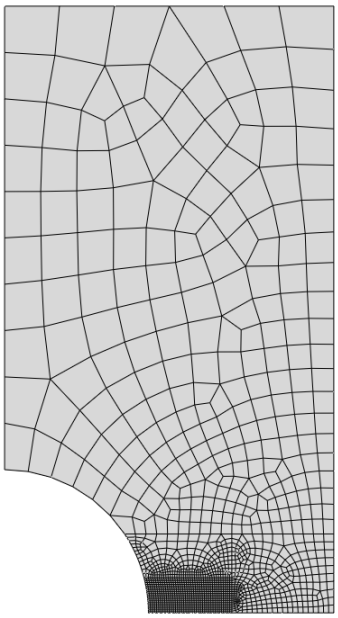

Figure 4-16: medium FE mesh for the specimen with a central hole

4.4.4 Numerical results and error estimation

The simulated force-displacement curve is depicted as a black solid line in Fig. 4-13. It is in excellent agreement with the experimental data (solid dots). The maximum difference between the experimentally-measured and numerically-predicted force level is smaller than 2%. This good

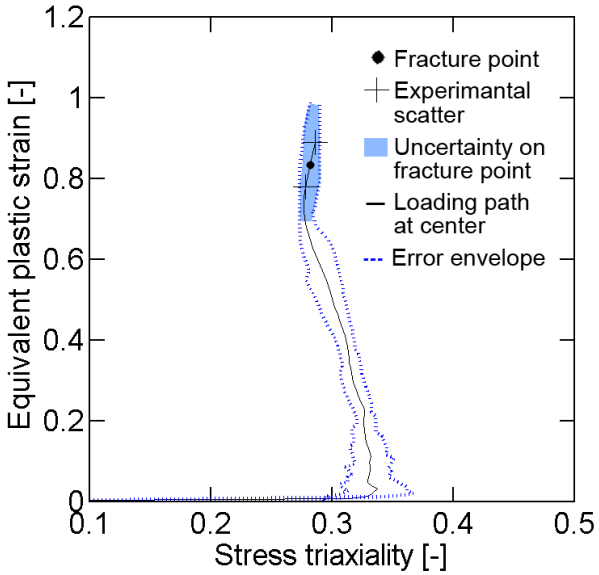

Figure 4-17: Analysis of a tensile test with a central hole
Loading path at the center of the specimen (black solid line); the black dot and the crosses highlight the onset of fracture including experimental scatter (min/max). The dashed blue lines show the error envelopes.

correlation is seen as a validation of the strain hardening curve that has been determined from the notched tension and punch tests. The FEA predicted evolution of the surface strain (blue line in Fig. 4-13) is also close to the DIC measurements (blue dots). Similar to the results for notched tensile tests, the strains computed by FEA are higher than the DIC measurements. Here, the final computed strain is overestimated by about 10%.

The evolution of the equivalent plastic strain as a function of the stress triaxiality is shown in Fig. 4-17. The black solid dot highlights the instant of onset of fracture. The differences due to scatter in the measured fracture displacement is represented with solid crosses. The identified fracture strain as well as the stress triaxiality at the onset of fracture are summarized in Table 4-4 along with the corresponding error estimates.

As compared to the results for notched tensile specimens, the stress triaxiality variations in the tensile specimen with a central hole are small. It varies between 0.277 and 0.338. At the onset of fracture, the stress triaxiality is $\eta = 0.282$ which is close to uniaxial tension ($\eta = 0.33$). The estimated equivalent plastic strain to fracture is 0.83. The relative displacements of the specimen boundaries are computed with a precision of $2.5\mu m$ which translates into an uncertainty of 0.002

for the fracture strain and of less than is 0.001 for the stress triaxiality. The modeling errors according to Eqs. (3.2) and (3.7) are 0.095 for the fracture strain and 0.004 for the stress triaxiality.

Fracture plastic strain			Stress triaxiality at fracture		
Displacement error [-]	Modeling error [-]	Total error [-]	Displacement error [-]	Modeling error [-]	Total error [-]
$0.22\ 10^{-2}$	$9.49\ 10^{-2}$	$9.71\ 10^{-2}$	$0.03\ 10^{-2}$	$0.43\ 10^{-2}$	$0.46\ 10^{-2}$

Table 4-5: Errors in the evaluation of the plastic strain and stress triaxiality at the onset of fracture in the tensile specimen with a central hole

4.5 Discussion and recommendations

4.5.1 Identification of the strain hardening response

The proper identification of the strain hardening model for very large strains is critically important for the reliable determination of the fracture strains. It is emphasized that conventional extrapolation formulas such as the modified Swift model seem to provide a poor approximation of the strain hardening behavior of advanced high strength steels at large strains. The present study shows that the Swift assumption leads to substantial errors in the simulation results after the onset of necking which is consistent with earlier results on martensitic steel (Mohr and Ebnoether, 2009). When hydraulic bulge testing devices are not available or a bulge test is impossible to realize (because of the very large specimen size), we propose the following procedure to identify the strain hardening function $H(\bar{\varepsilon}^p)$:

(i) Uniaxial tensile testing of dogbone specimens up to the strain of necking (ASTM E8, 2004);

(ii) Uniaxial testing of a tensile specimen with a central hole; the stress-strain curve can then be identified through inverse calibration;

One may also model the post-necking behavior of uniaxial tensile test and determine the stress-strain curve from inverse analysis (e.g. Mohr and Ebnoether, 2009). However, since the stress state in the neck of a uniaxial tension specimen is close to transverse plane strain, the maximum equivalent plastic strain achieved using a uniaxial tensile specimen with a central hole is expected to be larger. Furthermore, the stress gradients through the sheet thickness are smaller for the later type of specimen. From an experimental point of view, we note that location of the zone of localization is a priori known when using a specimen with a central hole. This allows for the proper positioning of the DIC system before the experiment. Note that in a uniaxial tensile test, the position of the emerging neck is unknown before the experiment and may thus occur outside the field of vision of the camera system.

4.5.2 Numerical modeling

Shell element simulations provide accurate predictions of the large deformation behavior of sheet metal structures before the onset of through-the-thickness necking. However, the strain and stress state predictions of shell element simulations after the onset of through-the-thickness necking are not reliable as out-of-plane stresses become important. The same limitation becomes apparent under the presence of high surface pressures (e.g. final phase of the punch test). Thus, we strongly recommend using solid element meshes to determine the stress and strain histories all the way to fracture. When evaluating the effect of mesh density on the simulation results, it is important to monitor the strain evolution within the zone of localization. The global force-displacement curves are usually not mesh size sensitive since the material within the zone of localization contributes only little to the “internal energy” (elastic strain energy plus plastic dissipation) of the entire structure. As a rule of thumb, we recommend sixteen first-order solid elements through the full thickness of the sheet.

4.5.3 Summary of the loading paths to fracture

Figure 4-18a summarizes the results from all simulations in a single graph of equivalent plastic strain versus stress triaxiality. Recall that the critical element (integration point) is positioned on the sheet mid-plane for the notched tensile specimens and the specimen with a

central hole, while it is located on the specimen surface for the punch experiment. We observe the high ductility for stress states close to uniaxial tension and those close to equi-biaxial tension. The strain path for the notched tensile specimen features stress states close to transverse plane strain which exhibit the lowest ductility. As an alternative to showing the results in the $(\eta, \bar{\varepsilon}^p)$-plane, we also computed the loading paths to fracture in terms of the principal plastic strains in the plane of the sheet. The minor and major strains shown in Fig. 4-18b are calculated from the in-plane components of the plastic strain tensor. Note that these strains are different from the eigenvalues of the plastic strain tensor (unless the out-of-plane shear strain components are zero).

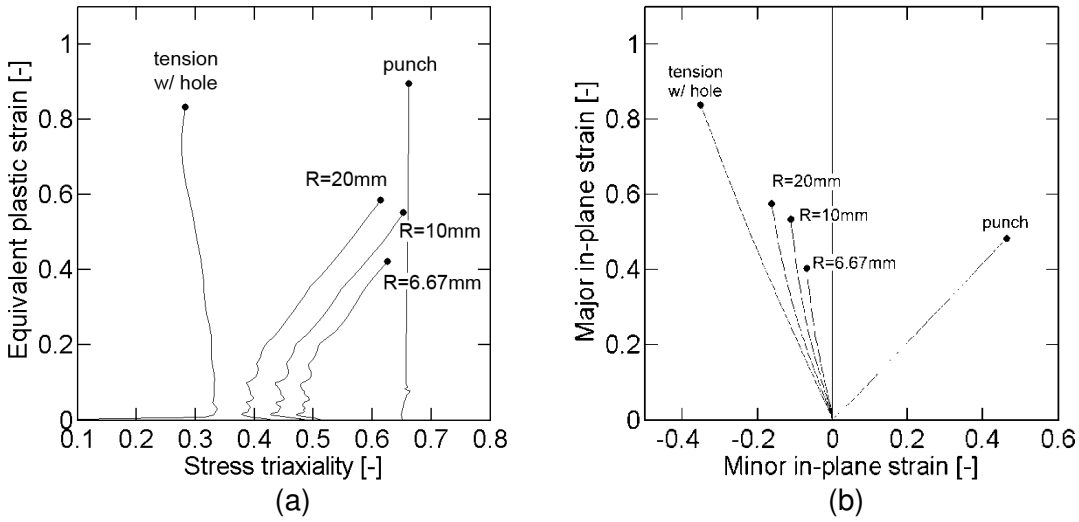

Figure 4-18: Stress and strain histories for the 5 geometries
(a) in the stress triaxiality versus equivalent plastic strain space,
(b) in the in-plane major strain versus in-plane minor strain space.

4.5.4 Effect of porosity

All numerical results presented in this paper are obtained under the simplifying assumption that the effect of (micro-)porosity evolution on the effective plastic behavior can be neglected. There is strong theoretical evidence that the evolution of porosity changes the predicted stress triaxialities (e.g. Danas and Ponte Castaneda, 2009a). However, it is difficult to quantify the effect of porosity on the plastic behavior of the TRIP780 steel based on our macroscopic measurements (surface displacement fields and total force). At the same time, the numerical predictions of the non-porous plasticity model employed in this study agree well with all macroscopic measurements for various loading conditions.

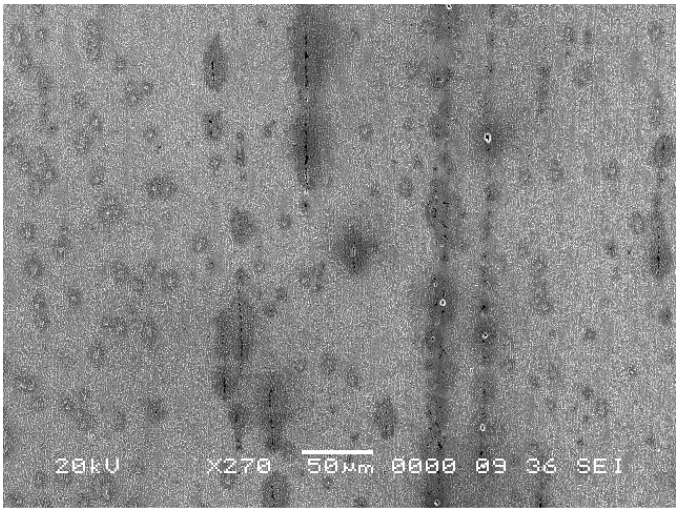

(a)

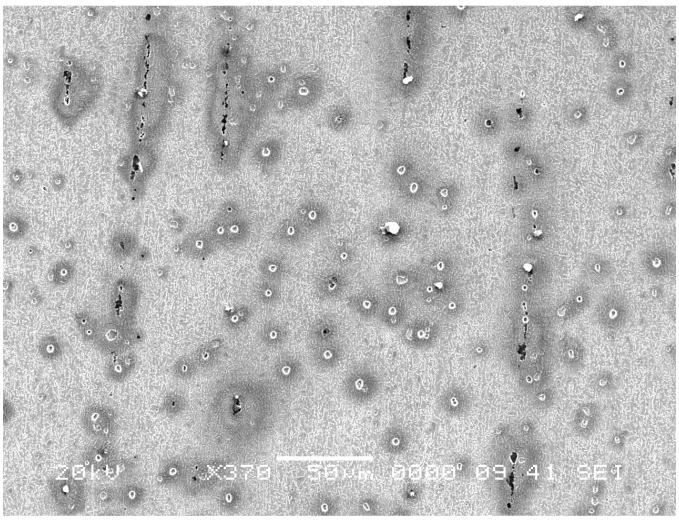

(b)

Figure 4-19: Micrographs of the axial plane of symmetry of deformed notched tensile specimens. (a) R=*20mm notch* specimen strained to 98.3% of the fracture displacement, (b) R=6.67 *mm* notch specimen strained to 96.8% of the fracture displacement. The vertical and horizontal directions of the pictures correspond to the axial and thickness directions of specimen, respectively.

The evolution of porosity clearly plays an important role as far as the onset of fracture is concerned. The initial microstructure is void free, but micrographs of highly deformed specimens indicate that voids initiate and grow throughout loading. Figure 4-19 shows micrographs of the axial plane of symmetry at the center of the notched specimens prior to fracture (after applying about 97% of the displacement to fracture). Voids and microcracks are clearly visible at this stage of deformation. Observe that the microcracks are aligned with the loading direction. This

observation may be explained using the anisotropic porous plasticity model of Danas and Ponte Castaneda (2009b). Their homogenization-based computations show that the severe elongation of initially spherical voids under transverse plane strain loading causes the loss of ellipticity of the effective porous medium. In other words, the axial microcracks may be considered as the result of the coalescence of highly elongated voids. However, in the present case, the onset of fracture is also affected by material heterogeneities at the microstructural level. Energy dispersive X-ray analysis revealed that the locations of the microcracks seen in Fig. 4-19 coincide with the position of Mn and Mo segregation bands.

4.6 Conclusion

Five different fracture tests have been performed on full thickness specimens extracted from TRIP780 sheets and analyzed in great detail to obtain reliable estimates of the loading path to fracture for stress triaxialities ranging from uniaxial tension to equi-biaxial tension. The main conclusions are:

(1) Shell element simulations are not suitable for the evaluation of the local loading path after the onset of through-the-thickness necking.

(2) Solid element simulations can provide accurate predictions. Both coarse and fine meshes predict usually the same overall force-displacement response, but it is important to evaluate the accuracy of an FE simulation through the comparison of the predicted strains within the neck with DIC surface strain measurements. For the present material and loading conditions, sixteen first order solid elements along the thickness direction provided sufficiently accurate results for the local fields.

(3) It is important to identify the strain hardening curve for large strains from experiments. The analytical extrapolation (e.g. Swift law) based on data for uniaxial tension prior to necking is not sufficiently accurate. When data from hydraulic bulge tests is not available, we recommend the inverse identification

of the stress-strain curve using the results from the testing of uniaxial tensile specimen with a large central hole.

(4) The stress-triaxiality is approximately constant all the way to fracture for a tensile specimen with a central hole and during a punch test; it increases monotonically throughout notched tensile tests.

Chapter 5.

Fracture Testing under Combined Normal and Shear Loading

5.1 Introduction

In sheet metal forming, the failure of the sheet metal is typically predicting using Forming Limit Diagrams (FLDs), e.g. Keeler et al. (1964). The FLD defines the onset of necking as failure while the so-called Fracture Forming Limit Diagram (FFLD) concept has been introduced to predict the fracture after necking (Embury et al., 1977). Most experimental techniques for determining FLDs and FFLDs comprise a plurality of specimens that are inserted into a testing system of only one degree of motion. For instance, the Hasek (1978) test makes use of a family of circular specimens with different recesses that are inserted into a punch/die system. The axial motion of the punch is the only degree of freedom of the testing system. The Nakazima (1971) test relies on a similar punch/die system to load strips of different width all the way to fracture. In the hydraulic bulge test, only one type of specimen is used while different states of loading are achieved by varying the elliptical shape of the die. The common feature of these testing techniques is a single degree of freedom loading system. This degree of freedom is used to vary the intensity of loading, i.e. the position along a linear loading path. However, the loading path is preset by the combination of specimen and testing system. It cannot by changed throughout the experiment. Moreover, it is noted that none of the aforementioned testing techniques allows for the reversal of loading direction. In other words, the described experimental techniques for FLD and FFLD determination are limited to monotonic linear loading paths.

Due to this limitation, the effect of non-linear and/or non-monotonic loading paths can only be studied by these techniques when the specimens are cut from pre-deformed sheets. Laukinis

and Gosh (1978) studied the failure under uniaxial tension of equibiaxialy pre-strained aluminum killed steel and 2036-T4 Aluminum specimens. Llod and Sang (1979) performed uniaxial tensile pre-straining followed by uniaxial tension in the orthogonal direction on 2036-T4 and 5182-0 Aluminum sheets. More recently, Graf and Hosford (1994) characterized the influence of strain path changes on the FLD of 6111-T4 Aluminum sheets by pre-straining their specimens under either uniaxial, transverse plane strain or equibiaxial tension. All experimental studies reported a significant dependence of failure on strain-path changes.

Mohr and Henn (2007) proposed an experimental technique that makes use of an universal biaxial loading device to test a flat specimen under different states of loading. This technique is fundamentally different from the established FLD tests in the sense that the state of loading is varied by changing the displacement boundary conditions rather than the shape of the specimen. In conjunction with a dual actuator system (e.g. Mohr et al., 2008), this experimental technique can be employed to perform fracture tests along non-linear loading paths. The original specimen design by Mohr and Henn (2007) featured a flat gage section of uniform thickness that has been designed such that cracks are most likely to initiate within the specimen center. Bai (2008) modified this geometry by including a second curvature, the specimen featuring a non-flat gage section. Both use of the specimen by Mohr and Henn as well as the specimen by Bai in a biaxial loading device require a hybrid experimental-numerical approach to determine the stress and strain states at the onset of fracture.

In the present chapter, the original design of the specimen by Mohr and Henn (2007) is revisited. After optimizing some characteristic geometrical features, a series of experiments is performed on a TRIP780 steel and analyzed in detail. The results show that the validity of the proposed hybrid experimental-numerical technique is very sensitive to machining imperfections. Furthermore, it is shown that the local stress and strain fields within the specimen gage section cannot be computed with high accuracy at very large strains. Thus, it is recommended to interpret the fracture data from butterfly experiments as lower bounds rather than “exact”.

5.2 Specimen design

Figure 5-1 shows a schematic of the proposed fracture specimen. The specimen features a thickness jump between the gage section of thickness t and the shoulders. Different states of stress and strain may be achieved within the specimen gage section by applying different combinations of normal loading F_V and tangential loading F_H to the top and bottom specimen boundaries. An attempt is made to optimize the specimen geometry such that the cracks initiate within the flat $h \times w_c$ large central area of the gage section.

In a plane stress specimen, the stress state is always uniaxial tension along the free boundaries, irrespective of the state of stress at the specimen center. This can pose a challenge when characterizing the onset of fracture at low stress triaxialities since early cracks may initiate along the specimen boundaries rather than at the specimen center. The boundaries of the proposed specimen are curved to avoid the crack initiation at the gage section boundaries. Here, we perform a short parametric study to gain further insight into the effect of the boundary curvatures on the stress and strain distributions within the gage section.

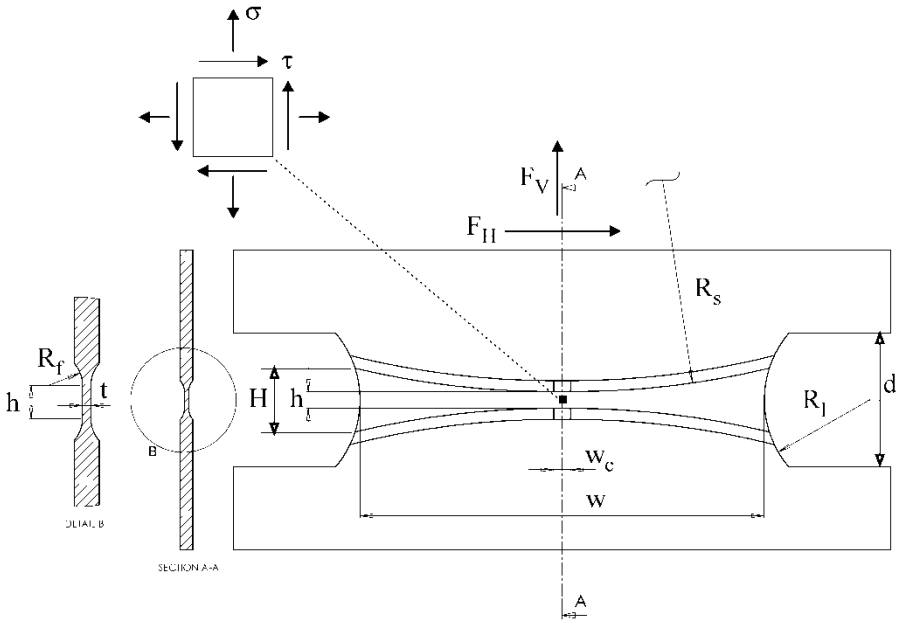

Figure 5-1: Schematic of the proposed specimen.

5.2.1 Theoretical range of loading states

The (x,y)-reference frame in Fig. 5-1 denotes the so-called machine coordinate systems. Prior to necking, the state of stress near the specimen center is plane stress in the (x,y)-plane with the superposed transverse plane strain constraint in the x-direction. For an isotropic rigid plastic Levy-von Mises solid, the corresponding stress tensor in the machine coordinate system (see Fig. 5-1) may be written as

$$\sigma = \begin{bmatrix} 0.5\,\sigma & \tau & 0 \\ \tau & \sigma & 0 \\ 0 & 0 & 0 \end{bmatrix} \tag{5.1}$$

The transverse plane strain condition implies that the strain along the specimen width direction (corresponds to x-direction in Fig. 5-1) is zero, $\varepsilon_x \cong 0$. Throughout our discussion, we use the stress triaxiality η and the Lode angle parameter $\bar{\theta}$ to characterize the stress state. The stress triaxiality is defined by the negative ratio of hydrostatic pressure $p = -tr(\boldsymbol{\sigma})/3$ and the von Mises equivalent stress, $\bar{\sigma}_{VM}$,

$$\eta = -\frac{p}{\bar{\sigma}_{VM}} = \frac{sign(\sigma)}{\sqrt{3 + 12\left(\frac{\tau}{\sigma}\right)^2}} \tag{5.2}$$

The stress triaxiality is zero for shear dominated loading ($\sigma/\tau \to 0$) while it approaches asymptotically its maximum value of $\eta = 1/\sqrt{3} \cong 0.58$ as the normal stress becomes dominant ($\sigma/\tau \to \infty$).

The Lode angle parameter $\bar{\theta}$ is defined by the ratio of the third and second stress deviator invariants,

$$\bar{\theta} = \frac{27}{2}\frac{\det(\boldsymbol{\sigma} + p\mathbf{1})}{\bar{\sigma}_{VM}^3} = \frac{\frac{27}{4}\frac{\sigma}{|\tau|}}{\left[\frac{3}{4}\left(\frac{\sigma}{\tau}\right)^2 + 3\right]^{\frac{3}{2}}} \tag{5.3}$$

Unlike the stress triaxiality, the Lode angle parameter is not a monotonically increasing function in σ/τ. We have $\bar{\theta} = 0$ for both $\sigma/\tau \to 0$ (pure shear) and $\sigma/\tau \to \infty$ (transverse plane strain tension), while it reaches its maximum of $\bar{\theta} = 1$ for $\sigma/\tau \cong 1.38$, which corresponds to uniaxial

tension. The theoretical relationship between the Lode angle parameter and the stress triaxiality for the present type of experiment is shown in Fig. 5-2. In addition, the biaxial loading angle, β, defined as

$$\tan\beta = \frac{F_V}{F_H} \cong \frac{\sigma}{\tau} \tag{5.4}$$

is depicted as curve parameter in Fig. 5-2. In this notation, $\beta = 0°$ corresponds to pure shear, while $\beta = 90°$ corresponds to transverse plane strain tension.

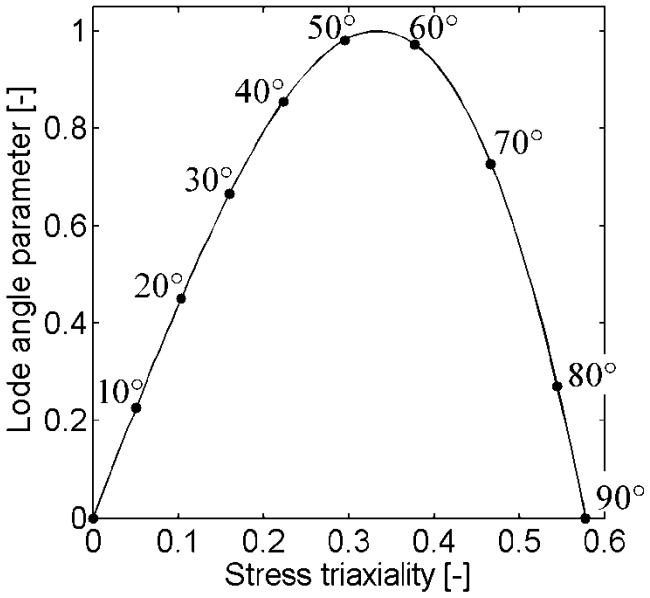

Figure 5-2: Lode angle parameter as a function of the stress triaxiality for plane stress conditions. The labels next to the solid dots indicate the corresponding biaxial loading angle.

5.2.2 Parametric study on specimen geometry

The exact geometry of the proposed fracture specimen is described by three geometric parameters: the shoulder radius R_S, the lateral radius R_L and the fillet radius R_F. The gage section thickness t and height h are not considered as a model parameter. From a theoretical point of view, the thickness does not affect the stress distribution in a plane stress specimen. The width is

important and should be as large as possible for stress field uniformity. In view of the force limitations of real testing systems, it is usually advantageous to increase the specimen width at the expense of thickness. Here, a gage section thickness of $t = 0.5mm$ is chosen. This corresponds to lower limit which can still be machined within reasonable dimensional tolerances (e.g. thickness variations of less than 5%). In order to produce transverse plane strain conditions near the specimen center, the distance h between the top and bottom shoulders needs to be small. Furthermore, the risk of buckling under shear loading may be lowered by choosing a small gage section height. In the present design, a minimum thickness of $h = 2mm$ is chosen to provide a sufficiently large flat area for two-dimensional DIC measurements.

The implicit finite element program Abaqus/standard (2007) is used to compute the stress and strain fields within specimens of different geometry. The linear plane stress elements CPS4R and CPS3 are used in two-dimensional models while the solid elements C3D8R and C3D6 are employed to discretize three-dimensional geometries. It will be shown in Section 4 that very fine meshes are needed to provide an accurate estimation of all local stress and strain fields. Within the framework of this subsection, rather coarse finite element meshes are employed; they are chosen such that the effect of various geometric features can be studied with satisfactory accuracy.

5.2.3 Effect of the shoulder curvature

The main reason for introducing the shoulder radius R_S is to reduce the amount of plastic deformation towards the free specimen boundaries to avoid premature fracture away from the specimen center. Since this problem is most critical for pure shear loadings, we performed all simulations for this loading condition. Three different radii are considered to demonstrate the effect of the shoulder curvature: $R_S = 50mm$, $R_S = 100mm$ and $R_S = 200mm$. Figures 5-3 to 5-5 show plots of the variation of the equivalent plastic strain and stress triaxiality along the x-direction at an advanced stage of deformation. Each solid dot represents the result at one integration point of the plane stress mesh. The plot of the stress triaxiality shows a narrow zone at the specimen center with very small ($\eta = 0 \pm 0.01$) variations in stress triaxiality. The width of this zone in x-direction increases as the shoulder radius increases (compare Figs. 5-3 to 5-5). The

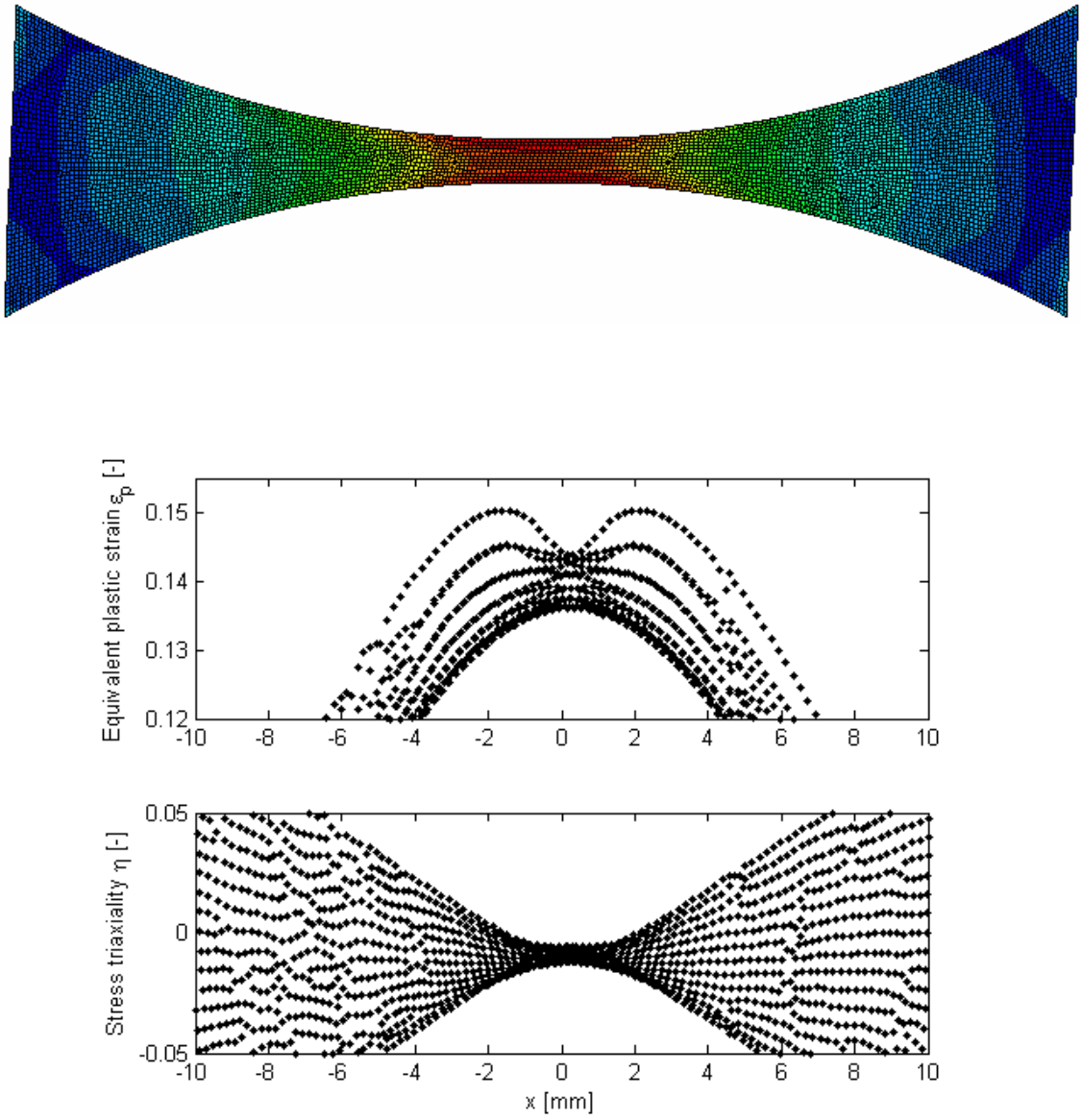

Figure 5-3: Equivalent plastic strain and stress triaxiality near the specimen center for $R_S = 50mm$.

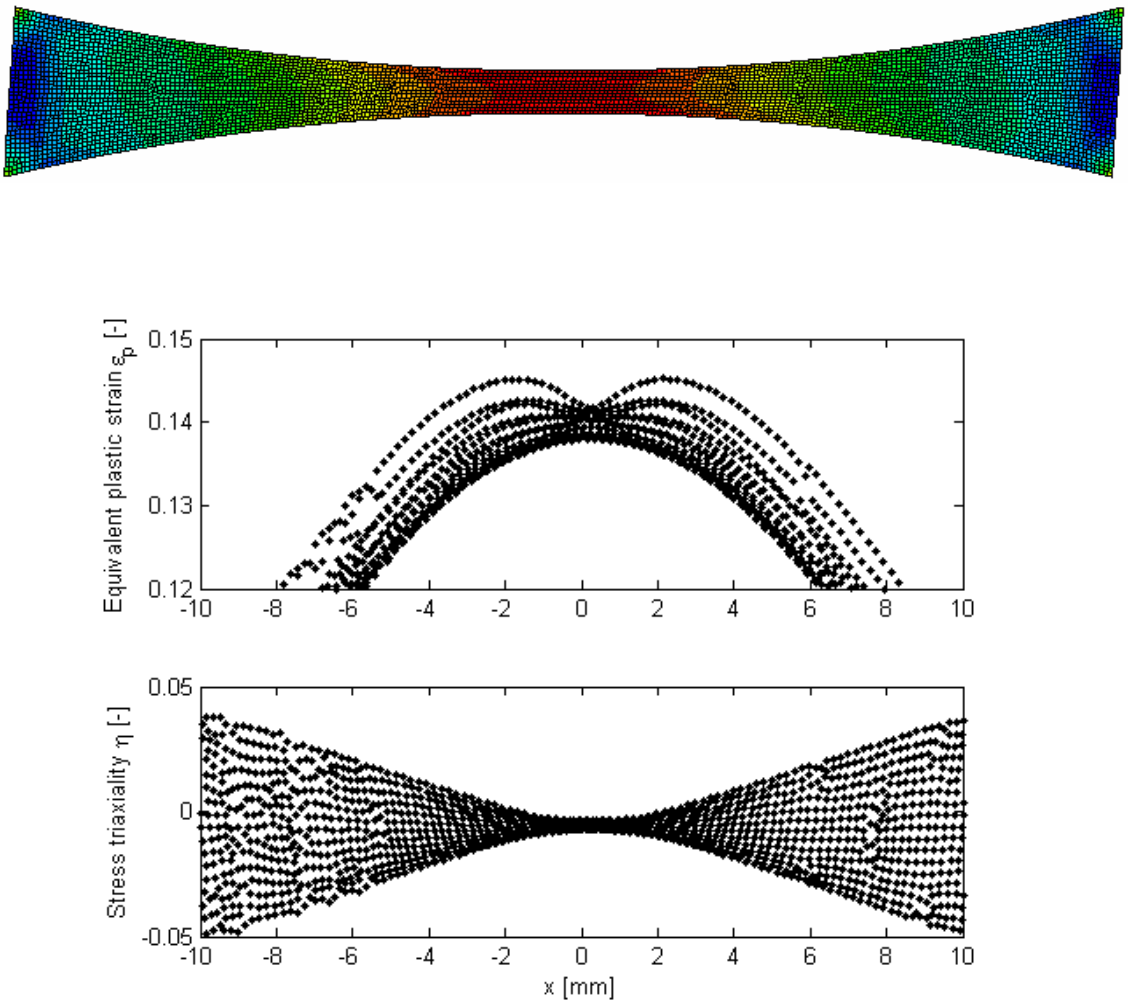

Figure 5-4: Equivalent plastic strain and stress triaxiality near the specimen center for $R_S = 100mm$.

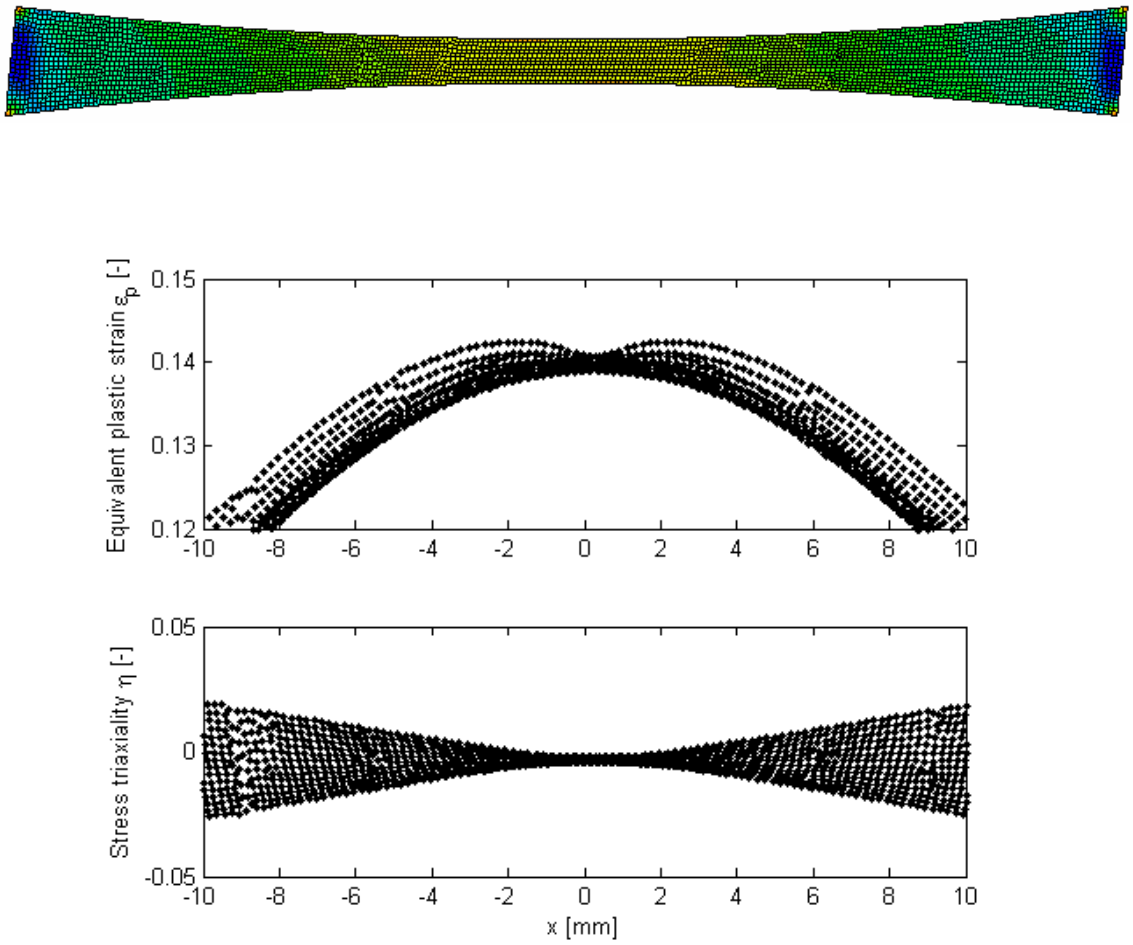

Figure 5-5: Equivalent plastic strain and stress triaxiality near the specimen center for $R_S = 200mm$.

corresponding equivalent plastic strain plots show more pronounced variations. For instance, for $R_S = 50mm$, the equivalent plastic strain varies from 0.135 to 0.15 within a central zone of $w_c = 2mm$. Note that the equivalent plastic strain reaches its maximum at the tangential point between the flat and curved boundary of the central gage section. The homogeneity of the strain distribution can be improved by increasing the shoulder radius (see Fig. 5-5). Since the small increase in the equivalent strain appears to be due to the change in curvature between the flat and round shoulder region, we considered a boundary of clothoidial shape where the curvature increases linearly with the distance from the specimen center. Figure 5-6 shows the smooth plastic strain profile which is obtained for the clothoidally shaped boundary with the shape parameter $\sqrt{RL} = 47mm$ (R is the radius of curvature and L is the length along the clothoidal boundary).

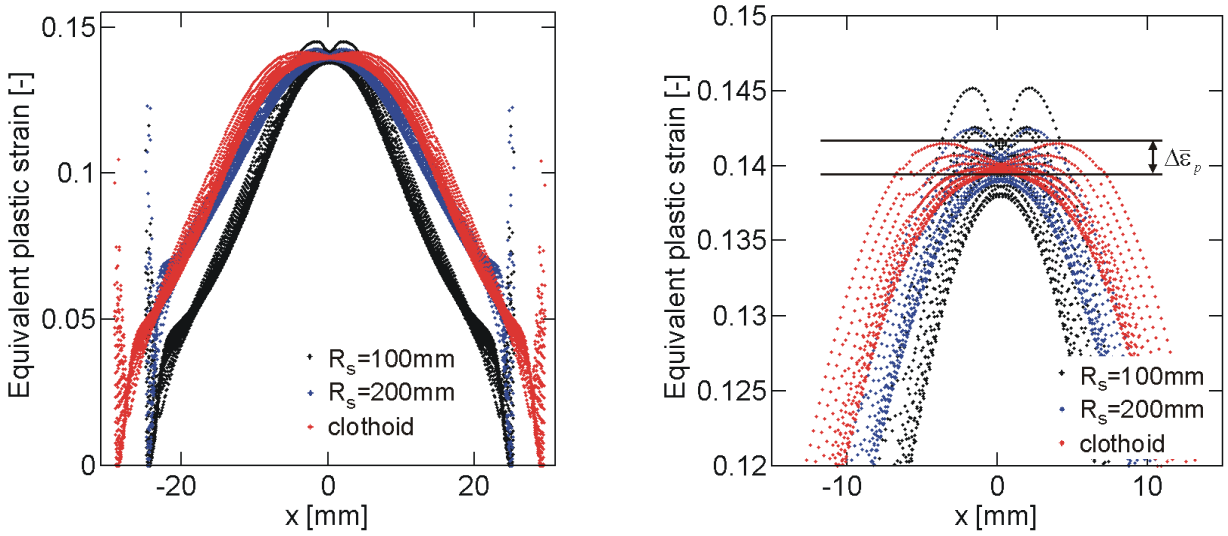

Figure 5-6: Influence of the shoulder curvature.

5.2.4 Effect of the lateral boundary curvature

The effect of the lateral boundary is investigated for the clothoidal shoulder geometry. The curvature of the lateral boundary is described by the radius R_l in Fig. 5-1. The same intersection points of the lateral boundaries with the specimen shoulders are chosen for all calculations while

the lateral boundary radius R_l is varied. Figure 5-7 depicts the variation of the equivalent plastic strain at that boundary along the vertical direction ($y = 0$ corresponds to the specimen center line) for macroscopic shear loading ($\beta = 0°$). The thick solid line shows the strain distribution for a straight boundary, i.e. $R_l = \infty$ (configuration "D"). The strain distribution is non-uniform and increases monotonically from 0.0 at the specimen center to values as high as 0.1 near the specimen shoulder. Increasing the lateral boundary radius decreases the strain near the specimen shoulder (Fig. 5-7). Observe from curves A, B and C that the location of maximum strain is no longer at the corner with the specimen shoulder. It appears that configuration B with a radius of $R_l = 10mm$ provides the lowest maximum value of the equivalent plastic strain along the lateral boundary. In Fig. 5-7, we also show the results for negative curvatures, i.e. configurations where the gage section features an outward notch as initially proposed by Mohr and Henn (2007). The simulation results clearly show that these configurations (E and F) lead to very high strain concentrations near the specimen shoulders and should thus be avoided.

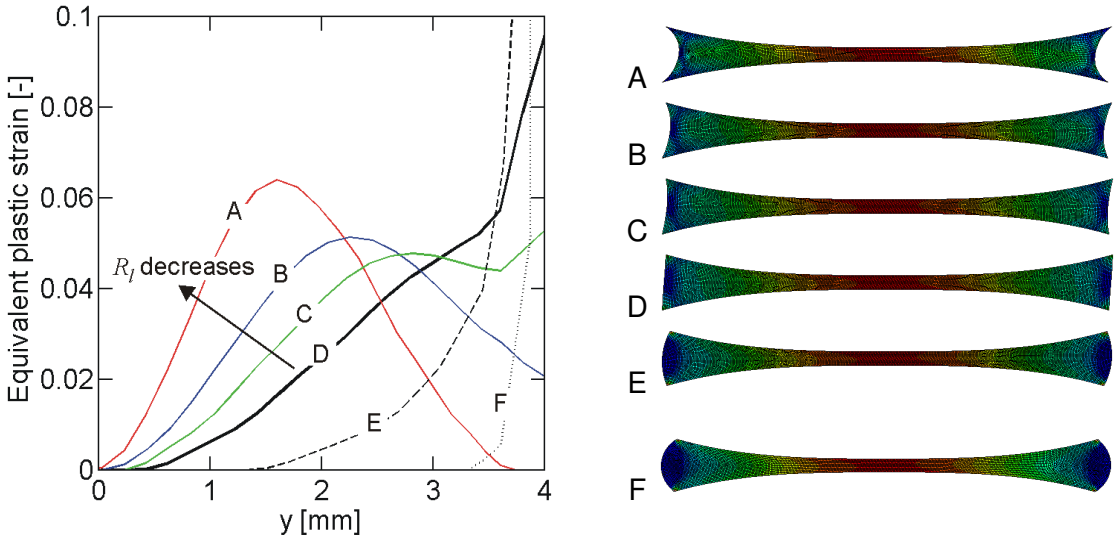

Figure 5-7: Variation of the lateral boundary curvature.

(A) $R_l = 5mm$; (B) $R_l = 10mm$; (C) $R_l = 20mm$; (D) $R_l = \infty$; (E) $R_l = -10mm$; (F) $R_l = -5mm$.

5.2.5 *Effect of the fillet radius*

A 3D solid element model is used to investigate the effect of the fillet radius between the specimen gage section and the specimen shoulders for macroscopic tensile loading ($\beta = 90°$). Figure 5-8 shows the distribution of the stress triaxiality and the equivalent plastic strain in the central vertical cross-section (corresponds to section A-A in Fig. 5-1). The simulation results for $R_f = 0.5mm$, $R_f = 1.0$ and $R_f = 2.0mm$ demonstrate that the equivalent plastic strain decreases faster from the gage section to the shoulder area for smaller fillet radii. On the other hand, small fillet radii induce a peak in stress triaxiality within the radius area. For instance, in the case of $R_f = 0.5mm$, the stress triaxiality increase from 0.58 within the gage section to about 0.8 in the radius region. However, the plot of the equivalent plastic strain versus stress triaxiality reveals that the corresponding plastic strains at high stress triaxialities are very small. Thus, it is concluded that the choice of the fillet radius has only a little effect on the experimental results and should be made based on manufacturing constraints.

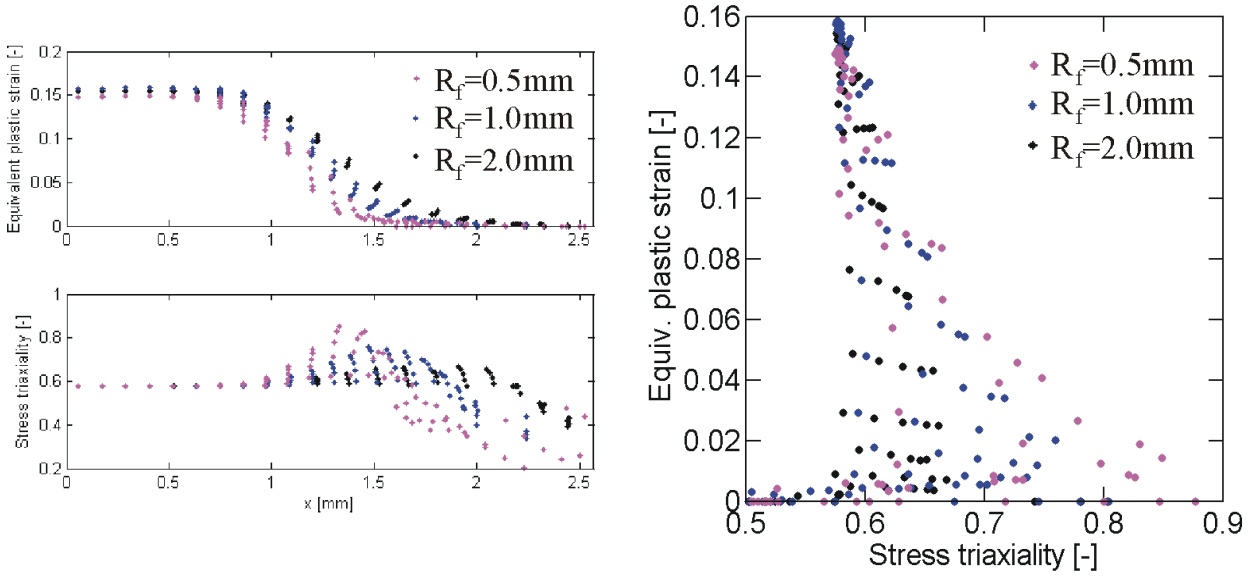

Figure 5-8: Influence of the fillet curvature on the stress triaxiality and equivalent plastic strain.

5.2.6 Final specimen geometry

The final specimen has the following dimensions: gage section thickness $t = 0.5mm$, minimum gage section height $h = 2mm$, maximum gage section height $H = 8mm$, gage section width $w = 57mm$, uniform gage section width $w_c = 0$, free distance between clamps $d = 12mm$, lateral boundary radius of $R_l = 10mm$ and fillet radius of $R_f = 2mm$. The shape of the clothoidal boundary (x_c, y_c) in the first quadrant is given by the dimensionless Fresnel integrals

$$x_c(L) = a \int_0^L \cos l^2 \, dl \tag{5.5}$$

$$y_c(L) = \frac{h}{2} + a \int_0^L \sin l^2 \, dl \tag{5.6}$$

with the curve coordinate L and the curvature parameter $a = 67mm$.

5.3 Hybrid experimental-numerical analysis procedure

Specimens of the final geometry are prepared and tested in a dual actuator system under various loading configurations. In this section, the underlying hybrid experimental-numerical analysis procedure is presented. The corresponding experimental results are discussed in Section 5.4.

5.3.1 Specimen preparation

The specimens are extracted from the 1.5mm thick sheet material by waterjet cutting. The thickness reduction of the gage section is then performed by CNC-machining. A first set of specimens is machined using a ball end mill of hemispherical shape; a second set is machined using a corner radius end mill. Unlike the ball end mills, the corner radius end mill featured a small flat area at the bottom of the end mill.

5.3.2 Dual actuator system

The tests are performed using a newly-developed dual actuator system (Mohr and Oswald, 2008). The custom-made dual actuator system applies tangential and normal loads to the boundaries of the butterfly specimen, which is clamped using high pressure grips. The horizontal actuator applies the tangential force to the lower specimen boundary. As shown in Fig 5-9, the lower specimen clamp is mounted onto a low friction sliding table. A load cell positioned between the horizontal actuator and the lower specimen clamp measures the tangential force. The normal force is applied through the vertical actuator in the upper cross-head. Two additional load cells have been integrated into the lower sliding table to measure the total vertical force. Combined tension-shear experiments are performed for biaxial loading angles β between $0°$ and $90°$. In all experiments, we observe a sudden drop in force level which is considered as the instant of the onset of fracture.

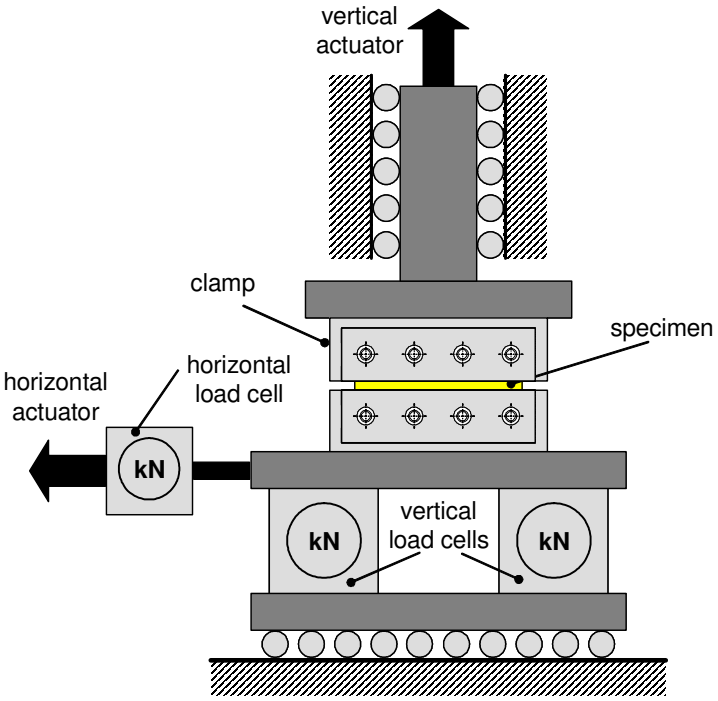

Figure 5-9: Schematic of the dual actuator system.

5.3.3 Optical strain and displacement measurements

During the tests, Digital Image Correlation is used to measure the surface displacement and strain fields. For that purpose two digital cameras (QImaging Retiga 1300i with 105mm Nikon Nikkor lenses) take about 500 pictures (resolution 1300x1030 pixels) of the speckle painted front and back surfaces of the specimen. The pictures of the front camera are used to determine the displacements of the specimen boundaries (translations and rotation). The front camera is positioned at a distance of 1.25m to take pictures of the entire specimen (square pixel edge length of 50μm). The photographs of the back face are used to perform accurate DIC measurements of the displacement field at the center of the specimen gage section. For that purpose, the second camera is positioned at a distance of 0.25m which reduces the square pixel edge length to 9μm. The average speckle size is about 70μm on both faces. The displacement field is calculated by DIC (VIC2D, Correlated Solutions) based on the assumption of a quadratic transformation of the 35x35 pixel neighborhood of each point of interest. The engineering axial and shear strains at the center of the specimen are computed from the relative horizontal and vertical displacements Δu and Δv of two points located at the center of the specimen

$$E_y = \frac{\Delta v}{\Delta y} \tag{5.7}$$

$$E_{xy} = \frac{\Delta u}{\Delta y} \tag{5.8}$$

Both points are located on the vertical axis of symmetry at an initial distance of $\Delta y = 20 pixels$ (180μm).

5.3.4 Finite Element model

Simulations of each experiment are carried out using the explicit version of the finite element analysis software Abaqus (2007). The material constitutive model is implemented in a user subroutine for an explicit time integration scheme (VUMAT for Abaqus/Explicit). Reduced integration 3D solid elements (types C3D6R and C3D8R from the Abaqus element library) are used to mesh the specimen. Exploiting the symmetry of the specimen geometry, only half of its

thickness is modeled. Note that the portion of the specimen shoulders between the clamps are not included in the mesh as DIC measurements have shown that the slip between the specimens and the high pressure clamp is negligibly small.

The translations and rotations of the straight boundary line between the clamps and the specimen shoulders are measured by DIC during each experiment. Subsequently, the measured translation and rotation histories are imposed on the boundaries of the computational model. Figure 5-10 shows the corresponding time histories for pure transverse loading ($\beta = 0°$). Due to the high rigidity of the testing machine, the rotations are very small. Assuming zero rotations in the FEA model does not change the predicted force-displacement curves, but it has a significant effect on the fracture strain: in case of shear loading ($\beta = 0°$), the fracture strain is about 5% higher when imposing both translations and rotations.

Double precision simulations are run up to the experimentally measured instant of the onset of fracture. The loading velocity has been artificially modified in order to complete the computational analysis after about 600,000 time increments. The specimen meshes are designed to reduce spatial discretization errors inherent to a finite element analysis (see Chapter 3): mesh size is chosen such that dividing all elements' dimensions by two does not change the fracture

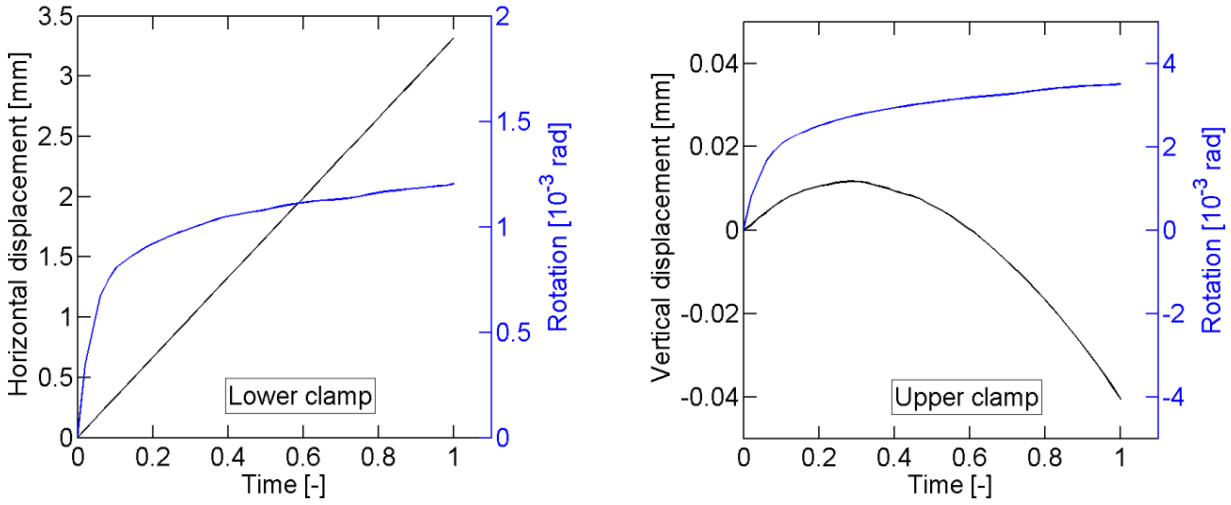

Figure 5-10: Boundary conditions during a pure transverse loading ($\beta = 0°$). Translation (black line) and rotation (blue line) of the lower clamp (a) and the upper clamp (b).

strain prediction by more than 0.5%. Because spatial discretization errors are mostly significant in regions where strain gradients are steep, different meshes are used for tension-dominated loadings ($\beta = 90°$ and $63°$) and for shear-dominated loadings ($\beta = 0°$ and $25°$). In tension-dominated experiments, strains localize through the thickness at the center of the gage section; consequently, the corresponding mesh features a dense mesh in the through-thickness direction. On the other hand, the meshes used to simulate shear-dominated experiments have only few elements through the thickness, while an increased mesh density along the width of the gage section is required. Both meshes are made of about 70,000 elements. Their main characteristics are summarized in Table 5-1. Note that both meshes are very fine, with elements dimensions close to the actual grain size of the TRIP steel.

Table 5-1: Characteristics of meshes used in Finite Element Simulations

Loading	Number of elements in the gage section			Size of the critical element [μm]		
	Height	Width	Thickness	Height	Width	Thickness
Shear-dominated	60	210	4	36	215	65
Tension-dominated	80	54	8	26	788	32

5.4 Results

5.4.1 Effect of the milling procedure

The sensitivity of the experimental results with respect to the machining process is investigated for pure shear loading experiments ($\beta = 0°$). Figure 5-11.a shows the measured force-displacement curves for specimens machined with ball and corner end mills, respectively. Observe that the horizontal displacement at which fracture occurs is about 55% lower for the specimen machined with ball end mills (red line in Fig. 5-11.a). The two specimens machined with corner radius end mills (black line in Fig. 5-11.a) feature almost the same fracture

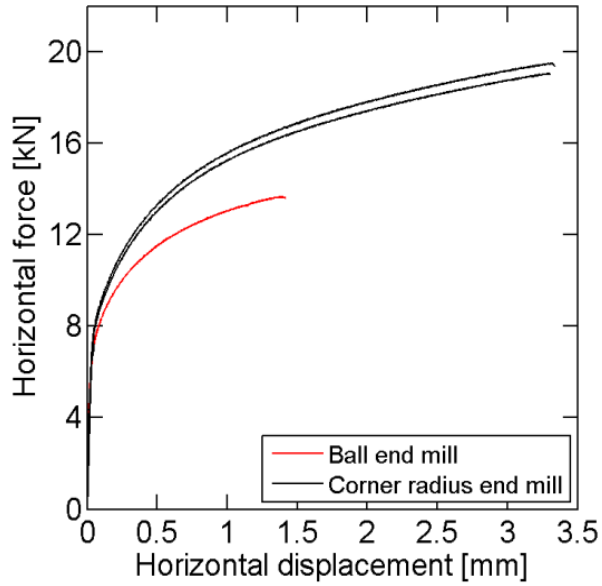

(a)

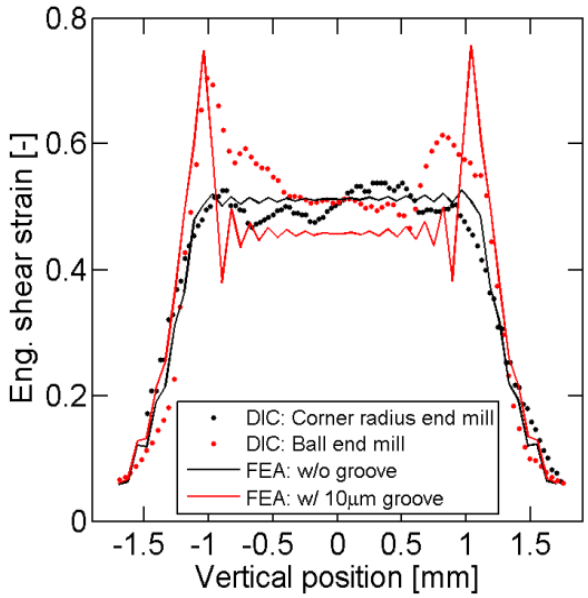

(b)

Figure 5-11: Influence of the specimen machining on a pure transverse loading experiment ($\beta = 0°$). (a) Force displacement curves for a specimen prepared with ball end mills (red line) and for two specimens prepared with corner radius end mills (black lines) submitted to a pure transverse loading: $\beta = 0°$. (b) Engineering shear strain along the vertical symmetry axis of the specimen as measured by DIC on the surface of the specimen prepared with ball end mills (red points) or prepared with corner radius end mills (black points), and as computed by FEA for a mesh with a flat gage section (black line) or with a 10µm groove along the fillets (red line). The position 0 corresponds to the horizontal axis of symmetry of the specimen.

displacement, highlighting a good repeatability of this test. Note that the difference in the force level is due to small variations of the average gage section thickness from one specimen to another.

Figure 5-11.b depicts the engineering shear strain evolution at the surface for each type of specimen; it is plotted along the vertical axis of symmetry for a horizontal displacement of 1.5mm. In the specimen machined with the ball end mill (red dotted line in Fig. 5-11.b), the strain is constant at the center of the gage section, but it exhibits an important peak near the boundary between the gage section and the specimen shoulder. The specimen machined with the corner radius end mill (black points in Fig. 5-11.b) shows a more or less constant strain throughout the entire gage section. Here, it is speculated that the use of a ball end mill has created a groove at the boundary of the clothoidally-shaped shoulder region. The effect of a possible groove can also be predicted by our finite element model. We introduced a $10\mu m$ deep groove into the finite element mesh and ran the simulation to the same horizontal displacement as in the experiment. The corresponding simulation results confirm the experimentally observed localization of shear deformation (red solid line in Fig. 5-11.b), while a uniform shear strain distribution is observed for a simulation without groove (black solid line in Fig. 5-11.b). Based on these observations, all subsequent experimental results are reported for specimens that have been machined using a corner radius end mill.

5.4.2 Experimental results

Force-controlled experiments are performed for four different loading conditions: $\beta = 0°, 25°, 63°$ and $90°$. During the experiments for $\beta = 63°$ and $90°$, the control mode is switched to displacement control before the onset of localized necking. From each experiment, we obtain tangential force versus horizontal displacement and axial force versus vertical displacement curves. In addition, the evolution of engineering shear and axial strains is recorded. The measured force-displacement curves are depicted with black points (blue points for strain evolution) in Fig. 5-12.b ($\beta = 0°$), Fig. 5-12.e-f ($\beta = 25°$), Fig. 5-12.c-d ($\beta = 63°$) and Fig. 5-12.a ($\beta = 90°$).

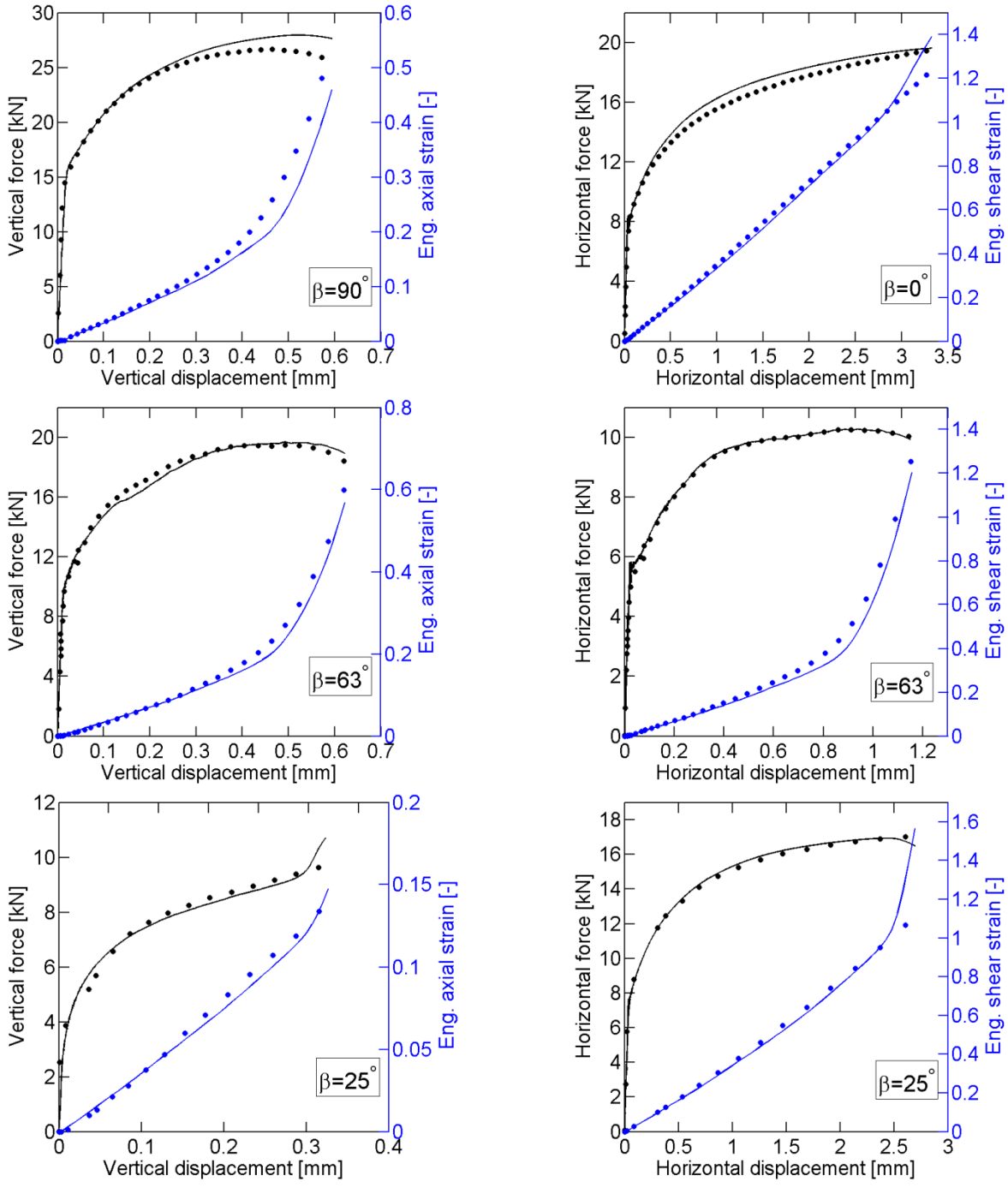

Figure 5-12: Experimental (dots) and simulation (lines) results.

(a): $\beta = 90°$. (b): $\beta = 0°$. (c) and (d): $\beta = 63°$. (e) and (f): $\beta = 25°$. The force displacement curves are depicted in black, while engineering surface strains are plotted in blue.

In experiments with tension dominated loading ($\beta = 63°$ and $\beta = 90°$), the force-displacement curves exhibit a force peak prior to fracture (black dots Fig. 5-12.a and 5-12.c). This maximum seems to coincide with the onset of localized necking. Note that this force peak is also associated with a noticeable surface strain rate increase at the center of the gage section (blue dots in Fig. 5-12.a and 5-12.c-d). The deformation localizes at the center of the specimen which leads to a pronounced thickness reduction in the form of a neck and subsequent onset of fracture. The measured force-displacement curves increase monotonically until fracture for the shear-dominated experiments ($\beta = 0°$ and $\beta = 25°$). At the same time, the engineering surface strains at the specimen center increase linearly with respect to the displacement (blue dots in Fig. 5-12.b and 5-12.e-f). However full field DIC shows that, for large deformations, the deformation localizes along the clothoidally shaped shoulder, away from the vertical axis of symmetry of the specimen. Figure 5-13.a shows a contour plot of the maximal principal surface strain as measured by DIC on the last picture before failure of a specimen submitted to a loading angle of $\beta = 25°$. For shear dominated loadings, fracture initiates along the fillet.

5.4.3 Comparison of simulations and experiments

Figure 5-12 shows the corresponding simulation results for all four loading conditions. The simulated force-displacement curves are depicted with black solid lines, while the evolution of engineering axial and shear strains are plotted with blue solid lines. In case of the pure tension loading ($\beta = 90°$, in Fig. 5-12.a), the correlation between simulation and experimental results is good for small displacements. However, the force level predicted by FEA is to too high for displacements larger than 0.3*mm*. At the onset of fracture, the vertical force prediction is higher than the experimental measurement by 9%. Note also that the characteristic force peak, which corresponds to the onset of through-the-thickness localization, occurs later in the simulation. As a result, the axial engineering surface strain at the onset of fracture is about 18% lower in the simulation than in the experiment. The numerical results for $\beta = 63°$ (Fig. 5-12.c-d) are in good agreement with experimental results. The simulation is able to predict accurately the vertical and horizontal forces histories, including the drop in force level prior to fracture. Shear and axial strains are also predicted with great accuracy. The relative difference between strains computed by FEA and those measured by DIC is less than 11%.

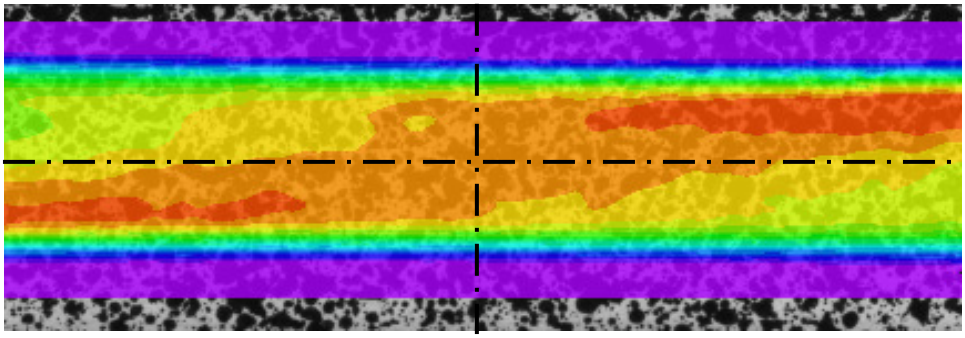

(a)

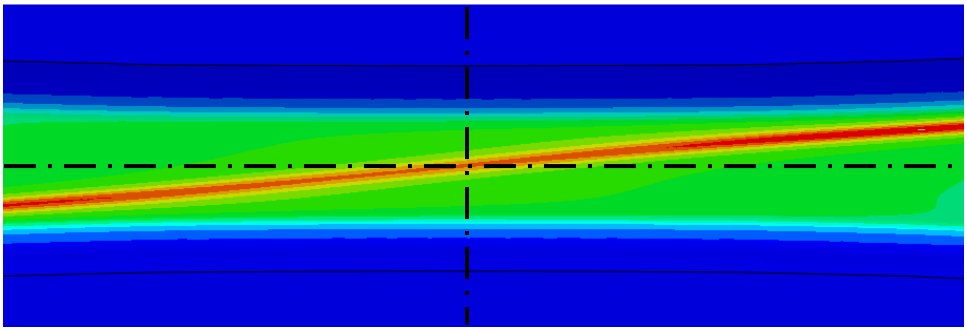

(b)

Figure 5-13: Principal strain at the surface of a specimen loaded with an angle $\beta = 25°$ at failure. (a) measured by DIC and (b) computed by FEA. Black dotted lines depict the axes of symmetry. Note that DIC measures Lagrangian strains while FEA computes logarithmic strains.

The simulation results for shear-dominated experiments ($\beta = 0°$ in Fig. 5-12.b and $\beta = 25°$ in Fig. 5-12.e-f) agree well with the experimental measurements up to about 85% of the fracture displacement. However, an important increase of strain rate can be observed on numerical results of both simulations prior to fracture, while experimental shear and axial strains increase linearly all the way to fracture in both cases. As a result, at the onset of fracture, surface strains predicted by FEA are much higher than experimental measurements at the center of the gage section. For the $\beta = 25°$ loading, the predicted engineering axial and shear strains at fracture are respectively 0.15 and 1.56, compared to 0.14 and 1.11 measured by DIC. It is also noticed that, for the

$\beta = 25°$ experiment, this increase of strain rate is correlated with a drop of the predicted horizontal force (black line in Fig. 5-12.f) and a large increase of the predicted vertical force (Fig. 5-12.e), both phenomena that are not observed experimentally. Those strain rates increases at the center of the gage section and force level variations can be explained in both simulations by the development of a narrow band (about 3 elements wide) where shear strains reach very high values (up to 1.6 in the simulation of the $\beta = 25°$ experiment). This "shear band" crosses the specimen gage section in diagonal, to join areas of maximal strains located on the upper and lower limits of the gage section, along the fillets. It is clearly visible in Figure 5-13.b, which depicts the contour plot of the maximal principal strain on the surface of a specimen submitted to a loading angle of $\beta = 25°$, as computed by FEA at the instant of fracture. However, this shear band does not appear on DIC measurements (Fig. 5-13.a).

5.4.4 Local stress and strain histories

Figure 5-14 shows the evolution of the equivalent plastic strain $\bar{\varepsilon}^p$ as a function of the stress triaxiality η (Fig 5-14.a) and the Lode angle $\bar{\theta}$ (Fig 5-14.b) at the location where fracture is assumed to initiate, for the four different loading conditions. The critical element where fracture initiates is considered to be the element where the equivalent plastic strain is the highest when the fracture displacement measured experimentally is reached. In tension-dominated experiments ($\beta = 90°$, in black in figure 5-14 and $\beta = 63°$, in red), stress triaxiality is first constant and then increases continuously beyond the onset of localize necking, to reach about 0.68 at the onset of fracture in both case. This increase is due to the development of a three-dimensional stress state inside the neck. The pure tension loading features a constant Lode angle of zero. In shear-dominated experiments, both stress triaxiality and Lode angle are approximately constant throughout loading. Note that the TRIP780 material exhibits a very large ductility, with fracture strains higher than 1.0 in both shear-dominated experiments, and 0.92 for the loading $\beta = 63°$.

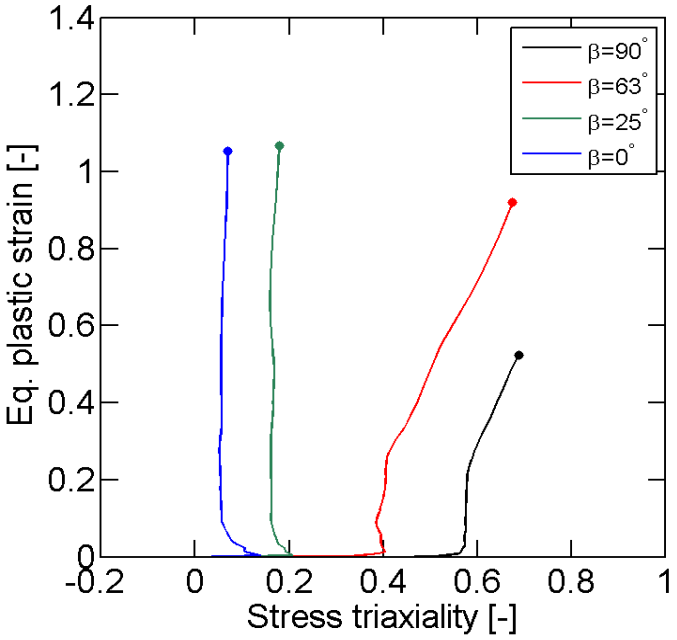

(a)

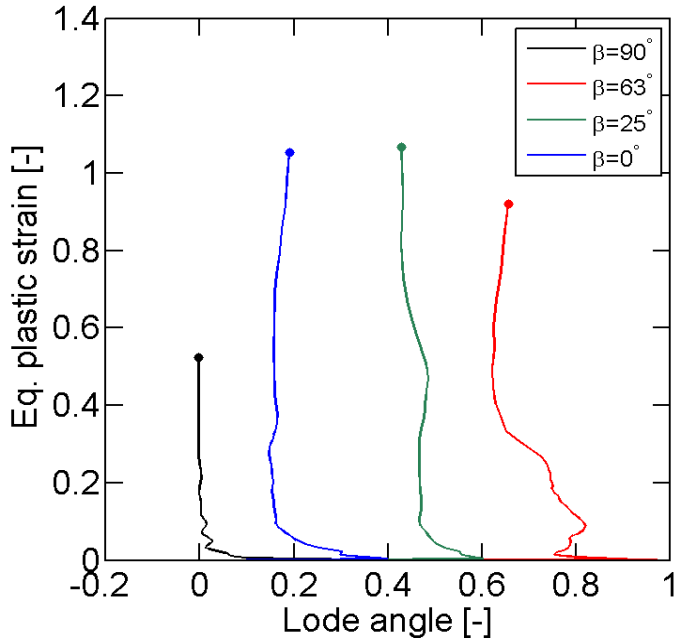

(b)

Figure 5-14: Loading paths for the 4 loading conditions at the critical element of the specimen. The critical element is the point of highest equivalent plastic strain at fracture displacement.
(a) Evolution of equivalent plastic strain with respect to stress triaxiality.
(b) Evolution of equivalent plastic strain with respect to Lode angle.

5.5 Discussion

5.5.1 Strain localization during loading

Experiments have shown that strain field localizes both in tension-dominated and shear-dominated experiments. Localization during tension-dominated loadings is due to necking and results in thickness reduction and development of three dimensional stress and strain states in the neck. This type of localization cannot be avoided in most fracture experiments based on tensile loading of flat specimens. To the best knowledge of the author, modified Nakazima experiments (Walters, 2009), or other experimental procedures based on membrane loading of sheet materials, are the only way to reduce or eliminate the effect of necking for stress states ranging from uniaxial to equibiaxial tension.

In shear-dominated experiments, strain localization appears for large displacement along the curved boundary line between the gage section and the specimen shoulder. It is worth noting that even for large deformations (engineering shear strains of 1 or more), the strain field is approximately homogeneous at the center of the gage section. This type of localization has not been observed on experiments using the present geometry of the butterfly specimen on a less ductile material (martensitic 22MnB5 boron steel), for which the horizontal displacement during a pure transverse loading experiment ($\beta = 0°$) did not exceed 1.3mm (Mohr & Ebnoether, 2009). Very fine mesh densities are required to accurately describe strain gradients due to localization, which significantly increases the computational cost of the hybrid experimental-numerical analysis needed to determine the loading path to fracture. It is emphasized that using coarser meshes would result in significant errors on numerical results and especially on the fracture strain.

The main issue with localization of stress and strain fields prior to fracture is that the validity of standard plasticity theory may break down due to the presence of presence of steep strain gradients and porosity (and/or microcracks). Strain gradient formulations of the constitutive modeling (e.g. Gurtin & Anand, 2005) or advanced porous plasticity models with microstructural evolution (Danas and Ponte Castaneda, 2009) may overcome these limitations at the expense of computational efficiency.

5.5.2 Accuracy of the hybrid experimental numerical analysis

The accuracy of the predicted loading path to fracture can be evaluated by comparing surface strains measured by DIC to strains computed by FEA (Dunand & Mohr, 2009). Such a comparison permits to expect a satisfactory accuracy for tension-dominated loadings. As far as shear-dominated loadings are concerned, the significant difference observed between measured and computed strains do not imply that the corresponding loading paths are inaccurate, because fracture does not occur where strains are measured (at the center of the gage section). In shear-dominated experiments, fracture initiates along the thickness reduction fillet. Because of the non-flat surface of the specimen, three dimensional Digital Image Correlation techniques are required to measure strains at this location. Those measures have not been performed during experiments, making an evaluation of the accuracy of loading paths depicted in Fig. 5-14 difficult.

5.5.3 Determination of the fracture locus

Loading histories have been plotted in Figure 5-14 with the assumption that fracture initiates where the accumulated plastic strain is the highest. However the present butterfly specimen generally features a highly inhomogeneous stress field. Figure 5-15 depicts the stress and strain states for the 4 different loadings at the instant of fracture in the $(\eta, \bar{\varepsilon}^p)$ space (Fig 5-15.a) and in the $(\bar{\theta}, \bar{\varepsilon}^p)$ space (Fig 5-15.b). In case of the loading $\beta = 25°$ (in green in Fig. 5-15), equivalent plastic strain shows almost no variations in the thickness direction, while stress triaxiality increases from 0.18 on surface to 0.37 at mid-thickness where plastic strain is maximal. Recall that in shear-dominated experiments highest plastic strains are reached along the fillet, where the stress state, being affected by the fillet geometry, is not uniform in the thickness direction.

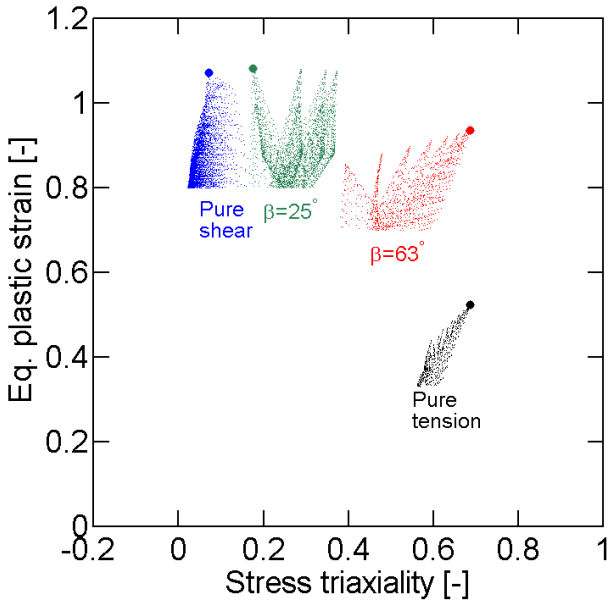

(a)

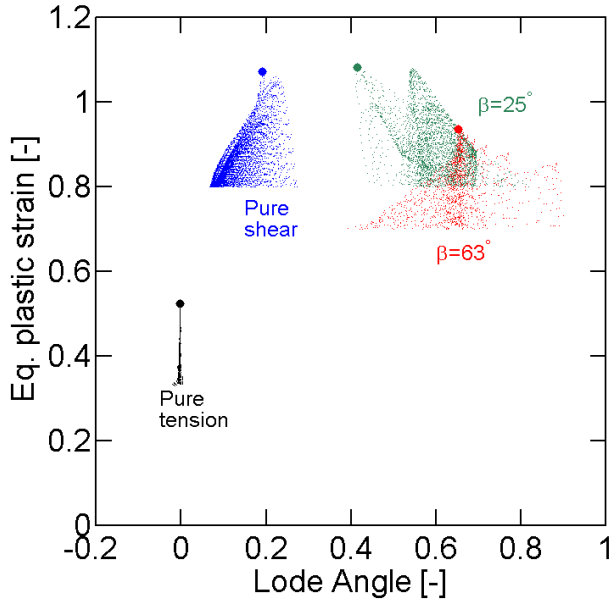

(b)

Figure 5-15: Stress and strain states at the onset of fracture for the 4 loading conditions.
(a) in the stress triaxiality – equivalent plastic strain space. (b) in the Lode angle – equivalent plastic strain space. Each dot stands for an integration point. Large dots represent the element with the highest equivalent plastic strain. Elements with low plastic strains are not included.

5.6 Conclusion

The experimental technique by Mohr and Henn (2007) has been revisited. The specimen design has been optimized to provide more homogeneous stress and strain fields in the area of fracture initiation. An hybrid experimental-numerical analysis of specimens submitted to four different loading conditions has permitted to characterize the loading path to fracture in the TRIP780 steel for loading states ranging from shear to transverse plane stress tension. Some remarks can be made based on this analysis:

(1) Test results, especially under transverse-dominated loading conditions, are very sensitive to machining imperfections. It is recommended to perform the thickness reduction of the gage section with a milling accuracy of at least $10\mu m$.

(2) The proposed geometry permits to get approximately constant stress and strain fields within the gage section for small deformations of the specimen. However, because of the important ductility of the TRIP material, specimens undergo large deformations before fracture. This leads to the development of stress and strain localizations in both transverse and tension dominated loading conditions. Analyses have shown that the numerical model used in this work is not able to predict with great accuracy the stress and strain states in the areas of localization.

Chapter 6.

Conclusion

This thesis is concerned with the accurate determination of the stress and strain histories in fracture experiments to provide an experimental data basis for the future development of ductile fracture models. The loading path to fracture in TRIP780 steel sheets has been identified for nine different multi-axial loadings, covering stress states from pure shear to equi-biaxial tension. The analysis of full thickness experiments has shown that the stress and strain histories prior to fracture can neither be estimated from the force history measurements using simple analytical formulas nor from optical surface measurements. In the present work, the loading histories have been characterized using a hybrid experimental-numerical approach.

An extensive experimental program has been carried out to investigate the inelastic behavior of the TRIP780 material under large deformations. Almost the same stress-strain curve has been determined from uniaxial tensile tests performed for seven different specimen orientations. However, the plastic flow (as characterized by Lankford's r-ratios) is direction dependent and its modeling requires the use of an anisotropic quadratic flow potential function. Here, a constitutive model with a planar isotropic quadratic yield function and a non-associated anisotropic flow rule is employed. Biaxial plasticity experiments have demonstrated that this constitutive model yields accurate predictions of the mechanical response under multi-axial loading.

Fracture experiments have been performed on three types of full thickness specimens, covering stress states from uniaxial to equi-biaxial tension. The errors affecting the determined loading histories have been quantified. In most experiments, through-the-thickness necking develops before fracture. An accurate description of the stress and strain fields within the neck region requires very fine solid element meshes and cannot be achieved using shell elements. To investigate the material fracture properties for stress triaxialities lower than 1/3, the experimental technique by Mohr and Henn (2007) has been used. Butterfly-shaped specimens have bee subject

to non-linear loading paths by applying combinations of normal and transverse forces at the specimen boundaries. A parametric study has been performed to choose a specimen geometry that guarantees the onset of fracture near the center of the specimen gage section. The proposed design is characterized by concave lateral edges and a flat gage section of reduced thickness delimited by two clothoidally-shaped shoulders. The hybrid experimental numerical determination of the loading path to fracture has been conducted for four different loading states, ranging from pure shear to transverse plane strain tension. The results show that the validity of the proposed hybrid experimental-numerical technique is very sensitive to machining imperfections. Furthermore, the computational model needs to be improved to provide accurate prediction of the local strain fields at very large strains.

References

Abaqus, Reference manuals v6.8, Abaqus Inc, 2008.

Angel T., Formation of martensite in austenitic stainless steels, Effect of deformation, temperature and composition, J Iron and Steel Institute 165, 1954

ASTM E8M-04, Standard Test Methods for Tension Testing of Metallic Materials, 2004.

Bai Y., Effect of Loading History on Necking and Fracture, PhD Thesis, MIT Department of Mechanical Engineering, 2008.

Bai Y, Wierzbicki T, A new model of metal plasticity and fracture with pressure and Lode dependence, Int. J. Plasticity 24, 1071-1096, 2008.

Bao Y, Prediction of Ductile Crack Formation in Uncracked Bodies, PhD Thesis, Ocean Engineering, Massachusetts Institute of Technology, 2003.

BaoY, Wierzbicki T, A comparative study on various ductile crack formation criteria, J. Engrg. Mater. Techn. 126, 314-324, 2004.

Banabic D, Bunge HJ, Pöhlandt K and Tekkaya A, Formability of Metallic Materials, Springer (Berlin), 2000.

Banu M, Takamura M, Hama T, Naidim O, Teodosiu C, Makinouchi A, Simulation of springback and wrinkling in stamping of a dual phase steel rail-shaped part, J. Mater. Processing Technology 173, 178-184, 2006

Barlat F, Brem JC, Yoon JW, Chung K, Dick RE, Choi SH, Pourboghrat F, Chu E, Lege DJ, Plane stress yield function for aluminum alloy sheets, Int. J. Plasticity 19, 1297, 2003a

Barlat F, Ferreira Duarte JM, Gracio JJ, Lopes AB, Rauch EF, Plastic flow for non-monotonic loading conditions of an aluminum alloy sheet sample, Int, J. Plastcity 19, 1215, 2003b.

Barranger Y, Doumalin P, Dupre JC, Germaneau A, Hedan S and Valle V, Evaluation of Three-Dimensional and Two-Dimensional Full Displacement Fields of a Single Edge Notch

Fracture Mechanics Specimen, in Light of Experimental Data using X-Ray Tomography, Engineering Fracture Mechanics 76, 2371-2383, 2009.

Bathe KJ, Finite Element Procedures, Upper Saddle River: Prentice-Hall Inc., pp 225-261, 1996.

Benzarga A, Besson J, Pineau A, Anisotropic Ductile Fracture Part II: Theory, Acta Materialia 52, 4639-4650, 2004.

Bishop JFW, Hill R, A theory of the plastic distortion of a polycrystalline aggregate under combined stresses, Phil. Mag. 42, 1951

Boehler JP, Demmerle S, Koss S, A new direct biaxial testing machine for anisotropic materials. Exp. Mech. 34, 1–9, 1994

Brozzo P, Deluca B, Rendina R, A New Method for the Prediction of Formability in Metal Sheets, Sheet Material Forming and Formability, in Proceedings of the 7th biennial Conference of the IDDRG, 1972.

Burford D, Narasimhan K, Wagoner R, A Theoretical Sensitivity Analysis for Full-Dome Formability Tests: Parameter Study for n, m, r and μ. Mettalurgical Trans. A 22A, 1775-1788, 1991.

Brünig M, Numerical simulation of the large elastic–plastic deformation behavior of hydrostatic stress-sensitive solids. Int. J. Plasticity 15, 1237–1264, 1999.

Brünig M, Obrecht H, Finite elastic–plastic deformation behaviour of crystalline solids based on a nonassociated macroscopic flow rule. Int. J. Plasticity 14, 1189–1208, 1998

Campana F, Cortese L, FEM evaluation of springback after sheet metal forming: application to high strength steels of a combined isotropic-kinematic hardening model, submitted for publications, 2008

Casey J, Sullivan TD, Pressure dependency, strength-differential effect, and plastic volume expansion in metals. Int. J. Plast. 1, 39–61, 1985

Chaboche JL, A review of some plasticity and viscoplasticity constitutive theories, Int. J. Plast. 24(10), 1642-1693, 2008

Chen P, Koc M, Simulation of springback variation in forming of advanced high strength steels, J. Mater. Processing Technology 190, 189-198, 2007

Clausing DP, Effect of Plastic Strain State on Ductility and Toughness, Int. J. Fracture Mech. 6, 71-85, 1970.

Clift SE, Hartley P, Sturgess CEN, Rowe GW, Fracture Prediction in Plastic Deformation Processes, Int. J. Mech. Sci. 32, 1-17, 1990.

Cockcroft MG, Latham DJ, Ductility and the Workability of Metals, J. Inst. Met. 96, 33-39, 1968.

Cvitanic V, Vlak F, Lozina Z, A finite element formulation based on non-associated plasticity for sheet metal forming, Int. J. Plast. 24, 646-687, 2008

Danas K, Ponte Castaneda P, A finite-strain model for anisotropic viscoplastic porous media: I-Theory, Eur. J. Mech. A/Solids 28, 402-416, 2009a.

Danas K, Ponte Castaneda P, A finite-strain model for anisotropic viscoplastic porous media: II-Applications, Eur. J. Mech. A/Solids 28, 402-416, 2009b.

Dunand M and Mohr D, Hybrid Experimental-numerical Analysis of Basic Ductile Fracture Experiments for Sheet Metals, Int. J. Solids Structures, 2009, doi: 10.1016/j.ijsolstr.2009.12.011

Durrenberger L, Molinari A, Rusinek A, Internal variable modeling of the high strain-rate behavior of metals with applications to multiphase steels, Mater. Science Engrg. A 478, 297-304, 2008

Embury J.D. and LeRoy G.H., Failure Maps applied to metal deformation processes. Proceedings of the ICF-4, vol.1, 15-42, 1977

Graf and Hosford, The Influence of strain-path changes on Forming Limit Diagram of AL6111 T4, Int. J. Mech. Science 36(10), 897-910, 1994

Green DE, Neale KW, MacEwen SR, Makinde A, Perrin R, Experimental investigation of the biaxial behaviour of an aluminum sheet, Int. J. Plasticity 20, 1677-1706, 2004

Gurson AL, Continuum Theory of Ductile Rupture by Void Nucleation and Growth: Part I Yield Criteria and Flow Rules for Porous Ductile Media, J. Eng. Mater. Technol. 99, 2-15, 1977.

Gurtin M and Anand L, A theory of strain-gradient plasticity for isotropic, plastically irrotational materials. Part 2: Finite Deformations, Int. J. Plast. 21 (12), 2297-2318, 2005

Hancock JW, Browm DK, On the Role of Strain and Stress State in Ductile Failure, J. Mech. Phys. Solids 31, 1-24, 1983

Hancock JW, Mackenzie AC, On the Mechanisms of Ductile Failure in High-Strength Steels Subjected to Multi-axial Stress States, J. Mech. Phys. Solids 24, 147-160, 1976.

Hasek V., Untersuchung und Theoretische Beschribung wichtiger Einflussgroessen auf das Grenzformaenderungsschaubild [Research and theoretical description concerning the influences on FLDs (In German)], Bleche Rohre Profile 25, 1978

Hershey AV, Plasticity of isotropic aggregate of anisotropic facecentered cubic crystals, J. Appl. Mech. 21, 241-249, 1954

Hill R, A theory of the yielding and plastic flow of anisotropic metals, Proc. Royal Soc. London A193, pp. 281-297, 1948.

Jacques P., Furnémont Q., Mertens A., Delannay F., On the source of work hardening in multiphase steels assisted by transformation-induced plasticity. Philosophical Magazine A81, 1789-1812, 2001

Jacques P., Furnémont Q., Lani F., Pardoen T., Delannay F., Multiscale Mechanics of TRIP-assisted multiphase Steels: I. Characterization and Mechanical Testing. Acta Materialia 55, 3681-3693, 2007

Johnson GR, Cook WH, Fracture Characteristics of three Metals Subjected to Various Strains, Strain Rate, Temperatures and Pressures, Eng. Fracture Mechanics 21, 31-48, 1985.

Keeler S.P. and Backhofen W.A., Plastic Instability and Fracture in Sheet Stretched over Rigid Punches, ASM Trans. Quart. 56, 25-48, 1964

Kuwabara T, Ikeda S, Kuroda T, Measurement and Analysis of differential work hardening in cold-rolled steel sheet under biaxial tension. J. Mater. Process. Technol. 80–81, 517–523, 1998

Kuwabara T, Advances in experiments on metal sheets and tubes in support of constitutive modeling and forming simulations, Int. J. Plast. 23(3), 385-419, 2007

Lademo OG, Hopperstad OS, Langseth M, An evaluation of yield criteria and flow rules for aluminium alloys. Int. J. Plasticity 15, 191–208, 1999

Lassance D, Fabrègue D, Delannay F, Pardoen T, Micromechanics of Room and High Temperature Fracture in 6xxx Al Alloys, Progress in Material Science 52 (1), 62-129, 2007.

Laukonis and Ghosh, Effects of Strain Path Changes on the Formability of Sheet Metals, Metall. Trans. A9A, 1859-1856, 1978

Leblond JB, Perrin G, Devaux J, An Improved Gurson-type Model for Hardenable Ductile Metals, Eur. J. Mech. A-Solids 14(2), 499-527, 1995.

Lecroisey F., Pineau A., Martensitic transformations induced by plastic deformation in the Fe-Ni-Cr-C system, Metallurgical Transactions 3, 387-396, 1972.

Lee KL, Whitehouse AF, Withers PJ and Daymond MR, Neutron Diffraction study of the Deformation Behavior of Deformation Processed Copper-Chromium Composites, Materials Science and Engineering A 348, 208-216, 2002.

Lee M-G, Kim D, Kim C, Wenner ML, Wagoner RH, Chung K, Spring-back evaluation of automotive sheets based on isotropic-kinematic hardening laws and non-quadratic anisotropic yield functions Part II: characterization of material properties, Int. J. Plasticity 21, 883-914, 2005.

Lee W, Chung K-H, Kim D, Kim C, Okamoto K, Wagoner RH, Chung K, Experimental and numerical study on formability of friction stir welded TWB sheets based on hemispherical dome stretch tests, Int. J. Plast., doi:10.1016/j.ijplas.2008.08.005, 2008

LeRoy G, Embury JD, Edward G, Ashby MF, A Model of Ductile Fracture Based on the Nucleation and Growth of Voids, Acta Metall. 29, 1509-1522, 1981.

Lin SB, Ding JL, Experimental study of the plastic yielding of rolled sheet metals with the cruciform plate specimen. Int. J. Plasticity 11 (5), 583–604, 1995

Llod and Sang, the influence of strain path on subsequent mechanical properties – orthogonal tensile paths, Metall. Trans. A10A, 1767-19772, 1979

Logan RW, Hosford WF, Upper bound anisotropic yield locus calculations assuming <111>-pencil glide, Int. J. Mech. Sci. 22, 419-430, 1980.

Makinde A, Thibodeau L, Neale KW, Development of an apparatus for biaxial testing using cruciform specimens. Exp. Mech. 32, 138–144, 1992

McClintock FA, A criterion of ductile fracture by growth of holes, J. Appl. Mech. 35, 363-371, 1968.

Mohr D, Dunand M, Kim KH, Evaluation of Associated and Non-associated Quadratic Plasticity Models For Advanced High Strength Steels Sheets under Multi-axial Loading, Submitted (Int. J. of Plasticity, December 2008).

Mohr D, Ebnoether F, Plasticity and Fracture of Martensitic Boron Steel under Plane Stress Conditions, Int. J. Solids and Structures 46 (20), 3535-3547, 2009.

Mohr D, Henn S, Calibration of Stress-triaxiality Dependent Crack Formation Criteria: A New Hybrid Experimental-Numerical Method, Experimental Mechanics 47, 805-820, 2007.

Mohr D, Jacquemin J, Large Deformation of Anisotropic Austenitic Stainless Steel Sheets at room Temperature: Multi-axial Experiments and Phenomenological Modeling, J. Mechanics and Physics Sol. 56(10), 2935-2956, 2008.

Mohr D, Oswald M, A New Experimental Technique for the Multi-axial Testing of Advanced High Strength Steels, Experimental Mechanics 48, 65-77, 2008.

Müller W, Pöhlandt KJ, New experiments for determining yield loci of sheet metal. Mater. Process. Technol. 60, 643–648, 1996

Nahshon K, Hutchinson J, Modification of the Gurson Model for Shear Failure, European J. Mechanics A-Solids 27, 1-17, 2008.

Nakazima K., Kikuma T. and Hasuka K., Study on the formability of steel sheets, Yawat Tech. Rep. 284, 1971

Oh S, Chen C, Kobayashi S, Ductile Failure in Axisymmetric Extrusion and Drawing, Part 2, Workability in Extrusion and Drawing, J. Eng. Ind. 101, 36-44, 1979.

Olson G.B. & Cohen M., Kinetics of Strain-Induced Martensitic Nucleation, Metallurgical Transactions 6A, 791-795, 1975

Padmanabhan R, Baptista AJ, Oliveira MC, Menezes LF, Effect of anisotropy on the deep-drawing of mild steel and dual-phase steel tailor-welded blanks, J. Mater. Processing Technology 184 (1-3):288-293, 2007

Pardoen T, Hutchinson JW, An Extended Model for Void Growth and Coalescence, J. Mech. Phys. Solids. 48, 2467-2512, 2000.

Rice JR, Tracey DM. On the ductile enlargement of voids in triaxial stress fields, J. Mech. Phys. Solids 17, 201-217, 1969.

Spitzig WA, Richmond O, The effect of pressure on the flow stress of metals. Acta Metall. 32, 457–463, 1984

Stoughton TB, A non-associated flow rule for sheet metal forming, Int. J. Plasticity 18, 687-714, 2002

Stoughton TB, Yoon JW, A pressure-sensitive yield criterion under a non-associated flow rule for sheet metal forming. Int. J. Plasticity 20, 705–731, 2004.

Stoughton TB, Yoon JW, On the existence of indeterminate solutions to the equations of motion under non-associated flow, Int. J. Plasticity 24, 583-613, 2008

Stringfellow R., Parks D., Olsen G., A Constitutive Model for Transformation Plasticity Accompanying Strain-induced Martensitic Transformations in Metastable Austenitic Steels, Acta Metall. Mater. 40 (7), 1703-1716, 1992

Sutton M, Orteu JJ, Schreier H, Image Correlation for Shape, Motion and Deformation Measurements. Basic Concepts, Theory and Applications. Springer, 2009.

Tarigopula V, Hopperstad OS, Langseth M, Clausen AH, Elastic-plastic behaviour of dual-phase, high-strength steel under strain-path changes, European J. Mech. A/Solids 27, 764-782, 2008

Tvergaard V, Needleman A, Analysis of the Cup-Cone Fracture in a Round Tensile Bar, Acta Metall 32, 157-169, 1984.

Walters CL, Effect of strain rate on fracture, PhD Thesis, MIT Department of Mechanical Engineering, 2009.

Wang J, Levkovitch V, Reusch F, Svendsen B,. Huetink J, van Riel M, On the modeling of hardening in metals during non-proportional loading, Int. J. Plast. 24, 1039-1070, 2008

Wierzbicki T, Xue L, On the Effect of the Third Invariant of the Stress Deviator on Ductile Fracture, Technical Report 136, Impact and Crashworthiness Laboratory, Massachusetts Institute of Technology, 2005.

Yoshida F, Uemori T, Fujiwara K, Elastic-plastic behavior of steel sheets under in-plane cyclic tension-compression at large strain, Int. J. Plasticity 18, 633-659, 2002.

Annex A

Biaxial plasticity tests: Experiment and simulation results

The following figures depict normal stress-strain curves (left column) and shear stress-strain curves (right column) for different specimen orientations and biaxial loading angles. The experimental results are shown by dashed curves while the solid lines depict the model predictions.

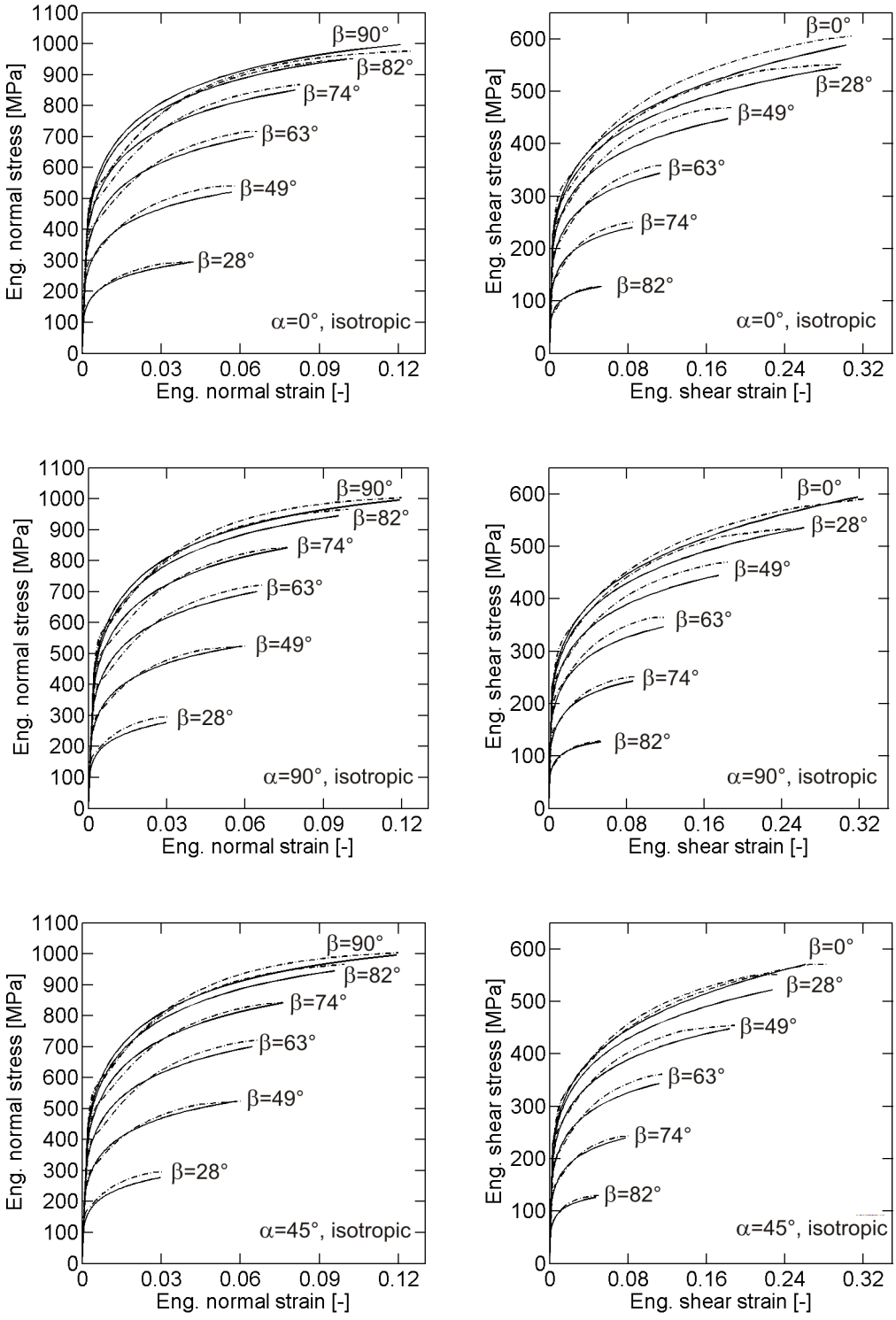

Figure A-1: Biaxial plasticity results – Model #1

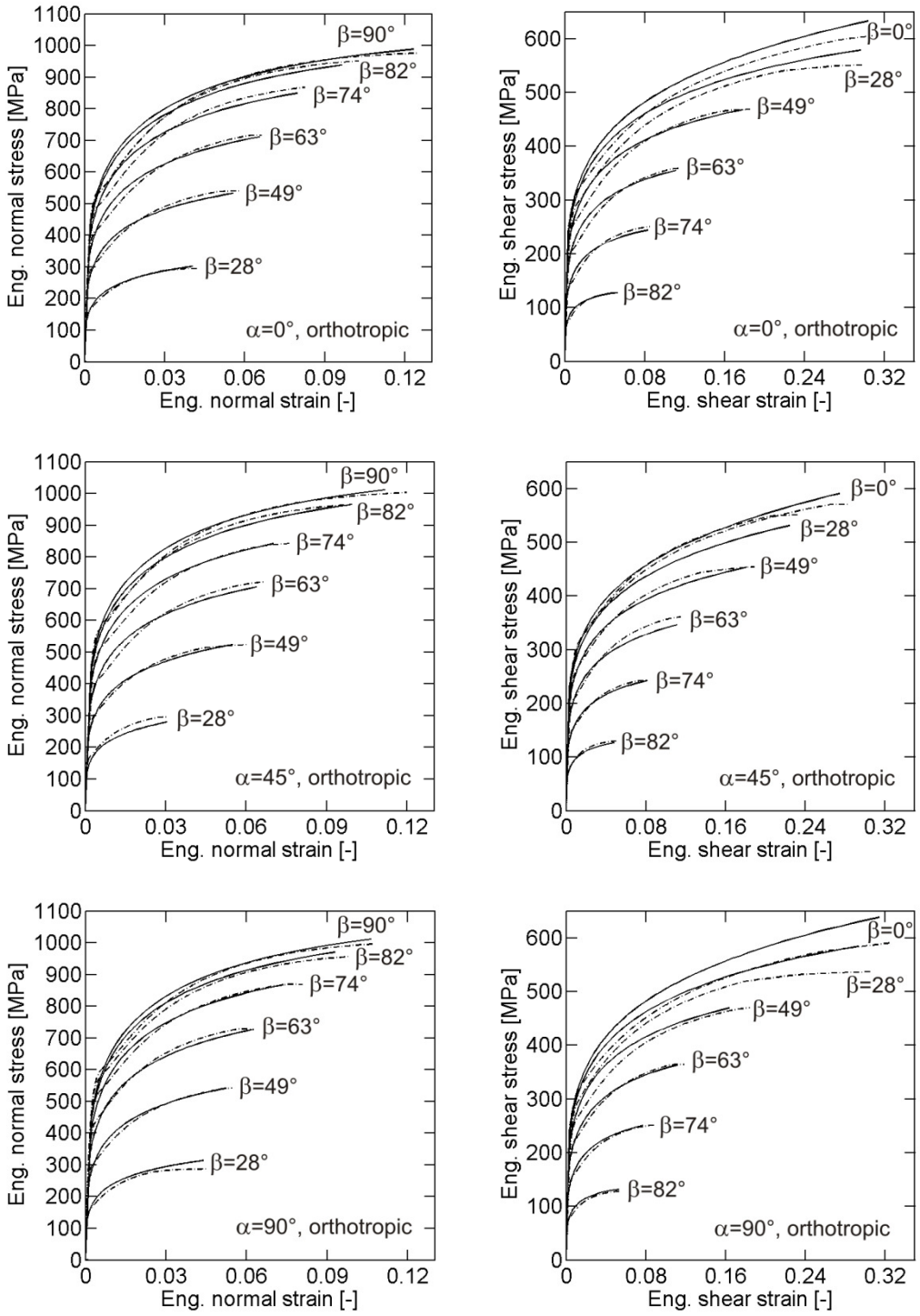

Figure A-2: Biaxial plasticity results – Model #2

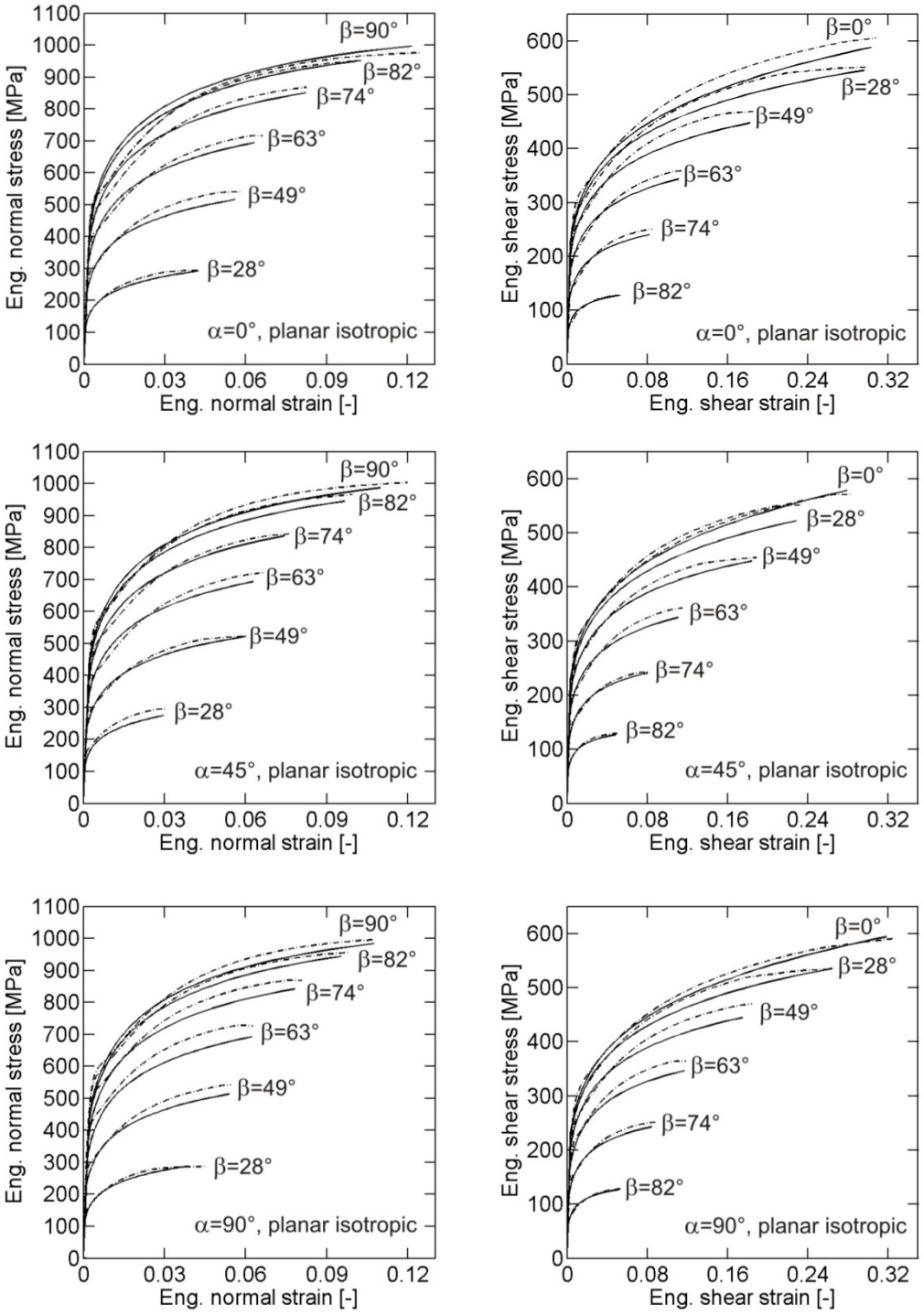

Figure A-3: Biaxial plasticity results – Model #3

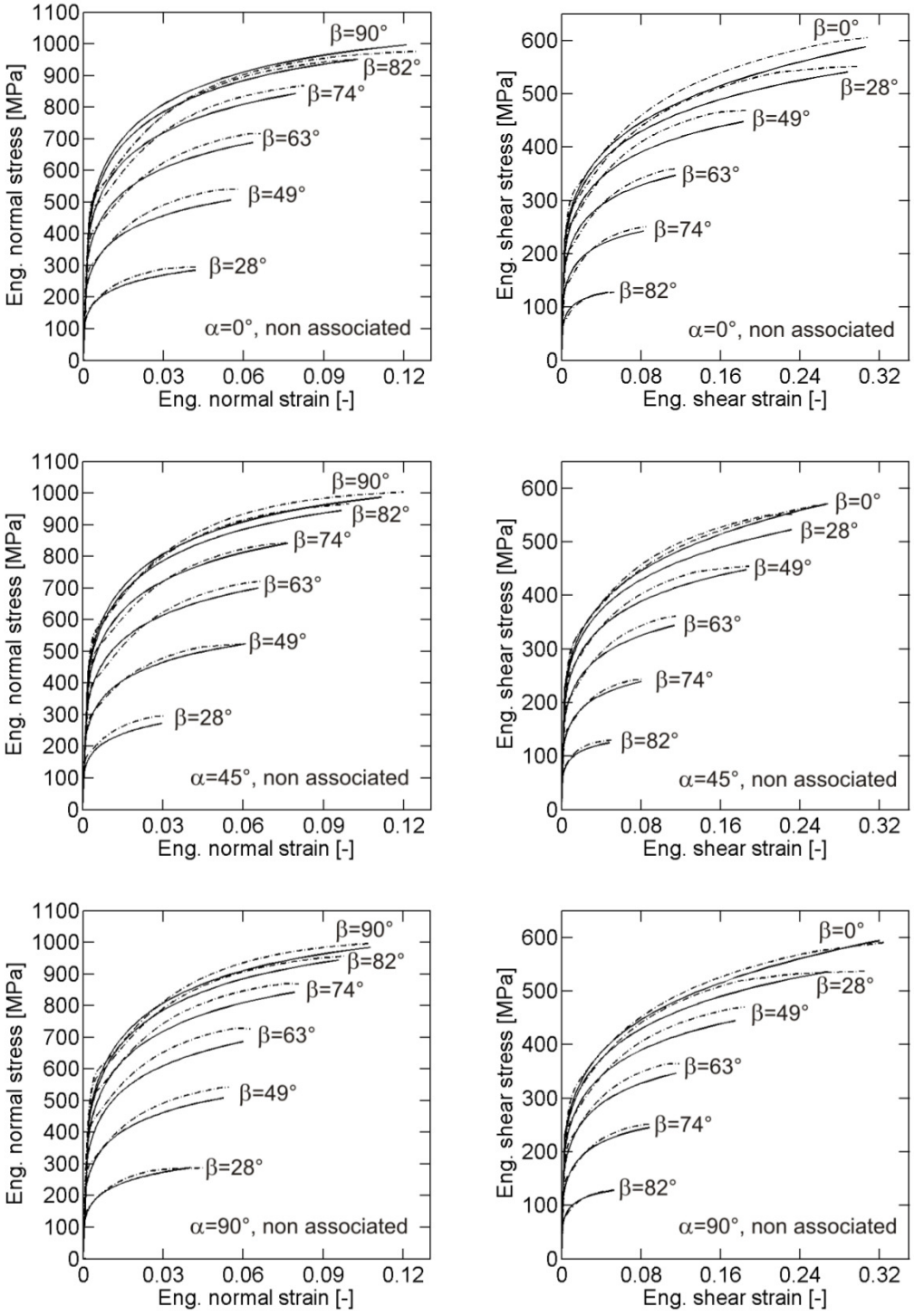

Figure A-4: Biaxial plasticity results – Model #4

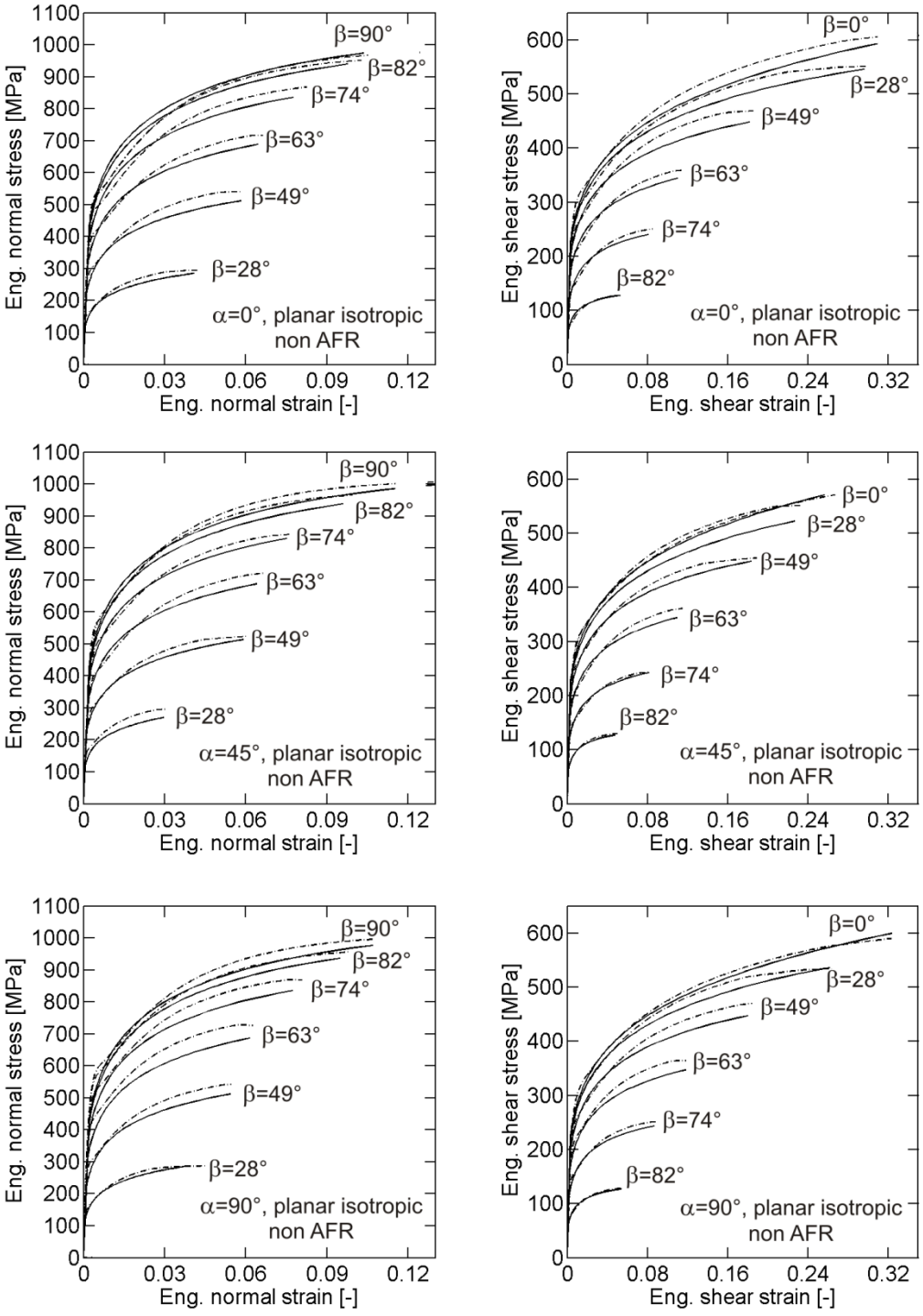

Figure A-5: Biaxial plasticity results – Model #5